MOLECULAR TAILORING AND ENGINEERING OF POLYMER-BASED MATERIALS FOR MARINE CORROSION AND METAL ION DETECTION APPLICATIONS

by

© Jinghan Feng

A Thesis submitted to theSchool of Graduate Studies

in partial fulfillment of the requirements for the degree of

Master of Engineering

Department of Engineering and Applied Science

Memorial University of Newfoundland

October 2014

St. John's, Newfoundland and Labrador, Canada

ABSTRACT

Corrosion is a long-lasting and challenging issue to modern industrial activities, especially to marine and offshore industries. In fact, the costs related to corrosion and corrosion prevention is a significant part of the gross national product in the world. Due to the increasing demand for marine transportation and oil and gas exploitation, solving the technological difficulties relevant to corrosion protection is absolutely essential. Epoxy resins have become one of the most widely used polymers in coating applications. However, common epoxy resins show undesirable water moisture affinity, which may lower their performance as anticorrosion coatings. Therefore, a series of polysiloxane derivatives have been synthesized and blended with epoxy resins as additives. The resulting material has been investigated by various chemical characterizations and numerical simulation of the cathodic protection system, called BEASY. As a result, various analyses confirmed that the performance of epoxy resin coatings in terms of corrosion protection was greatly enhanced.

ACKNOWLEDGEMENTS

First, I would like to express my sincere gratitude and deep appreciation to my supervisor, Dr. Wei Qiu, for his guidance throughout my M.Eng. studies, and assistance in the completion of this thesis.

Also, I would like to thank my co-supervisor, Dr. Yuming Zhao, for his generous help, constant encouragement, and tremendous guidance throughout my experimental part in the Chemistry Department.

I would like to thank Dr. Guang Chen, for his tremendous help, training, and suggestions during my study. I also would like to thank my dear groupmates, especially Dr. Shaoyu Ni and Ming Liu, in both Dr. Zhao's group and Dr. Qiu's group for their considerate assistance during my research work. I also would like to thank Prateek Dongare for his titration work in my side project.

I am grateful to the NSERC CREATE Training Program for Offshore Technology Research (OTR) and Memorial University of Newfoundland (MUN) for the financial support.

Last but not the least, I would like to express my profound appreciation to my parents and my beloved husband, Shuai Liang, for their encouragement, help and love.

Table of Contents

List of Tables

List of Figures

List of Schemes

List of Symbols, Nomenclature or Abbreviations

AFM	Atomic force microscopy
ATP	Aminopropyl-terminated polydimethylsiloxane
CP	Cathodic protection
CPE	Constant phase element
DGEBA	Diglycidyl Ether of Bisphenol A
EIS	Electrochemical impedance spectroscopy
EEC	Equivalent electric circuits
ER	Epoxy coating
EPON	Diglycidyl ether of bisphenol A
EPIKURE	Polyamide curing agent
ES	Eugenol-ethoxysilane-modified polysiloxane
EU	Eugenol-modified polysiloxane
FTIR	Fourier transform infrared spectroscopy
GPC	Gel permeation chromatography

HNMR	Proton nuclear magnetic resonance
ICCP	Impressed current cathodic protection
OCP	Open circuit potential
P1	Eugenol-modified polysiloxane
P2	Eugenol-ethoxylvinylsilane-modified polysiloxane
PAMS	Poly[(3-aminopropyl) methylsiloxane
PDI	Polydispersity index
PEG	Poly(ethylene glycol)
PMHS	Polymethylhydrosiloxane
SEM	Scanning electron microscopy
TBT	Toxic tributyltin
TGA	Thermogravimetric analysis
VOC	Volatile organic compounds
bf	Breakdown factor
c	transfer coefficient

E	Applied potential
E_{corr}	Corrosion potential
i_{corr}	Corrosion current
j	Current density
k	Conductivity
R_M	Metal corrosion rate
R_p	Polarization resistance
T_d	Decomposition temperatures
t_c	Coating life
t_t	Transition phase
u	potential
W	Integration domain
j_n	Current density component normal to the surface

Chapter 1 Introduction

1.1 Background of marine coating

The marine environment features very high corrosivity, as it generally contains three types of corrosive environments: marine atmosphere, splash zone, and seawater (ISO12944). The marine atmosphere is classified as C5-M in corrosivity categories, which is a very highly corrosive environment with a very heavy marine environmental impact (ISO9226). The corrosion level in the marine atmosphere is mainly determined by the time of wetness (TOW), air temperature, relative humidity, and the concentration of chlorides. TOW is the period of time when atmospheric conditions favors the formation of moisture on the metal surface, which is an important factor for the corrosion process. It is defined as the period of the time (hours per year) when temperature is higher than zero and the relative humidity is higher than 80% (ISO9223). However, in the presence of electrolyte, the moisture films may form even when the temperature is below zero and/or humidity is below 80%. As a result, a direct correlation between the defined TOW and the corrosion level can not always be successful determined, especially in the coastal regions with rich salt contents.(Mikhailov et al., 2008) Some mathematic models have been proposed to correlate the corrosion with salt concentration based on observed data. However, the models only work within the region where the data were obtained. Climate affects the corrosion level in marine atmosphere by altering the main factors mentioned above. In a cold marine atmosphere, the metal corrosion rate is relative slower as both

temperature and TOW are lower, but this is partially compromised by the fact that absorption of water vapor on metals reaches its maximum near the water phase transition temperature, in the region from – 5 ^{o}C to 5 ^{o}C.(Mikhailov et al., 2008) Gusty winds can accelerate the corrosion if they are from the ocean and bring high salt contents to the metals. Compared to the marine atmosphere, a splash zone represents a more severe corrosion environment. In addition to an oxygen-rich atmosphere and continuous splashing of electrolytes from the sea, the alternating wet and dry cycles greatly contribute to accelerating the corrosion. Such alternations cause not only mechanical stress within the metal, but also create concentration differences of both oxygen and electrolytes between different parts of the metal surface; especially, the ones below and above water levels. The concentration differences lead to potential differences that are crucial to the corrosion process. Seawater is another characteristic corrosive environment in marine environments. It provides ideal conditions for corrosion; that is, high humidity, high levels of oxygen, and high salt content. In addition, seawater contains rich biological species that play very important roles in the corrosion processes. Attachments of biospecies onto the metal surface modify the local environments of the attached sites through metabolic processes, resulting in different potential profiles in different parts of metal. Also, some bacteria, like sulfur reducing bacteria, are responsible for the acceleration of corrosion. The velocity of seawater flow has two extreme effects on to corrosion, either accelerating or retarding. The most common flow-influenced corrosions are erosion-corrosion and cavitation. (Shifler, 2005)

Despite the varying conditions in marine environments, general theories and mechanisms to account for corrosions usually hold true. Metal corrosion is mostly galvanic corrosion, an electrochemical reaction between two sites of metals. For galvanic corrosion to occur, some requirements must be fulfilled. First, the electrode potentials of both sites must be different. It is fulfilled when the two sites are from two different metals which show different electrode potentials in the galvanic series, or when two sites are from the same metal but with different electrochemical conditions, such as concentrations of electrolytes, oxygen, and pH.(Zhang, 1996) Second, both sites must be surrounded by an electrolyte solution. In marine environments, this requirement is readily available as seawater provides both moisture and electrolytes. Third, both sites must be electrically connected. It is simply done when two sites of metals are in direct contact or connected via a metallic bridge. When galvanic corrosion occurs, electrons flow from one electrode to another. In the meantime, electrochemical reactions occur at both electrodes, resulting in the anode being eroded. As an example, in the corrosion of steel, oxygen is reduced at the cathode mainly to hydroxyl ions, while iron at the anode is oxidized to ferrous ions which then undergo a series of electrochemical processes to form hydrated hematite, which is the so-called rust. (Sørensen et al., 2009)

The extent of galvanic corrosion is dictated by both thermodynamic and kinetic factors. From thermodynamic considerations, galvanic corrosion is a subsequence of electrode potential differences, which is based on the intrinsic properties of metals. Kinetically, many other factors contribute to the expression of galvanic corrosion,

including reactants, metallurgical factors, surface conditions, geometric factors, and electrolyte properties. (Zhang, 1996)

Pitting corrosion is a localized corrosion normally occurring on metals or alloys protected by a passive film. Ideally, oxide films formed over the metal surface provide good protection against further attack. However, oxide films are susceptible to aggressive electrolytes. Sulfide inclusions in steels (mainly MnS) create some small areas that become anodic, while other parts of the metals become cathodic. As corrosion commences, the electrochemical conditions within the cavities are modified. With decreasing pH in the cavities, the oxygen level decreases on the corroding surface. The initial micropitting, which is of the order of 100 μm to 200 μm in depth and diameter, grows into macropitting as the corrosion continues. It is believed that sulfate reducing bacteria (SRB) are responsible for the development of pitting by biological generation of hydrogen sulfide. The rate of pitting corrosion is closely related to the activity of SRB, which is influenced by the nutrient and oxygen levels, and temperatures. In polar seawaters, the pitting is greatly delayed compared to temperate seawaters.

Crevice corrosion is another type of localized corrosion occurring on different crevices, such as metal/metal crevices (*e.g.*, superimposed metallic parts, cracks), metal/nonmetal crevices (*e.g.*, plastic coating, nonmetallic inserts), and metal/macrofouling crevices (*e.g.*, under barnacles). In the crevice, local electrochemical conditions are different from the seawater due to the slow exchange between them. As a result, some parts within the crevice become anodic, while other

parts outside the crevice are cathodic. Similar to what happens in pitting corrosion, microorganisms are believed to be involved in and contribute to crevice corrosion.(Melchers and Jeffrey, 2008)

1.2 Methods for marine coating

1.2.1 Cathodic protection

Cathodic protection is mainly used in combating galvanic corrosion in harsh marine environments. The protection of metals is achieved by making metals cathodic in the galvanic corrosion with the help of sacrificial anodes (galvanic anodes) or impressed current. Sacrificial anodes, which must be electrically connected to the metals to be protected, are active metals in the galvanic series. The potential differences between sacrificial anodes and protected metals ensure protected metals are cathodic in the corrosion and thus remain inert as sacrificial anodes are corroded and consumed. Zinc is the most commonly used sacrificial anode material in marine environment, while aluminum and magnesium are also employed in some applications. As sacrificial anode, zinc can be directly coated on the surface of metals. For example, in zinc-coated steel, so-called galvanized steel, the zinc surface is oxidized into zinc oxide to form a barrier. Zinc corrodes 10 to 100 times slower than steel in most natural environments. With the zinc oxide barrier, both the zinc layer and the steel beneath are well protected from further corrosion.(Zhang, 1996) When some parts of the zinc oxide film are destroyed, the process of which can be accelerated by the high content of chlorides,(Yadav et al., 2004) the adjacent sites become active and act as anodes to

protect steel from corrosion. Besides direct coating, zinc can be mixed with a polymer in a powdery form to be coated on metal surfaces. The polymer coating provides a high electrical resistant barrier against aggressive species, while the zinc powder is responsible for the galvanic effect towards the cartion when the barrier is damaged. Such systems are effective and economical. Recently, conducting polymers have been used as additives to zinc-rich primes to enhance the anticorrosion performance and reduce the cost. For example, addition of polyanilineemeraldine salt(Emge and Bäuerle, 1999) in 0.3 wt% can reduce the loading of zinc pigment from 79 wt% to 60 wt% without a compromise of the anticorrosive performance(Armelin et al., 2007a)of the polymer coating. It was suggested that the reduction reaction of polyaniline from emeraldine to leucoemeraldines is accompanied by the oxidation of metals into cations. The metal cations form a second protective layer to aggressive ions in the metal-film surface with the dopant-anion in the polymer(Armelin et al., 2010; Torresi et al., 2005). Other conducting polymers, such as polythiophene, have also been found to bring enhanced anticorrosion performance to polymer coatings.(Armelin et al., 2007b)

Impressed current cathodic protection is anther important way of corrosion protection. It is done by applying a current into a metal cathode by an external source of dc power. Although featuring some advantages, the method is more demanding in terms of regular maintenance and monitoring and thus may be less cost effective than other anticorrosion protocols.(Sørensen et al., 2009)

1.2.2 Barrier Protection

Barrier protection offers an effective way of anticorrosion in marine environments. The barriers are created by passivation of a metal surface or providing external barriers such as organic coatings. Passivation of a metal can be done by oxidizing the metal surface into a layer of corresponding metal oxide. For example, in stainless steel, the chromium content is readily oxidized into chromium (III) oxide on the surface to form a film that prevents the approaching of aggressive species onto the metal surface. Although stainless steels are more resistant, they are still subjected to corrosion, notably pitting corrosion. Passivation of metal can also be done by generating a layer of insoluble deposition. For example, phosphates can be added to induce the formation of insoluble iron salts(Sørensen et al., 2009) on metal surfaces. Anodic films (metal oxide) are very adherent comparing to others, and in fact it naturally occurs on metal surface. However, the porous nature also means it has to be thick enough to provide a satisfied barrier effect and the increased thickness sadly makes it brittle. As to organic coatings, the adherence and brittleness can be tuned by changing the formulations.

Organic coating is another important way to protect metals from corrosion by the barrier effect. Typical organic coatings consist of pigments, binders, extenders, additives, and solvents. Pigments and binders constitute the major parts of organic coatings, which account for the main functions. Solvents are carefully chosen for better processability and film formation. Additives are used to fine-tune the coating properties,

solve technical problems, and occasionally enhance performance. Extenders are added to reduce cost.(Sørensen et al., 2009)

To create a barrier, two types of coatings are available. In the first type, inert pigments such as micaceous iron oxide, lamellar aluminum, or glass flakes are added as building blocks of barriers. Organic polymers are used as a matrix to bind the pigments and to provide adhesion to the metal surface. Within the coating, the flakes align parallel to the metal surface and overlap in a layer-by-layer fashion. The resulting barriers show low permeability for oxygen, water, chloride, and other aggressive species. The lower electrolyte concentration resulting from the ionic impermeability of the coating was believed to minimize the corrosion current.(Sørensen et al., 2009)

In the second type of coatings, organic polymer binders act as barriers. Ideal binders for such a purpose should possess strong adhesion to the metal surface and within the coating, a good barrier for aggressive species, and high mechanical strength.(Sørensen et al., 2009) Since the properties of coatings are closely related to the chemical structure of the binder, a better understanding of their structure-property relationships may be useful guidance to new designs in order to achieve better anticorrosive performance.

Epoxy resins (polyepoxide) are the most widely used polymer binders and are the most successful for applications in marine anticorrosion tasks. They are commonly prepared by reactions between biphenol A with epichlorohydrin followed by crosslinking with polyamines or polyamides. They show strong adhesion to metal

surfaces, which can be explained by the formation of hydrogen bonds between the hydroxyl groups of resins and the ferrous oxide layers on steel(Mikhailov et al., 2008; Nakazawa and Somorjai, 1995), or by interactions between hydroxyl oxygen and ferrous iron.(Mikhailov et al., 2008; Rouw, 1997)In addition, they have high chemical resistance, due to the stable carbon-carbon and ether bonds in the polymers. One drawback of epoxy resins lies in its oxidative degradation and discoloration under UV light. To overcome this problem and to maintain good corrosion protection, a UV resistant topcoat, such as polyurethane, is applied. Modified epoxy resins have been prepared to enhance UV resistance but at the cost of lowered corrosion resistance.(Shifler, 2005; Sørensen et al., 2009) Like many other polymers, adecrease in the permeability of epoxy resins with increased cross-linking results in improved barrier effects (Sangaj and Malshe, 2004; Zhang, 1996). However, a higher crosslinking decreases the fracture toughness of epoxy resins.(Levita et al., 1991; Sørensen et al., 2009) So a balance has to be made between corrosion resistance and mechanical strength. Other shortcomings of epoxy resins including the requirement of a good surface for casting, highly temperature-dependent curing, and limited overcoat-ability, should also be considered in their design. Many water-borne epoxy coatings are available but most of their performances are not comparable to the organic solvent-borne ones (formulations use any organic solvent instead of water). An exception is water-borne epoxy primes with zinc powders that show good corrosion protections.(Almeida et al., 2006; Zhang, 1996)

Acrylic polymers and copolymers are the second widely used polymer binders. They are commonly prepared by polymerization of acrylic acid or ester. Isocyanates or amino resins are used as crosslinking agents for curing. They show good adhesion and UV resistance, and are used as protective coatings. However, they alone do not provide corrosion resistance. Many modified acrylics have been prepared, such as epoxy-acid acrylics. These binders, while maintaining the merits of acrylics, show certain corrosion resistance, but normally not as good as epoxy resins alone.(Melchers and Jeffrey, 2008; Sørensen et al., 2009)

Polyurethanes are prepared by the reaction of isocyanates with compounds having active hydrogens. They show superior mechanical strength including high modulus and toughness. In addition, they show low loss of gloss and insignificant color change upon UV radiation. Also, they are scratch-resistant and suitable for the preparation of self-healing coating. The hydrogen bonds between the urethane linkages account for these properties. The drawback of polyurethane coatings are their poor resistant to mechanical strains; however, this can be improved by inducing crosslinking reactions in the coatings.(Sørensen et al., 2009; Zhang, 1996)

Polysiloxane is a type of polymer coating that shows good gloss and color retention. However, polysiloxane gives very poor mechanical properties. Because of its flexible polymer backbone, the glass transition temperature of polysiloxane is low. Therefore, it is often used as an adhesion promoter in coating formulations.(Sathyanarayana and Yaseen, 1995; Yadav et al., 2004) Epoxy modified

polysiloxane was reported to show anticorrosive behavior.(Ahmad et al., 2005; Emge and Bäuerle, 1999)

Other types of binders such as alkyd, chlorinated rubber, vinyl, and polyester have been used in organic coating. However, few of them have shown much success in providing good barrier effects in marine harsh environments.(Armelin et al., 2007a; Sørensen et al., 2009)

According to the types of solvents used, coatings can be divided into three categories, organic solvent-borne coatings, water-borne coatings, and solvent-free coatings (mostly powder coatings). Recent legislation has push the reductions of volatile organic compounds (VOC) and have spurred the development of new coatings with high solids content and low amounts of organic solvent. However, the performances of these new coatings are usually not as good as organic solvent-borne ones.(Armelin et al., 2010; Sørensen et al., 2009; Torresi et al., 2005)

1.2.3 Anti-biofouling coating

Biofoulings are greatly involved in corrosion in marine environments, and how to deal with such problems have received considerable attention. Marine biofouling can be defined as the undesirable accumulation of marine organisms on artificial surfaces immersed in seawater. It leads to many problems including acceleration of corrosion that leads to increased cost of operation and maintenance. Biofouling taking place on the hull of a ship can cause high frictional resistance, increased frequency of dry-

docking operations, deterioration of the coating, and introduction of invasive species.(Armelin et al., 2007b; Yebra et al., 2004)

Marine biofouling consists of 4 stages: (1) organic molecules like proteins accumulate on the surface to form a conditioning film; (2) bacteria and diatoms settle on the modified surface, and form a microbial biofilm with protozoa and rotifers, which provide other microorganisms with nutrients and protections; (3) more particles and organisms are trapped and the biofilm grows into a more complex community including multicellular primary producers, grazers and decomposers; (4) larger marine invertebrate and macroalgae settle down. (Sørensen et al., 2009; Yebra et al., 2004)

Two strategies are available for anti-biofouling protection: (1) prevention of the settle down or growth of microorganisms; for example, with the help of toxic pigments like biocides; (2) removal of settle-down organisms by self-releasing coatings.

For the first strategy, the most successful example is toxic tributyltin (TBT) based paints. They are based on acrylic polymers with TBT groups bonded through an ester linkage. After immersion, the soluble pigments in the paint dissolve and create pores. Water fills the pores and hydrolysis of the ester occurs releasing toxic TBT to inhibit the growth of microorganisms. In the meantime, part of the polymer after hydrolysis becomes hydrophilic and brittle due to an increased glass transition temperature. This part of the polymer is easily eroded by moving seawater, which reveals less reacted paint surface. The rate of hydrolysis can be tuned by controlled polymerization conditions to meet the different velocity of water. Although having

many merits, TBT based coatings are now banned due to environmental consideration.(Sørensen et al., 2009; Yebra et al., 2004)

Tin-free technology has been developed using a similar hydrolysis reaction or ion exchange to achieve the self-polishing effect and the toxic tin has been substituted with more environmentally friendly biocides. The most widely used biocides are copper-based reagents. For example, insoluble Cu acrylates has been designed, which release biocidal copper species in contact with seawater. The release of copper, in the meantime, makes the polymer more soluble, giving rise to the self-polishing effect. In these paints, Cu containing pigments, such as Cu_2O, are crucial for the anti-biofouling performance. In addition, booster biocides have been added to fight against some marine organisms that are mot susceptible to copper. These biocides include a variety of metallic-based and non-metallic compounds, synthetic and natural products.(Sørensen et al., 2009; Yebra et al., 2004) Another type of biocide commonly used is quarternary ammonium salts, which show biocidal activity through electrostatic and lipophilic interactions with the cell walls of microorganisms. (Banerjee et al., 2010; Sørensen et al., 2009)

Non-toxic technologies are also under development to prevent the settle down of microorganisms. One approach is the use of hydrophilic surfaces that resist the adhesion of fouling organisms; for example, immobilization of poly (ethylene glycol) (PEG) on the surface. The approach of proteins towards the substrate is disfavored by the repulsion caused by the compression of the PEG chains and the removal of water from hydrated polymers. However, PEG shows a tendency towards auto-oxidation,

which causes the loss of protein resistance. Development of new molecular systems other than PEG is thus warranted. To resist protein, the systems are expected to possess polar functional groups and hydrogen bond acceptors, but net charge or hydrogen bond donors should not be avoided.

Another approach to prevent the settle-down of microorganisms is to incorporate species that can damage organisms into the polymer coatings. For example, enzymes have been immobilized onto nanotubes for AF coating by degrading proteins. Nanotubes were selected as a support due to their large enzyme loading and high stability. Based on a similar concept, photo-activated self-cleaning films have been prepared. It was reported that high-energy species are produced upon UV-vis or NIR radiation by photoactive nanoparticles such as TiO_2. These high-energy species can degrade a variety of contaminants. For instance, transparent photoactive films based on carbon nanotubes with bovine serum albumin have been prepared.

The microtopography of the coating surface can also be manipulated for anti-biofoulings. It was reported that weak attachments occur if settling marine organisms are slightly larger than size of the topographical features. Because of the diversity of marine organism, it was reasoned that a coating with a hierarchically wrinkled surface topography having patterns of different length scales could be more effective in antifouling applications than coatings with a single topographical patterns. Field tests of coating designed based on this concept suggested a selective anti-biofouling effect(Banerjee et al., 2010; Sørensen et al., 2009). The anti-corrosive performance of some amphiphilic polymers developed recently were also ascribed to the topographical

effect caused by phase separations in addition to the electrostatic interactions.(Banerjee et al., 2010)

The second strategy used to remove settle-down organisms by self-releasing, coatings with a hydrophobic surface is commonly selected. For example, fluoropolymers give low surface energies and good non-stick characteristics, which can be used to prevent many organisms from interacting strongly with the surface. However, once some microorganisms are able to settle and accumulate, their removal them becomes difficult and requires a higher critical stress due to the high bulk modulus of the polymer. In contrast, polysiloxane elastomers show much better performance at removing accumulated marine organisms by seawater flow. Despite of this advantageous property, polysiloxane coatings still face significant problems as a result of their poor adhesion to the substrate, poor mechanical strength, and ease of damage. While the foul-releasing properties are moderate, the costs of polysiloxane elastomers are high.(Yebra et al., 2004) Recent research activities have been focused on the incorporation of biocides into elastomers so as to further reduce the settle down of the marine organisms(Majumdar et al., 2011). In another direction, superhydrophobic films based on silica nanoparticles, carbon nanotubes, and polymers have also been developed for fouling-releasing applications.(Banerjee et al., 2010)

Another type of self-cleaning film is based on stimuli-responsive materials, which show rapid and reversible changes with environmental conditions. Poly(*N*-isopropylacrylamide) is one example of thermo-responsive polymers. When temperature rises to lower than its lower critical solubility temperature, it changes from

a hydrophobic insoluble species to a hydrophilic soluble specie. The transformation leads to release of living cells attached to the polymer surface(Banerjee et al., 2010).

1.3 Theoretical model for marine coating

The development of a purely theoretical model to account for corrosion processes in the marine environment is extremely difficult due to the complexity of the problems.(Qin and Cui, 2003) Thus, most models are proposed based on past corrosion data, with or without some physical basis for the corrosion process involved.(Paik et al., 2004) The conventional models for corrosion assume the rate of corrosion is constant, thus weight loss of materials, which appear as depth of corrosion (d), increases as a linear function of time (t). However, more appropriate results can be achieved with nonlinear models using power expressions.

Southwell has observed that the development of corrosion depth increases non-linearly at an initial phase, but becomes relatively constant afterwards. The explanation for the two phases of corrosion is that initial nonlinear corrosion leads to the formation of oxidized products that cover the surface and subsequently change the mechanism of further corrosion. They proposed a linear equation(1) and a bilinear equation(2) model; however, both of them overestimated the corrosion depth at the initial corrosion phase. Melchers proposed an alternative nonlinear model equation(3) by interpreting their original models parameters.

Southwell linear model:

$$d = 0.076 + 0.038t, \quad (1)$$

Southwell bilinear model:

$$d = 0.09t, \ 0 < t < 1.46,$$

$$0.076 + 0.038t, \ 1.46 < t < 16, \quad (2)$$

Melchers-Southwell nonlinear model:

$$d = 0.084t^{0.823}, \quad (3)$$

Melchers also suggested a triliners model and a power approximation for corrosion depth.

Melchers trilinear model:

$$d = 0.170t, \ 0 \leq t < 1.46,$$

$$0.152 + 0.0186t, \ 0 \leq t < 1.46,$$

$$0.076 + 0.038t, \ 8 \leq t \leq 16, \quad (4)$$

Melchers power model:

$$d = 0.1207t^{0.6257}, \quad (5)$$

The above models recognize the non-linear time dependence of the corrosion rate on unprotected materials. For protected materials, new models have been

developed. GuedesSoares and Garbatov proposed a three-phase nonlinear model equation (6) for maintained corrosion protected plates.(Soares and Garbatov, 1999) In the first phase, corrosion is absent due to the existence of corrosion protection such as coatings. In the second phase, corrosion starts when the corrosion protection is damaged after coating life (t_c), and starts to level off after a certain time (t_t, which can be calculated from the data plot). In the third phase, corrosion progresses slowly and approaches a certain value (d_∞) due to the shielding effect arising from corrosion products accumulated on the surface.

$$d = 0,\ 0 < t \le t_c,$$

$$d_\infty \{1 - \exp[-(t - t_c)/ t_t]\},\ t > t_c, \tag{6}$$

Paik proposed a more general model equation (7) for seawater ballast tank structure of ships.(Paik et al., 2004) The model involved a transition phase (t_t) between the damage of coating at the coating life (t_c) and the start of corrosion, which is assumed to be zero. The value of m dictates the pattern of corrosion. With m less than 1.0 but larger than 0, the corrosion rate decreases overtime; with m larger than 1.0, the corrosion rate increases overtime, which is the case when corrosion products are continually removed from the surface. The value of m, as well as the value of c, can be determined in principle based on statistical corrosion data obtained from existing ship structures.

$$d = c(t - t_c - t_t)^m, \tag{7}$$

A more general model equation (8) was proposed by Cui for steel plated element, which is capable of including most existing corrosion models as its specific cases (Qin and Cui, 2003), The model includes a transition phase, which starts at time t_s. When corrosion starts, the coating deteriorates gradually and ends at time t_c when the coating has lost its protecting completely. In this phase, pitting corrosion takes place and the corrosion appears to accelerate. After that, corrosion decreases until time t_l when the structure is repaired or under maintenance or dead. The whole model contains four parameters d_∞, t_s, η and β.

$$d = 0,\ 0 \le t \le t_s,$$

$$d_\infty \{1 - \exp\{-[(t - t_s)/\eta]^\beta\}\},\ \ t_s \le t \le t_l, \tag{8}$$

All the above models rely on the extraction of parameters from the existing corrosion data. They may work well within environments with similar conditions to where the corrosion data are derived. But for the environments with major differences, calibrations must be conducted to ensure successful application of the model used. Guedes Sores has demonstrated the calibration of corrosion of ship structures in the marine atmosphere over the influences of relative humidity, chlorides, and temperatures. The results suggest that the corrosion rate (d^0, mg/m^2/day) increases with moisture ([Rh]), chloride contents ([Cl], mg/m^2/day) and temperatures ([T], °C), while the interactions between the three parameters are considered to be small.

$$d^0 = 0.3765[Rh] - 21.943,\ (60\% \le Rh \le 100\%),$$

$$= 0.0, (Rh < 60\%) \quad (9)$$

$$d^0 = 0.4184[Cl] + 69.062, \quad (10)$$

$$d^0 = 3.7493[T] + 85.689 \quad (11)$$

Melchers has applied a non-linear phenomenological model for marine immersion corrosion to copper-bearing steels and calibrated the corrosion rates over the seawater temperature.(Melchers, 2003) The model includes four phases that ought to be involved in marine immersion corrosion. Phase I is the kinetic phase that describes the initial corrosion under activation control and the following corrosion under oxygen concentration control. This phase can be modeled as a linear function of corrosion rate (r_0). Phase II is controlled by the oxygen diffusion to the corroding surface. A nonlinear function is adopted to estimate the approach of corrosion to anaerobic conditions through the theoretical time t_a. The total corrosion at that time is denoted as c_a. Phase III is controlled by sulphate reducing bacteria under anaerobic conditions. An expression of the corrosion curve in phase III is not available due to the currently insufficient understanding of this process. Phase IV is approximated to be a linear time-dependent corrosion process with a slope of r_s and corrosion axis intercept c_s, that corresponds to long-term anaerobic corrosion.

1.4 Motivation of this work

Organic coatings are highly important for the protection of steel structures against corrosive environments. The lifetime of these organic coatings usually depends

on the ability to protect the surface of the film to stop or retard the transport of corrosive species through it. In general, if the protective coating has a short lifetime and once it becomes permeable to water, some ionsand get into the metal/coatings interface, and trigger the corrosion process of the metallic substrate. This can lead to delamination between the coating and the protected metal and to the degradation of the organic coating and of the substrate. So protection performance of coatings generally depends on the barrier performance against water, oxygen and corrosive ions; in other words, reducing the water absorption can to a great extent improve the performance of coatings(Ji et al., 2006). Organic coatings that have a good lifetime are able to protect steel structures against corrosive environments due to less interaction with water and ions. Th eability of organic coating to protect the substrate from the environment is a sophisticated process, the mechanism has not been well understood and can be attributed to one of the following situations: (i) making anodic or cathodic areas less reactive, (ii) increasing electrical resistance in the circuit of the corrosion cell, and (iii) introduction of a barrier between substrate and aggressive species like oxygen, moisture and electrolytes. (Selvaraj et al., 2006; Suay et al., 2003)

Epoxy resins have been widely applied as protective coatings and adhesives due to their strong adhesion, high chemical resistance and good processing characteristics. However, due to the presence of hydrophilic hydroxyl groups in the polymer network, these epoxy resins can absorb water and lose adhesion and that leads to corrosion reaction on metallic substrates. The saturated water content in epoxy coatings has been reported as high as 10% (volume fraction). (Zhang et al., 2004) more receatly, epoxy

polyamide based coatings have been used to protect various steel structures, due to their better barrier protection and adhesion to surfaces. However, due to the presence of aromatic functionality, this polymer tends to degrade in UV light and also under high humidity. On the other hand, addition of chemical additives to epoxy coatings addresses the problem of brittleness and hydrophobicity. Modified polysiloxanes have been reported in the literature as additives for organic coatings, resulting in impressive performance for anticorrosion because of their low glass transition temperature, good thermal oxidative stability, low surface tension and high flexibility. Also, blending with polysiloxanes can attenuate the hydrophilic property of epoxy coatings. However, due to the poor miscibility and difficult in blending of polysiloxane systems with epoxy resins, functionalized polysiloxanes with reactive endgroups such as OH, NH_2 are highly required. (Rey et al., 1999)

It was reported that Cabanelas*et al*.(Cabanelas et al., 2001)investigated an epoxy–poly(organosiloxane) material prepared from diglycidyl ether of bisphenol A (DGEBA) and poly[(3-aminopropyl) methylsiloxane (PAMS), which is a polysiloxane functionalized with reactive branched amino groups, The DGEBA-PAMS was not miscible at room temperature; however, because of grafting of DGEBA to the polysiloxane chain by the epoxy-amine reaction, the blend became partially crosslinked. They made an epoxy system by adding PAMS as a curing agent rather than as a modifier (Cabanelas, 2003), and confirmed that the water absorption of the epoxy coating was considerably reduced due to changing the properties of epoxy coating from hydrophilic to hydrophobic. Kasemura*et al*.(Kasemura et al., 1993) studied the surface

modification of epoxy coatings from hydrophilic to hydrophobic by blending of aminopropyl-terminated polydimethylsiloxane (ATP) with epoxy resins. However, the performance of the surface modifications of the epoxy coating was not investigated in terms of corrosion protection.

1.5 Brief introduction to electrochemical impedance spectroscopy (EIS)

EIS is a well-known quantitative method for protective properties examination of the anticorrosion performance of organic coatings(Skale et al., 2008). This method can give useful information about the protective coating properties based on the response of the electrochemical system to small voltage perturbations of various frequencies.(Skale et al., 2008) The result of EIS is the impedance of the electrochemical system as a function of frequency. Usually impedance is described with an equivalent electrical circuit, constructed preferably by circuit elements with proper electrochemical background.(Kendig and Scully, 1990) In this work, EIS has been employed to characterize the anticorrosion performance of the coating materials prepared.

Impedance spectroscopy is the most valuable characterization tool for corrosion protection because of its ability in a single experiment to detect interfacial relaxation covering a wide range of relaxation times. In the practical perspective, the application of this technique in corrosion science has been applied the measurment of transfer function at sub-herz frequencies.Now instruments and techniques are available for investigating interfacial impedance at frequencies down to the 10^{-3}- 10^{-4} Hz region,

where relaxation involves absorbed intermediates and diffusing species.(Barsoukov and Macdonald, 2005)

1.6 Outline of this thesis

This Master's thesis focuses on the development of effective anticorrosion coating systems using polysiloxane based polymers as additives for epoxy polyamide coatings. In Chapter 1, a brief introduction to anticorrosion technology for marine environment and recent development of anticorrosion coatings in the literature has been described. In Chapter 2, synthetic routes to a series of polysiloxane derivatives are discussed. The experimental work has clearly elucidated that the detailed molecular structures of the prepared polysiloxane materials, which are supported by various characterizations such as proton nuclear magnetic resonance (^{1}HNMR), gel permeation chromatography (GPC), Fourier transform infrared spectroscopy (FTIR), thermogravimetric analysis (TGA) atomic force microscopy (AFM), scanning electron microscopy (SEM), and contact angle experiments. The anticorrosion performance of the polysiloxane additives has been studied by EIS, the details of which are described in this chapter as well. In Chapter 3, a side project in my master program will be described. This project is based on the thesis work of former Master student, Youself, in Prof. Zhao's research group. This project aims to investigate the optimal ratio between two monomers of the copolymer in order to efficiently detect different metal cations. In Chapter 4, a 3D software package (BEASY) is used to evaluate the performance the newly designed polysiloxane-epoxy coatings in cathodic protection systems. The boundary element method is employed to describe the governing

mathematical model. Finally, Chapter 5 presents a summary and conclusions for this dissertation work, while perspectives on further research are offered. In particular, a number of new directions worthy of pursuit are suggested based on the findings of this thesis work.

Chapter 2 Modified Polysiloxanes as Additives for Epoxy Polyamide Coatings

2.1 Introduction

Epoxy resins are one of the most widely used polymers in coating applications owing to their good adhesion, high mechanical strength, and strong heat and chemical resistance. However, common epoxy resins show poor UV resistance and undesired water moisture affinity, which may lower their performances as anticorrosion coatings. To solve these problems, various surface modification methods of epoxy resins can be performed, and these methods usually do not alter the bulk properties of epoxy resins. Compared to other surface modifications like metal depositions, plasma treatment, and surface graftings, polymer blends are versatile in creating surface morphologies and property enhancements. In a common polymer blend, polymer A mixes with polymer B and cures. Polymer B must have relatively lower surface energy than A to segregate to the surface region during the curing process.

Second, the structures and relative molecular weights of the polymers affect the surface compositions and patterns. Because the bulk ratio of pigment B may also play an important role in determining the final surface, careful formulations are also needed. Moreover, pigment B in the resulting surface may be vulnerable due to the lack of interactions with polymer matrix A. The surfactant, for example, may be washed away by solvents. In the case of surface graftings, polymer B is applied to a preformed polymer matrix A and forms covalent bonds with it. The method requires suitable

functional groups installed in matrix A. If polymer B is installed before curing, then it must be tolerated in the curing process, and more importantly it cannot deteriorate the properties of the matrix resins. If polymer B is installed after curing, then the choice is quite limited by the surface treatments. Either way, polymer B imposes considerable difficulty in the design and synthesis.

To address these issues and provide another possible way for surface modifications, we have designed and synthesized two new polysiloxane polymers, namely eugenol-modified polysiloxane EU and eugenol-ethoxysilane-modified polysiloxane ES. These polymers have been found to react with epoxy resins and migrate to the surface during the curing process.

2.2 Experimental Section

2.2.1 Materials

Polymethylhydrosiloxane (PMHS), eugenol, triethoxyvinylsilane, and chloroplatinic acid were purchased from Sigma-Aldrich. Unmodified liquid epoxy resin (a diglycidyl ether of bisphenol A, EPON 828), and a polyamide curing agent (EPIKURE 3115) were provided by Momentive Specialty Chemicals. All solvents were reagent grade and used as received. Steel test panels were supplied by Q-Lab and were washed with acetone and dried in a desicator for 24 h before used.

2.2.2 Synthesis of eugenol-modified polysiloxane P1

Eugenol-modified polysiloxane P1 was synthesized by a hydrosilylation of PMHS with eugenol. In a typical experiment, PMHS (2.0 g), eugenol (6.0 g), and Speier's catalyst (a solution of H_2PtCl_6 in isopropanol, 0.04 mL, 10 mg/mL) were mixed and stirred for 48 h. The resulting mixture was diluted with dichloromethane, and then loaded onto a short silica column for separation. Excess starting materials were removed by dichloromethane wash, and polymer P1 was obtained, after washing with ethyl acetate, as pale yellow thick oil.

^{1}HNMR (500 MHz, $CDCl_3$): δ 6.67 (s, 1H), 6.57 (s, 2H), 5.43 (s, 1H), 4.68 (s, 0.13H), 3.73 (s, 3H), 2.46 (s, 2H), 1.57 (s, 2H), 0.49 (s, 2H), 0.05 (s, 3H); ^{13}CNMR (75 MHz, $CDCl_3$): δ 146.5, 143.8, 134.5, 121.1, 114,3, 111.2, 55.9, 39.4, 25.5, 17.6, 2.1, 0.2; FTIR (KBr): 3504, 3422, 2957, 2926, 2858, 2152, 1607, 1512, 1460, 1429, 1367, 1259, 1232, 1151, 1076, 1018, 907, 843, 781 cm^{-1}; GPC: M_n = 4100, PDI = 2.3.

2.2.3 Synthesis of eugenol-ethoxylvinylsilane-modified polysiloxane P2

Eugenol-ethoxylvinylsilane-modified polysiloxane P2 was synthesized by a hydrosilylation of PMHS with eugenol and triethoxyvinylsilane (see Scheme 2-1). In a typical experiment, PMHS (2.0 g), eugenol (5.0 g), triethoxyvinylsilane (2.0 g), and Speier's catalyst (0.04 ml, 10 mg/ml) were mixed and stirred for 48 h. The resulting mixture was diluted with dichloromethane, and then loaded onto a short silica column for separation. Excess starting materials were removed by dichloromethane wash and polymer P2 was obtained,after washing with ethyl acetate, as a pale yellow thick oil.

^{1}HNMR (500 MHz, $CDCl_3$): δ 6.76 (s, 1H), 6.58 (s, 2H), 5.49 (s, 1H), 3.76 (s, 5H), 2.48 (s, 2H), 1.58 (s, 2H), 1.18 (s, 3H), 0.52 (s, 3H), 0.05 (s, 4H); ^{13}CNMR (75 MHz, $CDCl_3$): δ 146.5, 143.8, 134.6, 121.1, 114,3, 111.2, 58.6, 55.9, 39.4, 25.5, 18.5, 17.6, 2.1, 0.2; FTIR (KBr): 3518, 3412, 2953, 2926, 1607, 1514, 1456, 1429, 1367, 1259, 1234, 1148, 1072, 1015, 955, 843, 766 cm^{-1}; GPC: M_n = 5900, PDI = 3.1.

2.2.4 Preparation of P1/P2 incorporated epoxy coating

The synthesized polymer P1/P2 was added into an EK3115 solution in xylenes (70 wt%). To the mixture was added an EPON 828 solution in xylenes (70 wt%) in the stoichiometric ratio. The contents of P1/P2 in the incorporated epoxy coating was 1~2.5 wt%. Then 1-butanol (5 wt% of the coating) was added and the mixture was stirred for 2 h. It was then applied on steel test panels by brush. The coated panels were allowed to cure at room temperature for 7 days and then stored in desiccators for at least 24 h before tests. As a control, a set of panels was coated with epoxy resins without P1/P2.

2.2.5 Characterizations

Fourier transform infrared spectra (FTIR) were recorded on a Bruker Tensor 27 spectrometer equipped with a ZnSe ATR module. ^{1}H and ^{13}C NMR spectra were measured on a BrukerAvance 500 MHz spectrometer or a Tecmag APOLLO 300 MHz spectrometer with chloroform-*d* as solvent. Gel permeation chromatography (GPC) measurements were performed on a VISCOTEK GPC Max 2001 system with TDA 305 triple detector array using polystyrene standards with THF as eluent.

Thermogravimetric analysis (TGA) was conducted on a TA Instruments Q500 thermogravimetric analyzer from 25 ^{o}C to 600^{o}C in an inert atmosphere with a heating rate of 20 C^{o}/min. Atomic force microscopy (AFM) images were taken with a Q-Scope AFM operated in tapping mode. Scanning electron microscopy (SEM) images were taken with a Hitachi S570 scanning electron microscope operated at 10 kV. Water contact angles were taken by procedures described in the literature. Coating thickness measurements were done by using a coating thickness tester (ST156, REED). The panels with coating thickness 40 μm were selected for corrosion studies. Electrochemical impedance spectroscopy (EIS) was performed on a MetrohmAutolabpotentiostat with FRA32M at open circuit potentials over the frequency range of 10kHz to 0.1 Hz with a signal amplitude of 10 mV. The three-electrode electrochemical cell consisted of a coated steel panel as a working electrode with an electrode surface of 19 cm^2, a stainless steel counter electrode, and a Ag/AgCl reference electrode. An aqueous NaCl solution (3.5 wt%) was used as electrolyte solution. A Faraday cage was used to shield the cell from external noise effects. The impedance data were analyzed by NOVA software provided by MetrohmAutolab.

2.3 Results and discussion

2.3.1 Characterization of modified polysiloxanes P1 and P2

The FTIR spectrum of polymer P1 (see Figure 2-1) shows a weak absorption of Si-H stretching at 2140 cm^{-1}, suggesting the hydrosilylation of PMHS with eugenol did not come to completion under the reaction conditions. Based on the integration of Si-H

at 4.7 ppm in the ^{1}H NMR spectrum, the content of Si-H residue is estimated to be 11% (mol). In contrast, the FTIR spectrum of P2 shows no absorption at 2140 cm^{-1} and the ^{1}H NMR spectrum of P2 displays no peak at 4.7 ppm. These results indicate a higher Si-H conversion in the synthesis of P2, probably owing to insignificant steric effects imposed by triethoxyvinylsilane. Analysis of the ^{1}H NMR spectrum of P2 suggests that during the reaction, 75% of Si-H reacted with eugenol and 25% reacted with triethoxyvinylsilane. Note that the molar ratio of starting eugenol and tirethoxyvinylsilane was roughly 3:1. It may be a hint that the hydrosilylation of PMHS is non-selective towards these vinyl substrates, which allows the control of the P2 structure by varying the concentration of vinyl substrates.

Based on GPC analysis results, polymer P2 has a significantly larger molecular weight than P1, which is difficult to explain solely by higher Si-H conversion and the larger molecular weight of triethoxyvinylsilyl groups. Also, the polydispersity index (PDI) of P2 (3.1) is higher than P1 (2.3). It may indicate a higher degree of cross-linking within P2, likely due to condensations involving triethoxysilyl moieties.

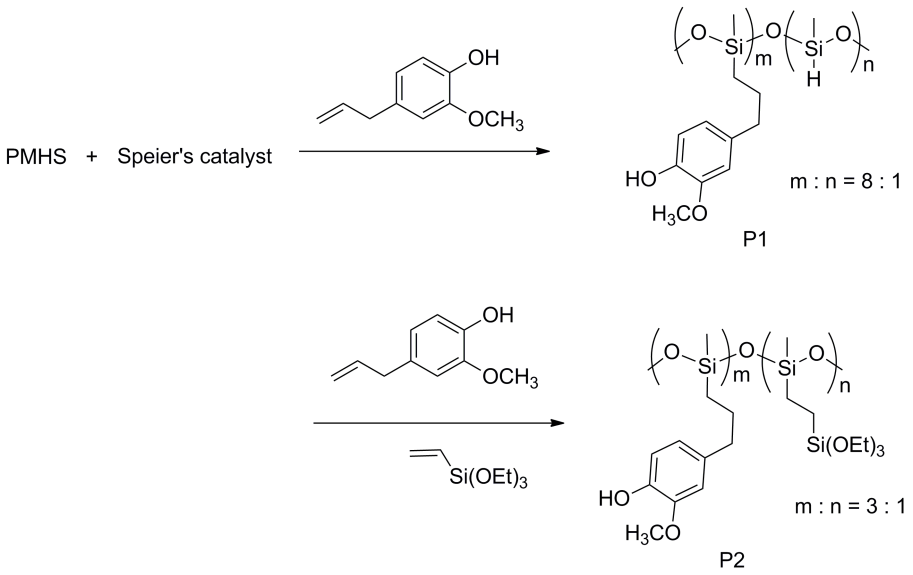

Scheme 2-1 Synthesis of polymers P1 and P2 by hydrosilylation of PMHS

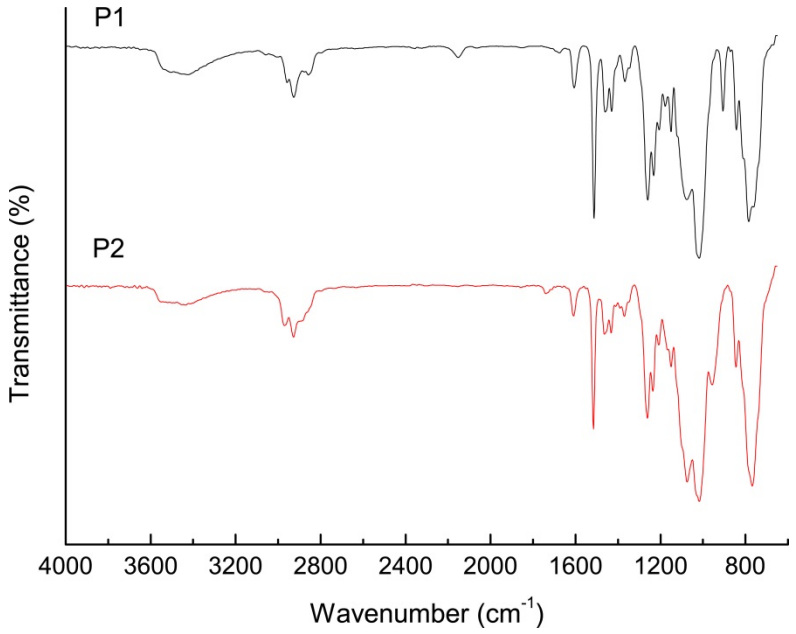

Figure 2-1 FTIR spectra of polymers P1 and P2

2.3.2 Characterization of modified epoxy coatings

All cured epoxy coatings with/without polymers P1/P2 were colorless and transparent, indicating no macroscopic phase separations.

2.3.2.1 Infrared spectroscopy

The FTIR spectra of the unmodified epoxy coating (ER), the epoxy coating with 2.5 wt% polymer P1 (ER-2.5P1), and the epoxy coating with 2.5 wt% polymer P2 (ER-2.5P2) show almost the same pattern in the region below 3000 cm^{-1} (see Figure 2-2). The absence of epoxide absorption at 917 cm^{-1} confirms that all epoxy coatings were fully cured. And the small increase of the relative absorption at 1512 cm^{-1}, which is corresponding to the phenolic aromatic skeleton, is consistent with the addition of P1/P2. In the meantime, the absorptions bands above 3000 cm^{-1}, which are due to O-H and N-H stretching modes, shift towards the higher frequency region. As unmodified epoxy coating ER givesa vibrationalband at 3301 cm^{-1}, the band of P1 shifts to 3393 cm^{-1}, and the band of P2 shifts to 3436 cm^{-1}. The relative intensity of thesevibrational bands also increase significantly in the presence of P1/P2. The results may suggest weakening of the hydrogen bonding in the coatings after addition of P1/P2. As part of the curing process, P1/P2 may be incorporated into the epoxy resin by epoxide ring-openings and silanol condensations. The resulting epoxy resin may show weaker hydrogen bonding interactions due to the steric effect and the hydrophobic nature of the silicon parts which is not compatible with the hydrophilic backbone of epoxy resin. Compared to P1, P2 has triethoxyvinylsilyl groups that are more capable of

participating in silanol condensations, which in turn may result in a more cross-linked system and affect a larger portion of the epoxy resin.

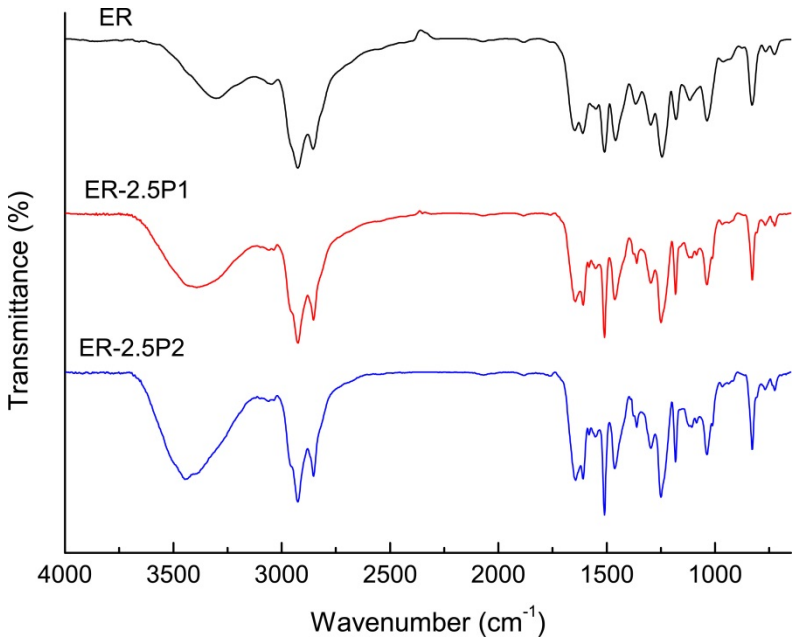

Figure 2-2 FTIR spectra of cured epoxy resins with/without 2.5 wt% P1/P2

2.3.2.2 Thermal stability

The TGA of cured epoxy coatings all show two-step degradations (see Figure 2-3). The initial decomposition temperatures (T_d) corresponding to 5% weight loss of the epoxy coating, is 307 ^oC for ER, 305 ^oC for ER-2.5P1, and 304 ^oC for ER-2.5P2. The close values suggest that P1/P2 has little effect on the initial decomposition temperature of the epoxy coatings. The temperatures corresponding to the maximum rates of weight loss (T_{max}), however, change moderately in the presence of polymer P1/P2. Unmodified ER gives T_{max1}at 385 ^oC in the first degradation step and T_{max2}at 451 ^oC in the second degradation. Polymer P1 increases T_{max1} by 16 ^oC and T_{max2} by 6

^{o}C, and P2 increases T_{max1} by 22 ^{o}C and T_{max2} by 14 ^{o}C. The data shows that polymers , even at a low concentration (2.5 wt%), can noticeably improve the thermal stability of the epoxy resin. The well-known thermal stability of the -O-Si-O- bonds can partially account for the enhanced thermal stability of the mixed polymers. In addition, the silica matrix formed by condensations of P1/P2 during the curing process, once carbonized at high temperatures, may act as shields to delay the further thermal degradation of the trapped epoxy resins. Polymer P2, bearing triethoxysilyl units, is more capable of forming a cross-linked system so it is more effective in terms of thermal stability enhancement. The residue yield (Y_c) at 600 ^{o}C of the coatings are similar, of which the highest is from ER-2.5P2 (23%), the middle from ER (22%), and the lowest from ER-2.5P1 (20%). It is worth noting the relatively lower Y_c of ER-2.5P1 may be a result of higher maximum decomposition rate in the second degradation step.

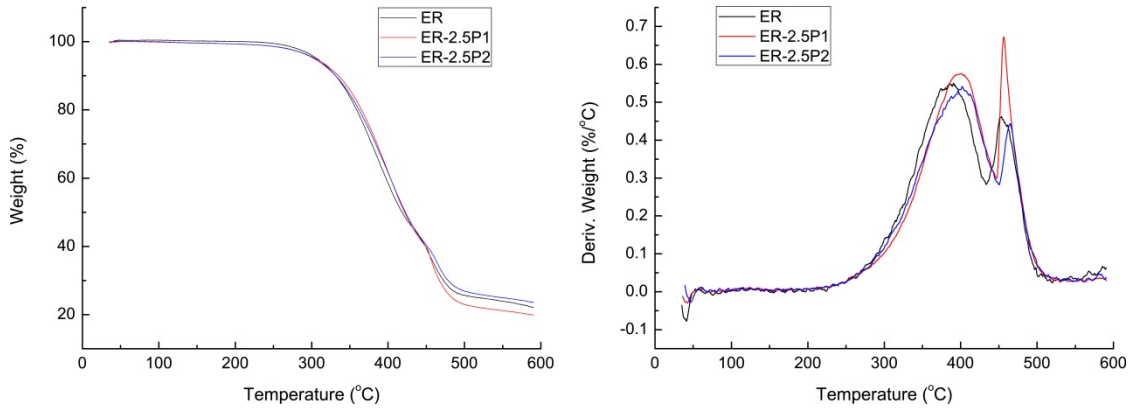

Figure 2-3 TGA traces (left) and derivatives (right) of epoxy coatings with/without P1/P2

Table 2-1 Selected data from TGA of epoxy coatings with/without P1/P2

Coating	T_d (^oC)	T_{max2} (^oC)	T_{max2} (^oC)	Y_c (%)
ER	307	385	451	22
ER-2.5P1	305	401	457	20
ER-2.5P2	304	407	465	23

2.3.2.3 Morphology of epoxy coatings

The morphology of coated steel panels was probed by AFM and the results are very interesting (see Figure 2-4). The AFM image of the unmodified epoxy coating ER reveals a featureless surface morphology. In contrast, the coating ER-2.5P1 exhibits an ordered surface pattern featuring well-dispersed "dimples". The shapes of these samples are close to spherical, with diameters varying from 90 to 180 nm and depths between 5 to 10 nm. The surface of coating ER-2.5P2 also has a similar dimple pattern but with a much wider diameter range from 110 to 300 nm. The depth of the dimples is between 10 to 25 nm. It is known that polymer additives with hydrophobic natures tend to migrate to the coating surface. Thus, it is hypothesized that the formation of surface dimple pattern results from the enrichment of P1/P2 to the surface followed by phase separations. In the polymer coating, some of the polysiloxane components settle down on the surface, while others are absorbed into the resin matrix during curing process leading to the formation of dimple-like morphology. The size distribution of the dimples may depend on many parameters that dictate the phase separation. One of

them is the structure of P1/P2. Elucidation of the detailed mechanism may require more information to be characterized about the surface composition, and this investigation will be conducted in the future work.

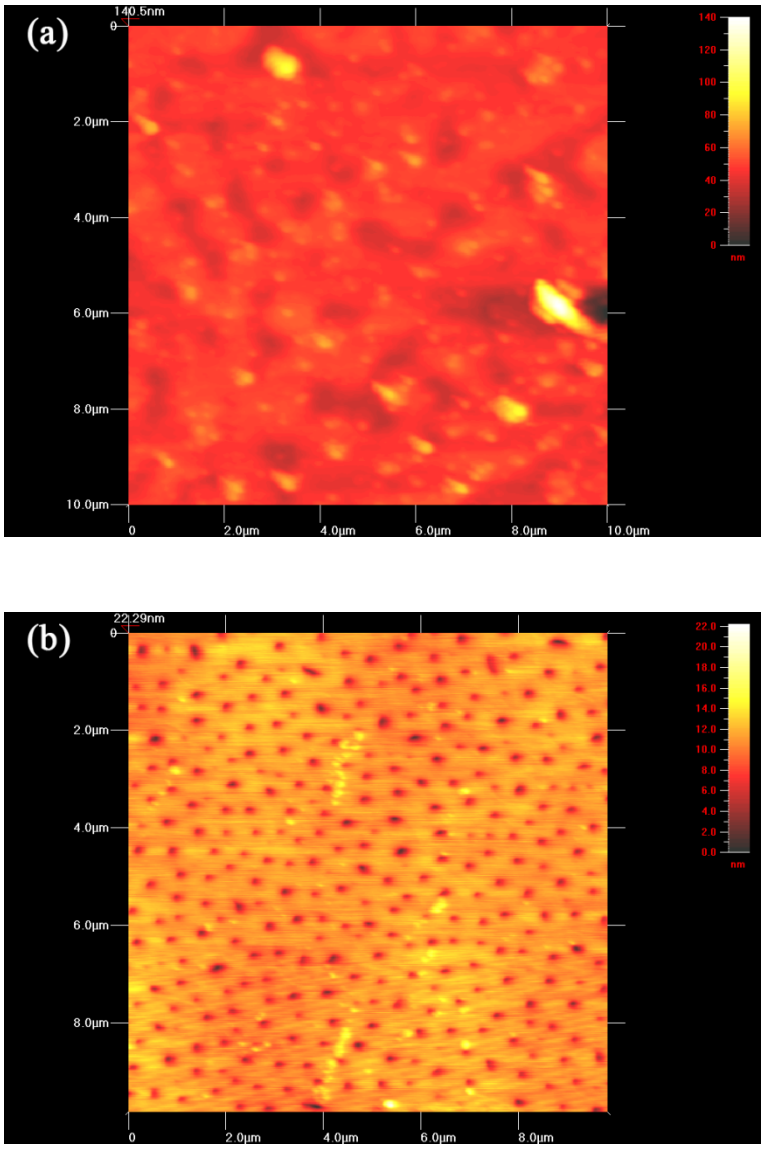

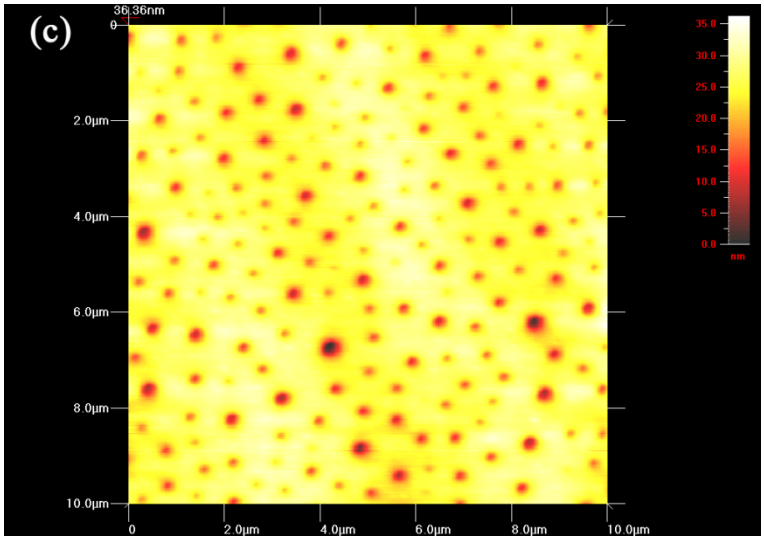

Figure 2-4 AFM images of epoxy coatings: (a) ER; (b) ER-2.5P1; (c) ER-2.5P2

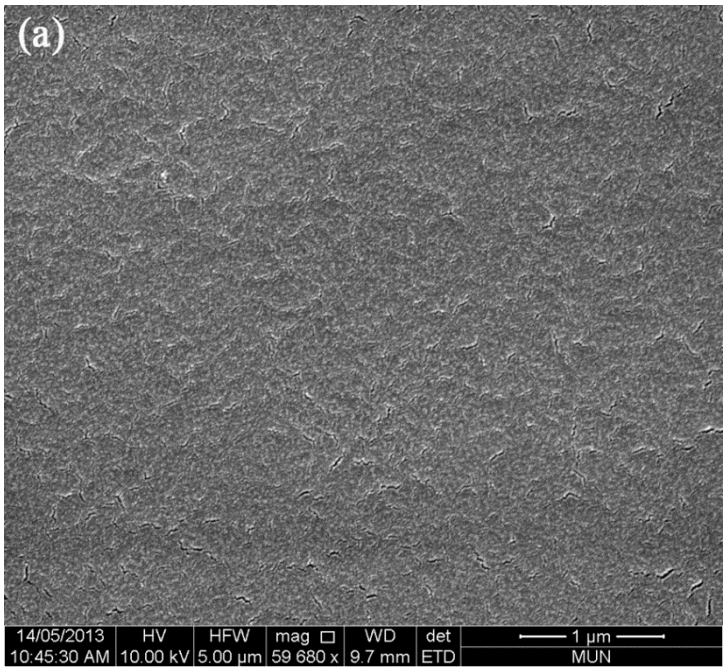

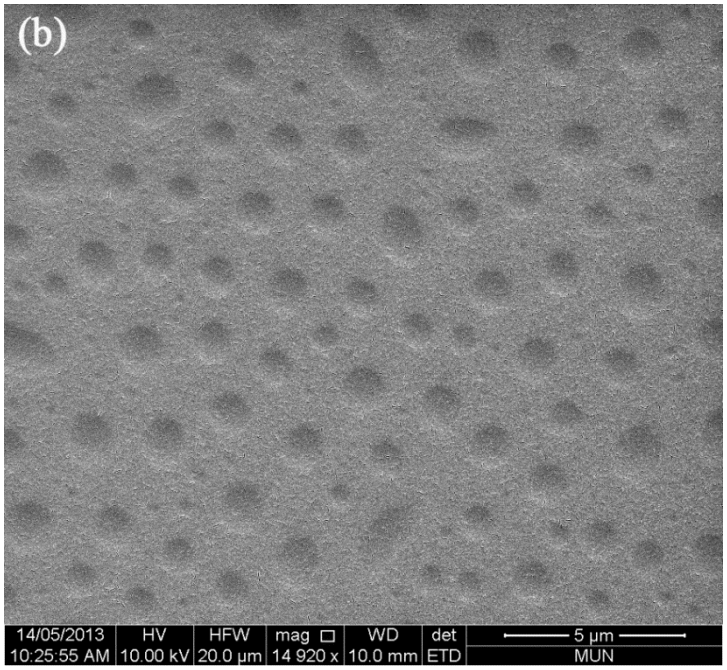

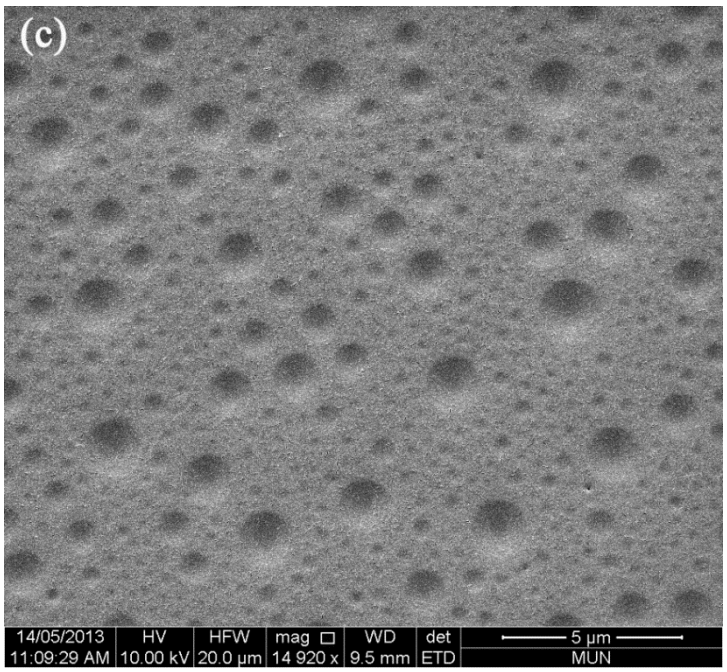

Figure 2-5 SEM images of epoxy coatings: (a) ER; (b) ER-2.5P1; (c) ER-2.5P2

The SEM images of epoxy coatings (see Figure 2-5), which were applied to small cut steel panels (1.5×1.5 cm^2) by dip casting, are in good agreement with the AFM results. Unmodified epoxy coating shows no distinguishable surface pattern, while both modified epoxy coatings have spherical dimples on the surface. However, these dimples are significant larger than the ones observed in AFM imaging. Some dimples observed in ER-2.5P2 even have diameters over 2 μm. Clearly, other factors during curing process have come into play. Nevertheless, the size distribution of the dimple-like patterns is retained to some extent; that is, when most dimples on ER-2.5P1 surface have narrow diameter range, the dimple sizes on ER-2.5P2 vary significantly. In the SEM images, it is much clearer to observe the trend of the diameter distribution in ER-2.5P2. Most of the dimples are either very small or very large. It is assumed that the larger PDI value of P2 is a dominant factor accounting for this phenomenon. Nevertheless, other possible factors may also contribute and cannot be ruled out.

2.3.2.4 Hydrophobicity

The hydrophobicity of epoxy coatings was studied by water contact angle measurements. As shown in Figure 2-6, epoxy coating ER has a contact angle of 60^o. The incorporation of polymer P1 sharply increases the contact angle of the coating to 78^o, and the addition of P2 leads to a contact angle of 90^o. The increase of hydrophobicity may come from the migration of P1/P2 to the surface area. The inherent hydrophobic nature of the -O-Si-O- backbone in P1/P2 can significantly increase the hydrophobicity of the surface. In addition, the spherical dimples on the

coating surface may generate air/water interfaces when in contact with water, which may also contribute to the hydrophobicity enhancement. However, the contact angle does not exceed the threshold of 90^{o} for superhydrophobicity, either because the concentration of P1/P2 is low on the surface, or the hydrophobicity of backbone is partially attenuated by the phenolic appendages.

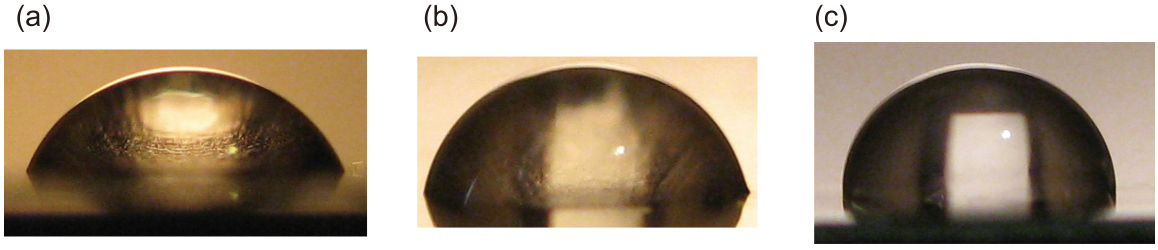

Figure 2-6 Water contact angle of epoxy coatings: a) ER; b) ER-2.5P1; c) ER-2.5P2

2.3.2.5 Corrosion studies

The performances of the epoxy coatings in terms of corrosion protection were investigated by EIS at open circuit potentials. Because ER-2.5P2 shows complex behaviour and the results are not always reproducible, discussions in the following section are mainly based on the EIS data for the epoxy coating ER-1P2 with 1 wt% P2. The detailed EIS study regarding ER-2.5P2 will be disclosed in due course.

2.3.2.6 Electrochemical impedance spectroscopy

As shown in Figure 2-7, the Nyquist plots for epoxy coatings ER, ER-2.5P1, and ER-1P2 show a partial capacitive loop in the first day of immersion in 3.5% NaCl. All epoxy coatings show good initial corrosion protection with the impedance values

higher than 10^7 ohm at 0.1 Hz and the minimum phase angles around -86°. It is clear that P1/P2 can greatly modify the initial corrosion resistance of the epoxy coatings. The coating ER-1P2 with the largest semicircle diameter manifests the highest enhancement of corrosion resistance. After 20 days of immersion, all coatings show decreased corrosion resistance. The coatings ER-2.5P1 and ER-1P2 remain intact with one loop, and the coating ER shows a second loop in the low frequency corresponding to corrosions on the metal surface.

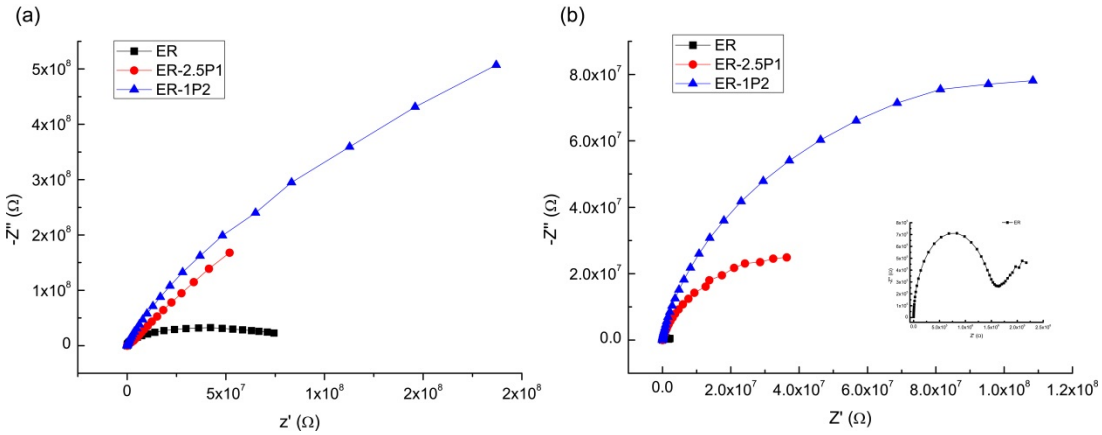

Figure 2-7 Nyquist plots for epoxy coatings ER, ER-2.5P1, and ER-1P2 after 0 day (a), and 20 days (b) immersion in 3.5% NaCl solution

Unmodified epoxy coating ER behaves in the same manner as typical organic coatings (Figure 2-8). It has a high impedance value of 7.8×10^7 ohm at 0.1 Hz, which drops half to 3.8×10^7 ohm after 1 day immersion. It is the first stage when water starts to penetrate the coating, but not yet reach the metal surface. The increased water content in the coating leads to an increase in the coating capacitance and a decrease in the coating resistance. The Bode phase plot shows only one time constant in the very

beginning, but after 1 day immersion, a second time constant is barely seen in the moderate frequency region. It is rare but not unprecedented that intact coatings can show two time constants (Hinderliter et al., 2006). As reported in the literature, a coating could possess two time constants simply due to the different properties of the water-saturated part and the deeper unaffected part of the coating. The second time constant disappears after a few days, probably because the coating is almost saturated with water and the difference within the coating is eliminated. After 6 days of immersion, the impedance value at 0.1 Hz drops to 2.6×10^6 ohm. In addition, a small peak appears in the Bode phase plot at frequencies between 0.1 Hz to 1 Hz. The new time constant indicates the process has progressed to the second stage, in which the electrolytes have reached the metal surface and corrosion on metal starts. After 20 days of immersion, the impedance value drops to 2.2×10^6 ohm as the corrosion beneath the coating moves on. The appearance of tiny corrosion pittings on the coated sample surface confirms the progress of this type of corrosion.

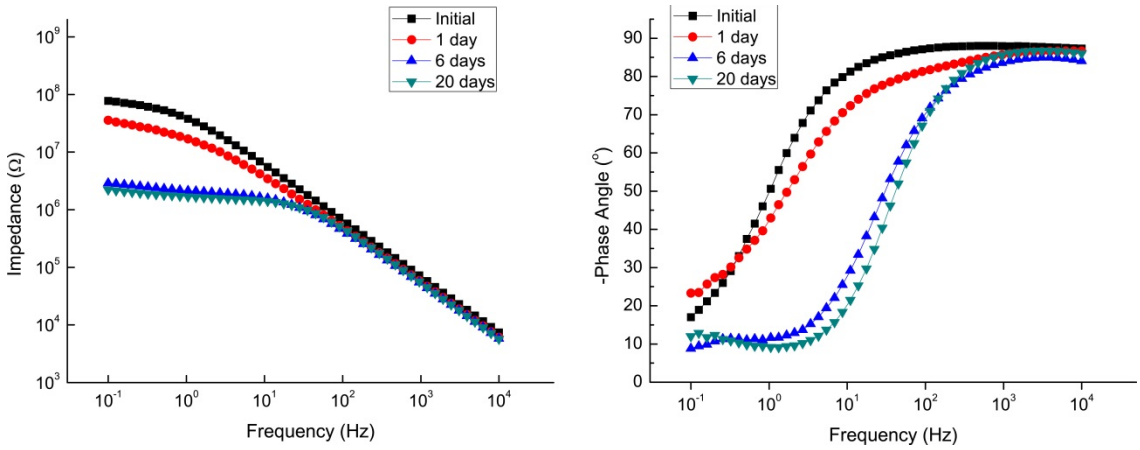

Figure 2-8 Bode plots for epoxy coating ER at different immersion time in 3.5% NaCl solution

Similar to the epoxy coating ER, the epoxy coating ER-2.5P1 has a high impedance value of 1.8×10^8 ohm at 0.1 Hz in the initial stage (see Figure 2-9). A large drop of impedance value to 7.4×10^7 ohm occurs after 1 day of immersion, and the value decreases with the immersion time. However, after 20 days of immersion, the impedance value still remains as high as 4.4×10^7 ohm, indicating a good coating durability. In contrast to ER, the coating ER-2.5P1 shows two time constants from the beginning as seen in the Bode phase plots and they remain within the experiment time frame. It is not clear whether the second time constant at the low frequency region is from the double layer capacitance related to the corrosion on the metal surface. The high impedance values at 0.1 Hz and the visual observation of the coating show no corrosion pittings after 20 days. It is evident that the coating ER-2.5P1 shows better corrosion protection than the unmodified epoxy coating ER. Therefore, if the second time constant is related to metal corrosion, it indicates that the barrier effect of the coating becomes weaker. However, the corrosion rate must be much slower than unmodified epoxy coatings, which can be ascribed to the good corrosion inhibiting effect of P1/P2. The second time constant also possibly result from two different parts of the coating, similar to the coating ER. In that case, the large difference in the two time constants may reflect the complexity of the coatings besides the simple effect caused by water penetration. Within coating ER-2.5P1, two parts may exist with different compositions, including the majority of the unmodified epoxy resins, and a combination of the P1 modified epoxy resins and some unmodified epoxy resins in contact with them. During the curing stage, a significant amount of P1 modified epoxy resins may migrate to the surface owing to the hydrophobic nature of the siloxane

skeletons, and they occupy the major area of the top part with the unmodified epoxy resins around them. In addition, some of the P1 modified epoxy resins enrich on the metal surface due to the phenol-metal or silanol-metal interactions, and some others distribute inside the coating matrix. In the meantime, the unmodified epoxy resins account for most of the coating matrix below the top part. So the water front does not move as in typical organic coatings. It can follow the interface beween the modified epoxy resins and the unmodified epoxy resins around them. Or it can, after passing the top part, penetrate the bulk unmodified epoxy resins imbeded with small modified epoxy resins. The difference in the two paths results in the two time constants. It is worth noting that by moving towards both directions water molecules may have chances to encounter residual silanol groups from the modified epoxy coatings, which in turn trigger silanol condensations to block the pathway. As seen in the Bode phase plot, the plots barely change from day 1 to day 6, and the phase angles after 20 days do not follow the same decreasing trend as others. This suggests a different change in the coating other than deteriorating. Most likely a self-healing process may take place.

The epoxy coating ER-1P2 shows comparable results with ER-2.5P1 as can be seen in Figure 2-10. The impedance value at 0.l Hz is 5.4×10^8 ohm at the beginning, and as high as 1.3×10^8 ohm after 20 days of immersion. The phase angle remains below -70^o over a wide frequncey range after 20 days of immersion. Not surprisingly, ER-1P2 also shows two time constants. Compared to ER-2.5P1, the coating ER-1P2 shows less significant difference in impedance between 6 days and 20 days of immersion. The data indictes ER-1P2 is more stable and resistant to water immersion.

It is believed that the triethoxysilyl groups in the coating material can enhance the barrier effect of the coating by increasing cross-linking density and it may furnish more silanol residues to slow down water penetration.

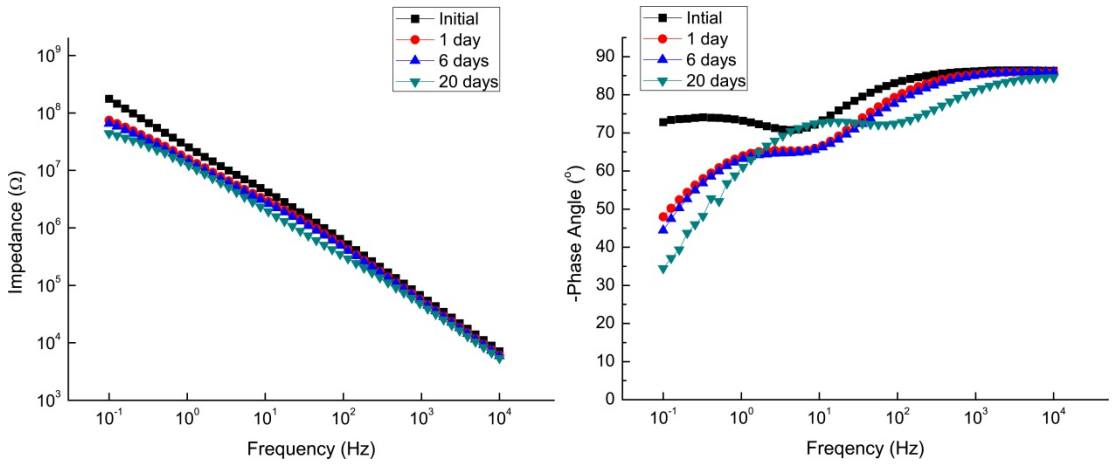

Figure 2-9 Bode plots for epoxy coatings ER-2.5P1 at different immersion time in 3.5% NaCl solution

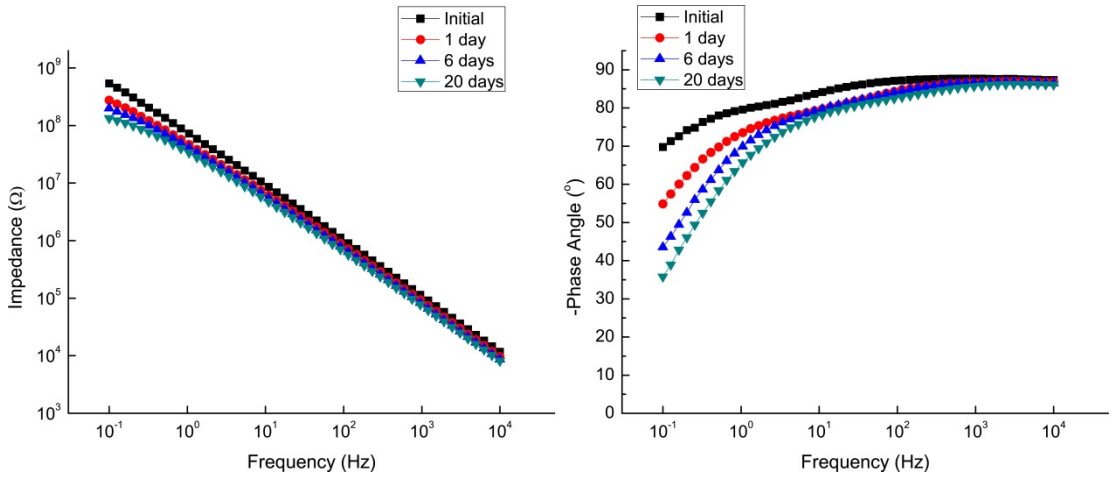

Figure 2-10 Bode plots for epoxy coatings ER-1P2 at different immersion time in 3.5% NaCl solution

To further evaluate the coating properties, the EIS data were fitted with equivalent electric circuits (EEC). For the EIS data of the coating ER in the beginning of the immersion with one time constant, a simple EEC model for typical organic coatings is adopted, which consists of a solvent resistance R_s in series with a parallel combination of a coating resistance R_c and a coating capacitance C_c (Figure 2-11a). For the data with two time constants in the intact coatings, several EEC models have been tried but failed to get a good fit including the one proposed in the literature for the coating containing water-saturated and intact parts. It is found that a simple addition of a parallel combination of a coating resistance R and a constant phase element (CPE) in series to the first coating resistance afford good fitting results (Figure 2-11b). The same model can be applied to the later stage in which metal corrosion starts and carries on. Herein, the CPE is substituted with the double layer capacitance C_{dl}, and the resistance in parallel is related to the charge transfer resistance R_{ct}.

For the coating ER-2.5P1, the EEC used for the coating ER in the second stage when both capacitances are substituted with the phase constant element (CPE) as shown in Figure 2-11c, produced excellent fits for most data during the whole immersion test. However, based on the CPE values obtained by fitting, the calculated values for the double layer capacitances are much smaller than typical ones. In fact, they are more similar to those of common organic coatings in values. The result may support the argument that the second time constant is not from corrosion on the metal. For this reason, the second CPE in the model is tentatively assigned to the inner part of the coating that is more intact. Interestingly, the same model does not fit the EIS data

for ER-1P2, suggesting the coatings are very different. Nevertheless, when the first CPE is substituted with a capacitor (Figure 2-11d), the EEC model provides a good fit.

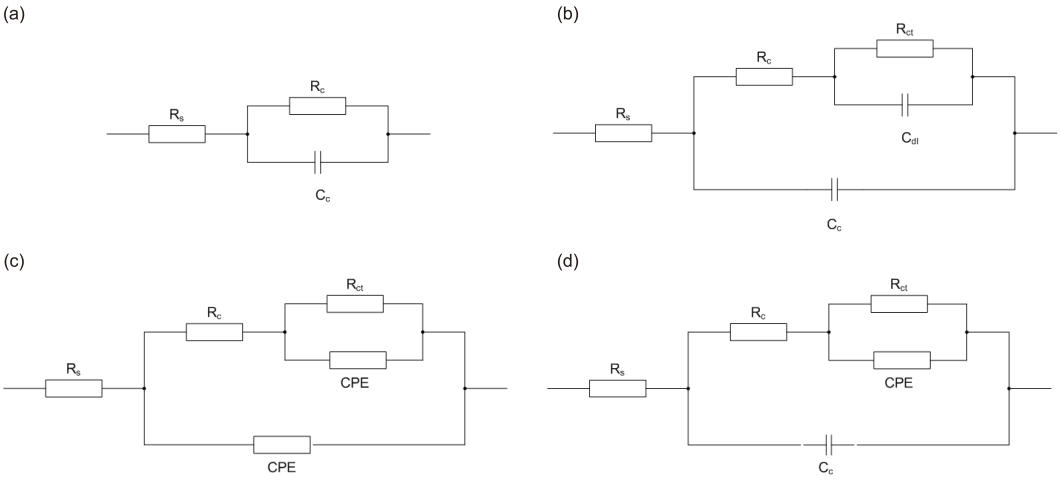

Figure 2-11 The EEC used for the fitting of EIS data of epoxy coatings: (a)(b), ER; (c), ER-2.5P1; (d), ER-1P2

2.4 Conclusion

Two eugenol-modified polysiloxane polymers were synthesized and used for the modification of commercial epoxy coatings. The cured epoxy coatings doped with the modified polysiloxanes showed a noticeable increase in thermal stability. In addition, the surface of modified epoxy coatings shows interesting spherical dimple-like microscopic patterns. Moreover, the hydrophobicity of the coatings was increased significantly, as evidenced by the increased water contact angles. The performances of commercial epoxy resin coatings in terms of corrosion protection were greatly enhanced after blended with a low percentage of modified polysiloxane additives. The detailed correction mechanisms have been studied by EIS analysis. Based on the

experimental results, it is believed that the modifiedpolysiloxane will be of great value for anticossorion applications. In particular, the eugenol-functionalized polysiloxanes are very cheap and easy to produce in large quantity. It is envisioned thatfurther investigations of this type of polysiloxane materials should lead to useful technology for corrosion control and optimization.

Figure 2-12 illustrates the corrosion rate for the three materials after 20 days immersion in sea water: regular epoxy coating (ER), epoxy coating with eugenol-modified polysiloxane(P1) andepoxy coatingwith eugenol-ethoxylvinylsilane-modified polysiloxane(P2). Some small areas of the epoxy coating (ER) plate have been corroded. Those plates protected by the epoxy P1/P2 coatings have good anti-corrosion resistance, Figure 2-12 (b) and (c) show the experimental test results.

(a)ER (b)P1 (c)P2

Figure 2-12 Corrosion results after 20 days immersion

(ER: epoxy coating, P1: epoxy with eugenol-modified polysiloxane coating.P2: epoxy with eugenol-ethoxylvinylsilane-modified polysiloxane coating)

Chapter 3 Synthesis and Characterization of a Series of Modified Poly(*p*-phenyleneethynylene)s (PPEs) as Fluorescence Chemosensors

3.1 Introduction

Conjugated polymers (CPs) have drawn enormous research attention over the past three decades. Due to the wide variety of applications such as solar cells(Chen and Hsu, 2011), single-walled carbon nanotube (SWNTs) dispersion (Liang et al., 2013), biological and chemical sensing (Pourghaz et al., 2011), and field effect transistors (FETs). (Thomas et al., 2007) In the case of fluorescence-based chemical sensing, CPs exhibit a prominent advantage of high detection sensitivity and easy measurement, owing to enhanced electronic communication between receptors and the polymer backbone, compared with small-molecule sensors. (Li et al., 2007) Relaxation from excited an electronic state to the ground state by the emission of photons is referred to as fluorescence, and chemosensors based on the change of fluorescence signal are called fluorescence chemosensors (Fan et al., 2009). In general, fluorescence chemosensors can be divided into two categories: turn-on sensors and turn-off sensors. (de Silva et al., 1997) In the turn-off system, the excited fluorophore carrying the free receptor(s) is highly fluorescent in nature. Upon the addition of the analyte, the LUMO energy level of the receptor/analyte pair is in between the HOMO and LUMO energy levels of the fluorophore, resulting in competitive non-radiative decay of the excited state and hence quenching of fluorescence. (Fan et al., 2009)

In the system of fluorescence “turn-on”, the non-bonding electron pair of the receptor can quench the fluorescence of the fluorophore via a rapid intramolecular charge transfer (ICT) from the receptor to the excited fluorophore, because the HOMO energy of the receptor is relatively high. Upon addition of an electron deficient analyte, such as a Lewis acid, the electron lone pair of the receptor can coordinate with the analyte, accordingly lowering the HOMO energy level of the receptor. Therefore, the binding of analytes gives increased fluorescence (Figure 3-1). (Fan et al., 2005) In practical uses, turn-on sensors do have some advantages over turn-off sensors, including the ease of detecting low concentrations cdue to the dark background, reduced false-positive signals, and enhanced sensitivity. (Pourghaz et al., 2011)

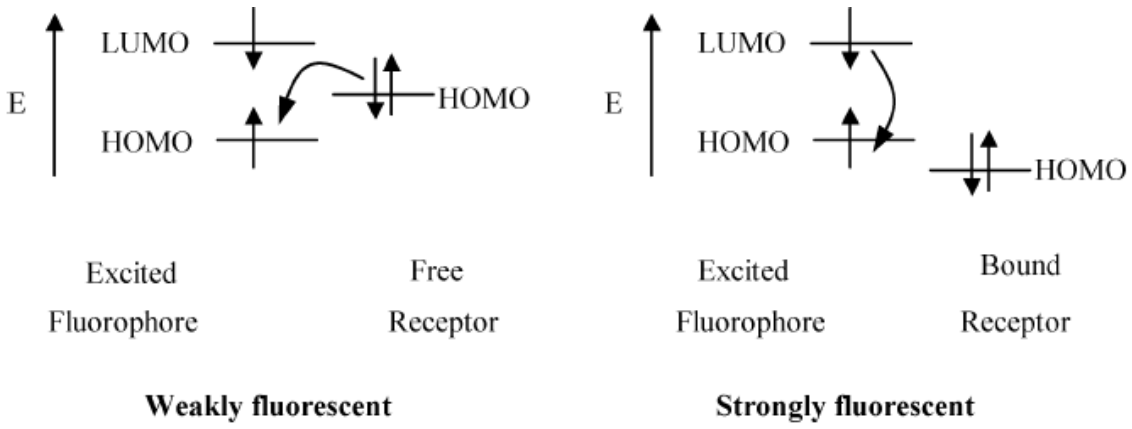

Figure 3-1 Schematic orbital energy diagram of a fluorescence turn-on sensor before and after binding with cation.(adopted from (Fan et al., 2005) with permission)

3.2 Objectives

In this chapter, I continued to work on the PPEs chemosensor project, which was previously investigated by a former Master's student, Yousef Pourghaz, in the Zhao research group in Department of Chemistry. His work showed that click reaction functionalized PPEs (polymer structures shown in Figure 3-2) are highly selective and sensitive fluorescence turn-on chemosensors for Zn^{2+} and Cd^{2+} ions (Pourghaz et al., 2011). Nevertheless, the performance of those PPE sensors still awaits optimization at the molecular level. One immediate objective after completing of his work was to further reduce the fluorescence background of the polymer sensors in solution and to increase the selectivity for larger-size cations. Accordingly, I focused my work on modification and introduction of different spacer lengths in the backbone of the polymer (target polymers shown in Figure 3-4). It was expected that such modified polymer sensors would selectively detect larger cations such as Cd^{2+}. Most importantly, the molecular structural design was aimed at reducing the number of receptors in one exciton migration path to the optimum length, such that it could lead to dramatically increased sensitivity (to reduce the detection limit of analyte).

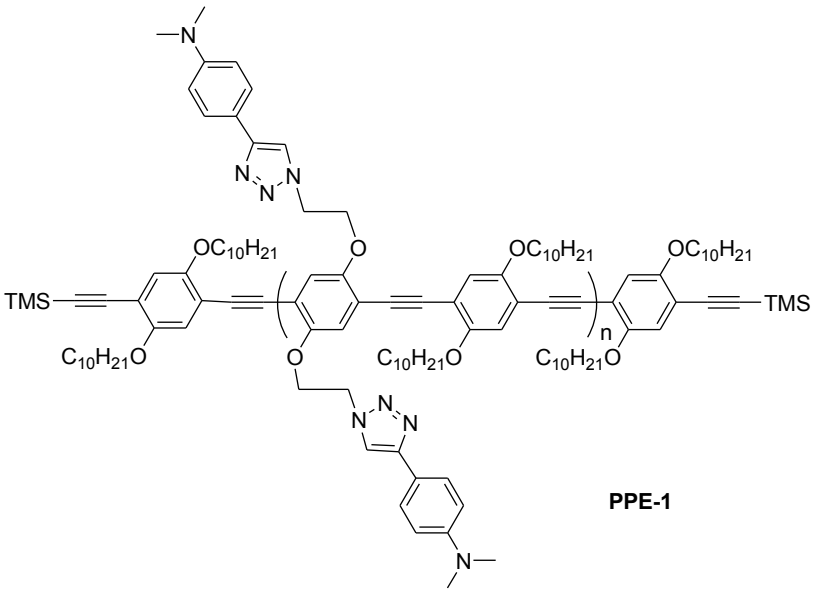

Figure 3-2 Molecular structure of modified sensors PPE-1.

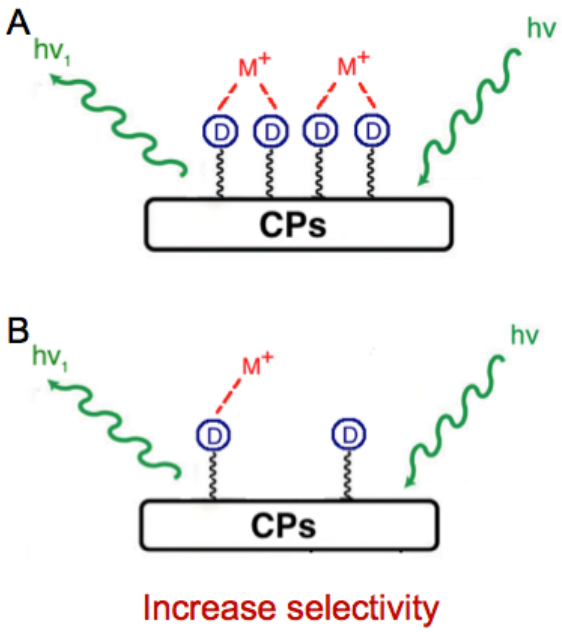

Figure 3-3 Scheme showing fluorescence selectivity for larger cations introduced by longer spacer.

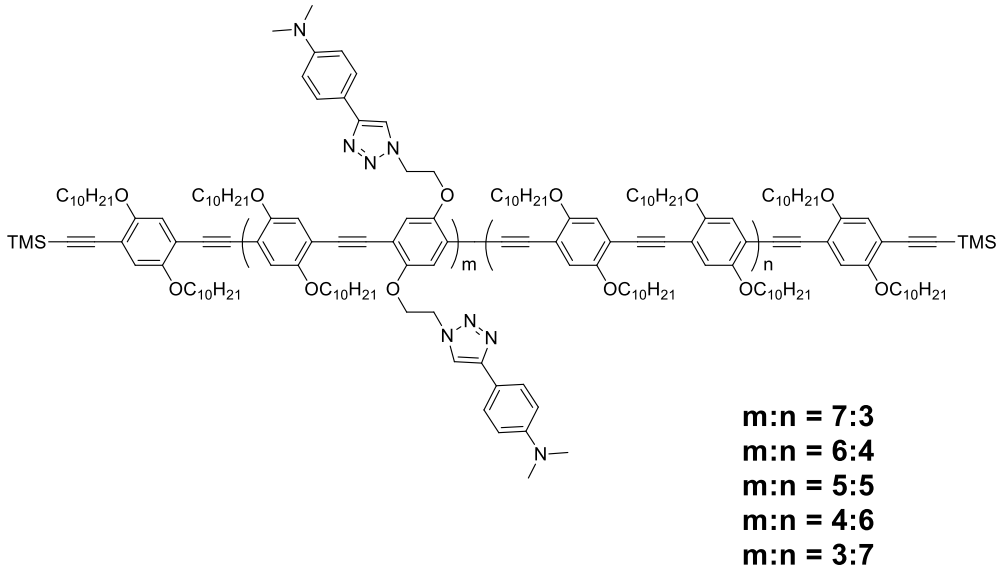

Figure 3-4 Molecular structures of target polymer sensors with different ratios of receptor groups on the polymer backbone.

3.3 Results and discussion

3.3.1 Synthesis

In order to make the target PPE polymers, a one-pot Sonogashira cross-coupling polymerization strategy was employed here. Three monomers (compound **3-9,** compound **3-11**, and compound **3-14**) were prepared at first (Figure 3-5).

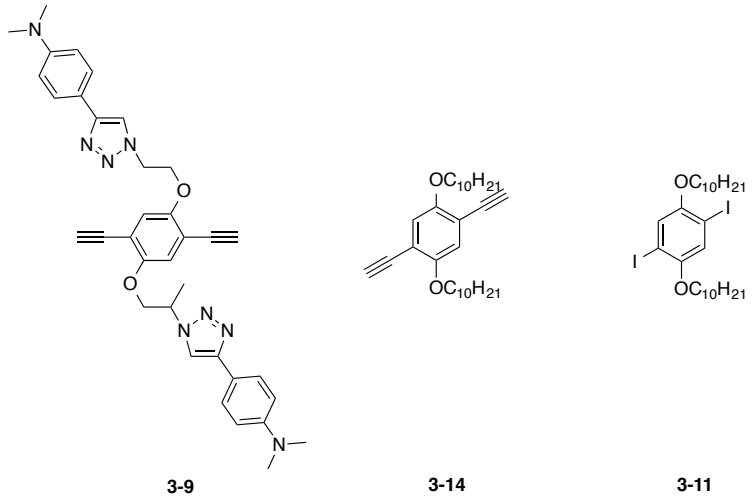

Figure 3-5 Monomers for polymerization reactions.

Compound **3-11** was obtained by alkylation of 1,4-hydroquinone followed by iodination catalyzed by $Hg(OAc)_2$ in dichloromethane (Scheme 3-1). In the first step, commercially available 1,4-hydroquinone was subjected to the alkylation reaction with 1-bromodecane in a basic ethanol solution to afford compound **3-10**. Then compound **3-10** was subjected to an iodination reaction in the presence of iodine chips and $Hg(OAc)_2$ to produce compound **3-11** in a moderate yield of 52%.

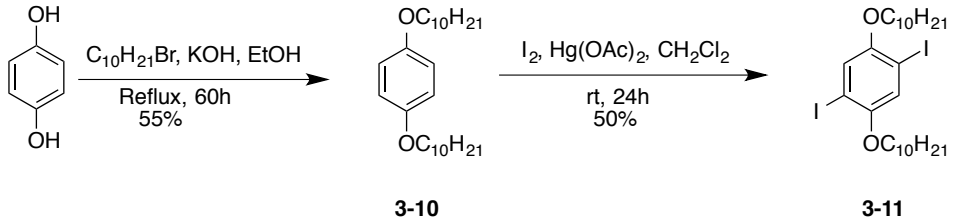

Scheme 3-1 Synthesis of monomer 3-11.

In order to achieve monomer **3-8** as shown in Figure 3-6**,** two more precursors, compound **3-3** and **3-7**, were required. The synthesis of compound **3-7** was described in Scheme 3-2. First, 1,4-bis(2-hydroxyethyloxy)benzene underwent an Appel reaction in the presence of CBr_4 and PPh_3 in acetonitrile at room temperature to give compound **3-4**. Then, compound **3-4** underwent iodination reaction in the presence of I_2 and $Hg(OAc)_2$ to afford compound **3-5**. Compound **3-5** was subjected to Sonogashira cross-coupling reaction with trimethylsilylacetylene (TMSA), using Pd(II) and CuI as catalyst and triethylamine as base, to afford compound **3-6**. Finally, the bromide groups of **3-6** were converted to azido groups with sodium azide to afford compound **3-7** in a good yield.

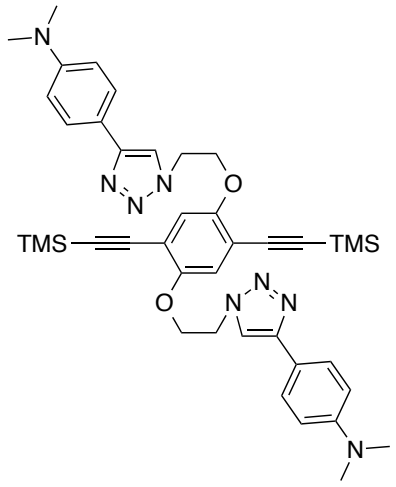

3-8

Figure 3-6 Molecular structure of monomers for 3-8.

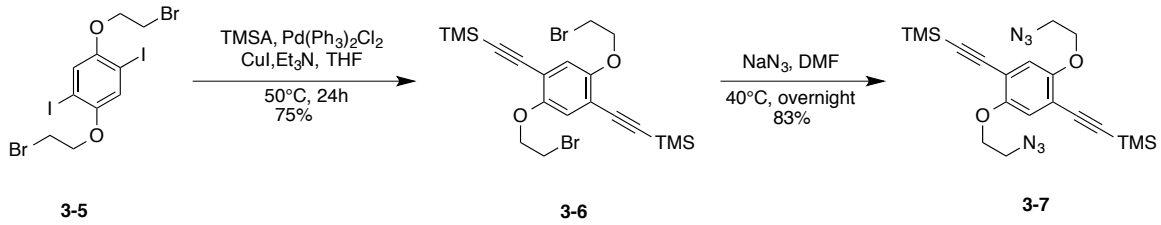

Scheme 3-2 Synthesis of compound 3-7.

In order to synthesize compound **3-3**, *N,N′*-dimethylaniline was subjected to iodination reaction in the presence of iodine chips in pyridine/dioxane mixture at room temperature to produce compound **3-1**. Compound **3-1** was then subjected to Sonogashira reaction with TMSA in the presence of Pd/Cu catalysts and piperidine as base to afford compound **3-2**. Compound **3-3** was obtained by desilylation of **3-2**, using potassium carbonate in methanol (Scheme 3-3).

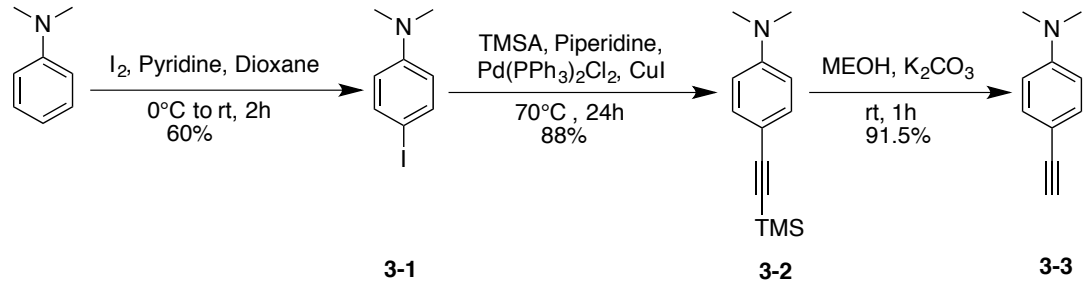

Scheme 3-3 Synthesis of compound 3-3.

Finally, a Cu-catalyzed alkyne-azide coupling (click) reaction was carried out between compound **3-7** and compound **3-3** in the presence of diisopropylethylamine (DIPEA) and CuI in DMF to obtain compound **3-8** (Scheme 3-4). Compound **3-8** was immediatelysubjected todesilylation reaction to achieve dialkyne **3-9** in the presence of

potassium carbonate and THF/MeOH at room temperature. The resulting product was soluble in both DMF and DMSO.

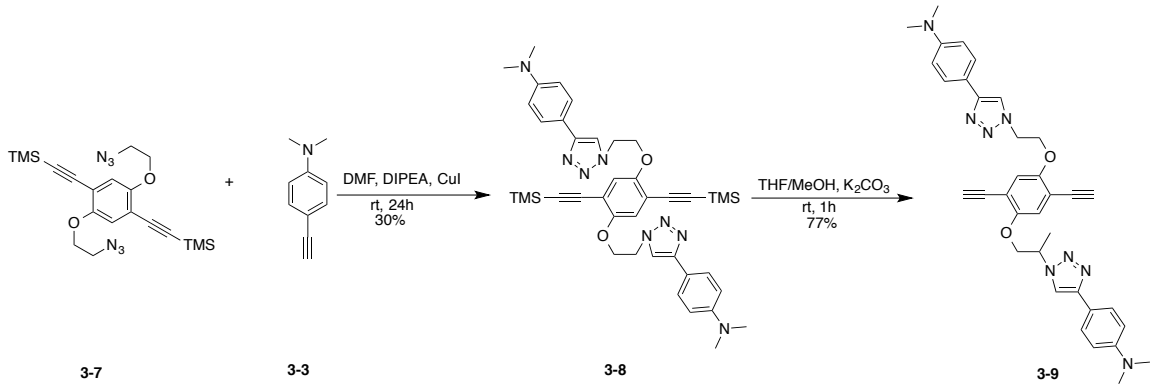

Scheme 3-4 Synthesis of compound 3-9.

Compound **3-14** was similarly prepared from a Sonogashira coupling reaction between compound **3-11** and TMSA, followed by desilylation to achieve compound **3-14** (Scheme 3-5). In addition, compound **3-12** acted as endcapping reagent in the final polymerization and was prepared from the Sonogashira reaction. Compound **3-11** was treated with 0.7 molar equivalent of TMSA in the presence of Et_3N and Pd/Cu catalysts to achieve compound **3-12** as the major product as shown in Scheme 3-6.

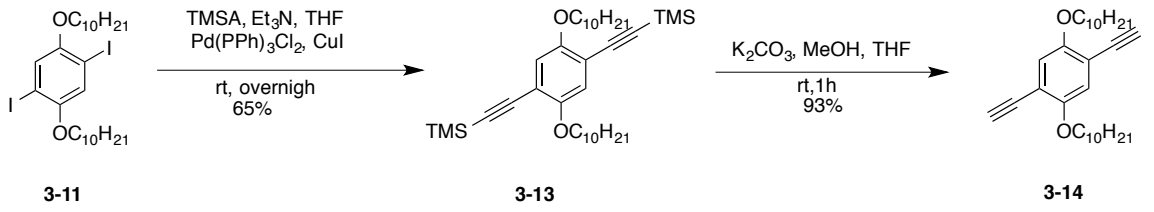

Scheme 3-5 Synthesis of compound 3-14.

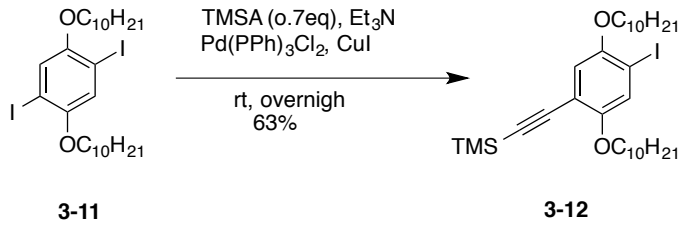

3-11 **3-12**

Scheme 3-6 Synthesis of compound 3-12.

Once all of monomers and endcapping reagents were acquired synthetically, one-pot Sonogashira polymerization was conducted (Scheme 3-7) using Pd (II) and Cu (I) as catalyst and piperidine as base, with 10% molar equivalent of endcapping reagent added to control the molecular weight and stability of final polymer. Most importantly, different ratios of three monomers were used to exert control over the number of receptors in one exciton migration length in order to enhance selectivity and reduce the fluoresence background. For example, 70% molar equivalent of **3-9**, 30% molar equivalent of **3-14**, and 100% molar equivalent of **3-11** were added for polymerization to achieve **P73**. Similarly, 60% molar equivalent of **3-9**, 40% molar equivalent of **3-14**, and 100% molar equivalent of **3-11** were added to polymerization to achieve **P64**.Also, 50% molar equivalent of **3-9**, 50% molar equivalent of **3-14**, and 100% molar equivalent of **3-11** were added to achieve **P73**. Since these polymers were highly p-conjugated, they tended to get stuck on the GPC column. Therefore, the molecular weights of the three polymers were not obtained by GPC.

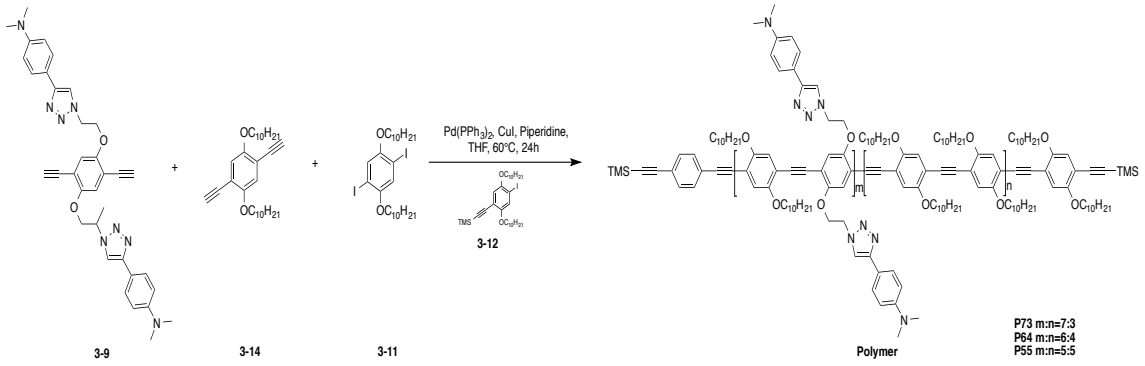

Scheme 3-7 Synthesis of polymer P73, P64, and P55.

3.3.2 Characterizations

Since the fluorescence background is very critical for polymer "turn-on" sensors, the fluorescence backgrounds of three polymers were initially checked. Upon irradiation with a UV lamp, highly diluted solutions of three polymers exhibited different backgrounds. That is, **P55** showed a very dark background, while **P73** and **P64** showed relatively strong background emission (Figure 3-14).

UV-Vis spectroscopy and fluorescence spectroscopy were used to monitor the spectral change upon titration of nearly non-emissive **P55** by various metal ions ranging from Zn^{2+}, Cd^{2+}, Cu^{2+} to Ba^{2+}, Na^{+} and Li^{+}. Titration spectra are shown below from Figure 3-7 to Figure 3-12. As can be seen, Cd^{2+} lead to the greatest fluorescence enhancement upon metal ion addition as depicted in Figure 3-7.

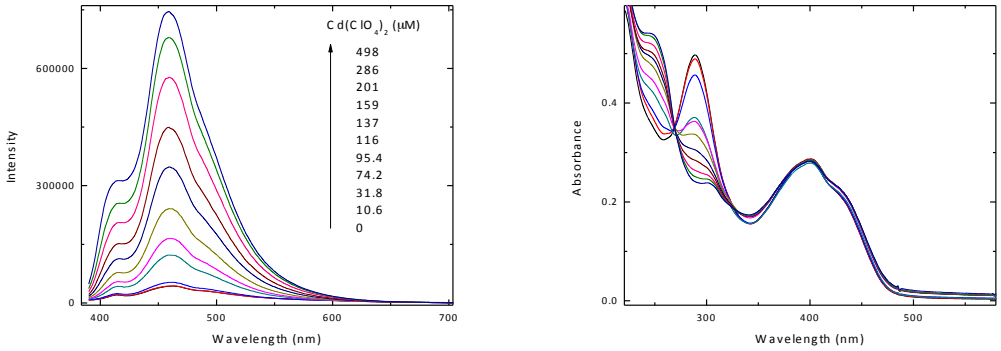

Figure 3-7 Fluorescence spectral (left) and absorption changes (right) of P55 (100 mg mL^{-1}, λ_{ex} = 380 nm) upon titration of $Cd(ClO_4)_2$ in THF.

According to Figure 3-7, **P55** exhibited the highest sensitivity towards Cd^{2+} ions among other ions and H^+. At the saturated point of the titration with Cd^{2+}, the fluorescence of **P55** gains a 17-fold enhancement at λ_{em} = 459nm. In contrast, **P55** only exhibited relatively low sensitivity to other ions and H^+ (1 to 6 fold enhancement) as shown from Figure 3-8 to Figure 3-12. In addition, Figure 3-13 summarized the decreasing trend of sensitivity of **P55** for various metal ions. This trend clearly showed that **P55** is a highly sensitive and selective chemosensor for Cd^{2+} ions in THF.

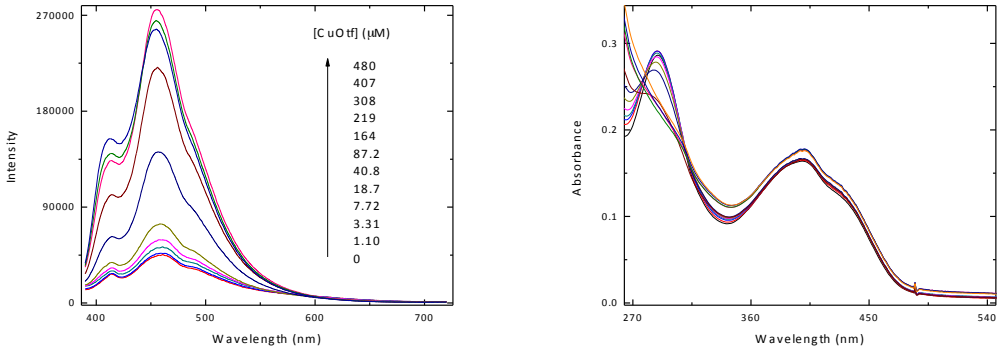

Figure 3-8 Fluorescence spectral (left) and absorption changes (right) of P55 (100 mg mL^{-1}, λ_{ex} = 380 nm) upon titration of Cu(OTf)$_2$in THF.

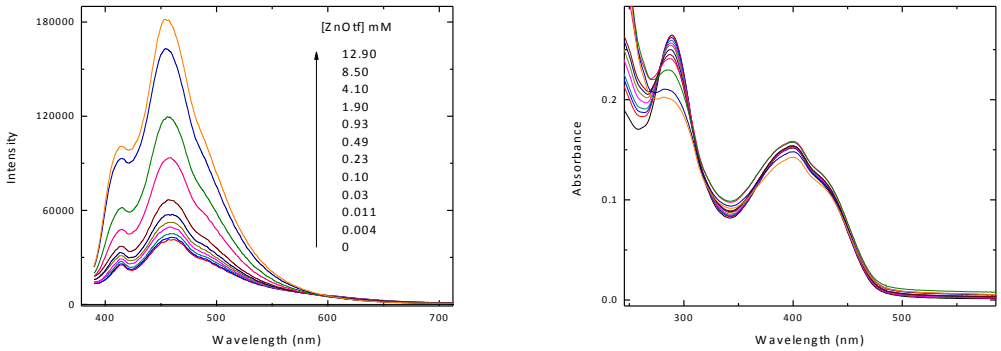

Figure 3-9 Fluorescence spectral (left) and absorption changes (right) of P55 (100 mg mL^{-1}, λ_{ex} = 380 nm) upon titration of Zn(OTf)$_2$in THF.

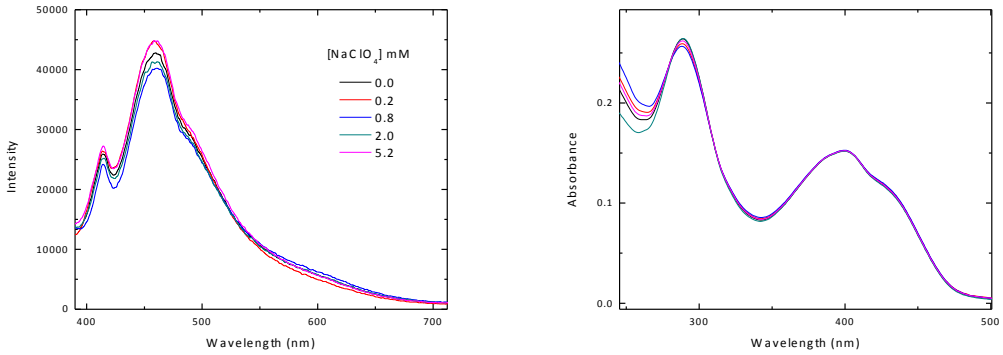

Figure 3-10 Fluorescence spectral (left) and absorption changes (right) of P55 (100 mg mL^{-1}, λ_{ex} = 380 nm) upon titration of $NaClO_4$ in THF.

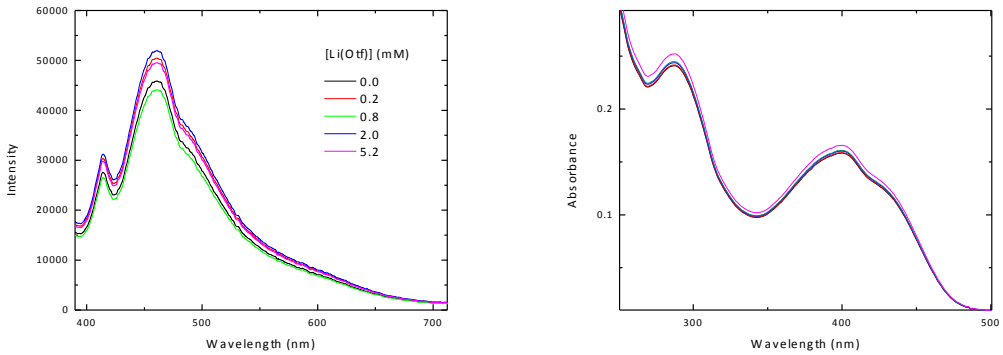

Figure 3-11 Fluorescence spectral (left) and absorption changes (right) of P55 (100 mg mL^{-1}, λ_{ex} = 380 nm) upon titration of LiOTf in THF.

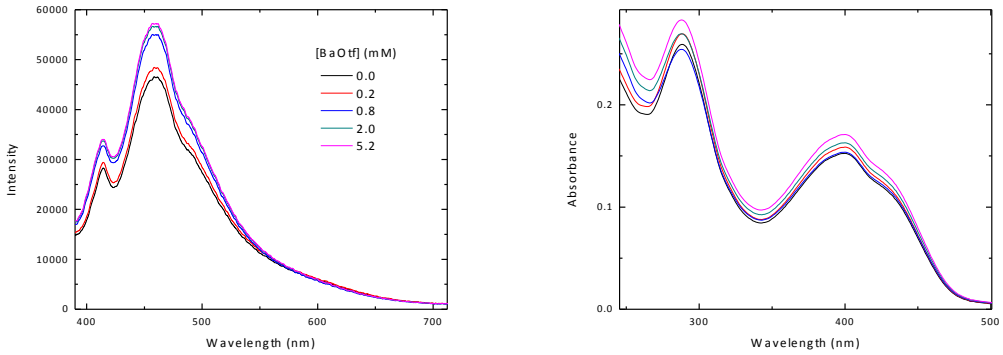

Figure 3-12 Fluorescence spectral (left) and absorption changes (right) of P55 (100 mg mL^{-1}, λ_{ex} = 380 nm) upon titration of Ba(OTf)$_2$ in THF.

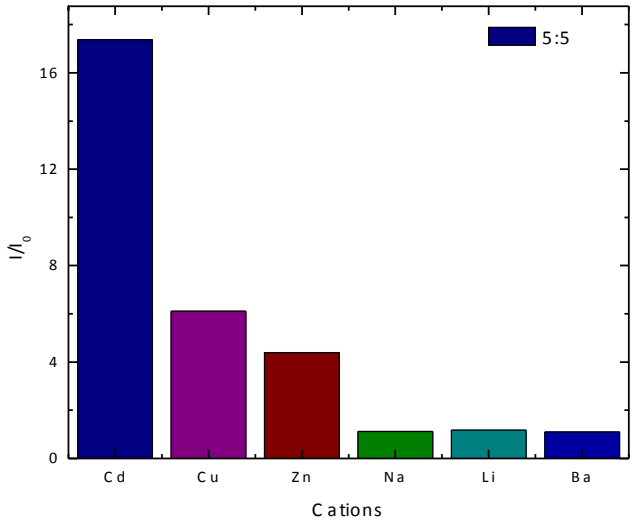

Figure 3-13 Trend of P55 fluorescence enhancement (I/I_0) for different cations at maximum emission wavelength (I: fluorescence intensity at the saturation point of titration; I_0: initial fluorescence intensity).

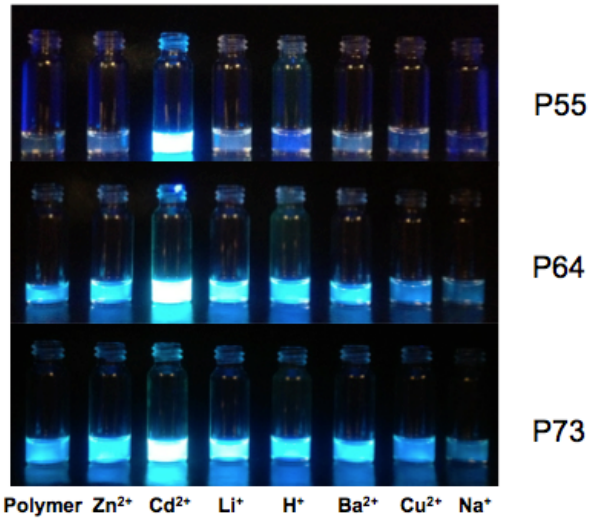

Figure 3-14 Photographic images of THF solutions of P55, P64, and P73 without and with various metal cations and H^+ under the irradiation of a UV lamp.

In addition, the titration of **P64** and **P73** with various metal ions was also conducted and monitored by UV-Vis spectroscopy and fluorescence spectroscopy as shown from Figure 3-15 to Figure 3-26. Since their fluorescence backgroundsare strong (highly emissive) compared with **P55**, they are not suitable for fluorescence turn-on sensing purposes. Hence there is no necessity of making further discussions on the titration results.

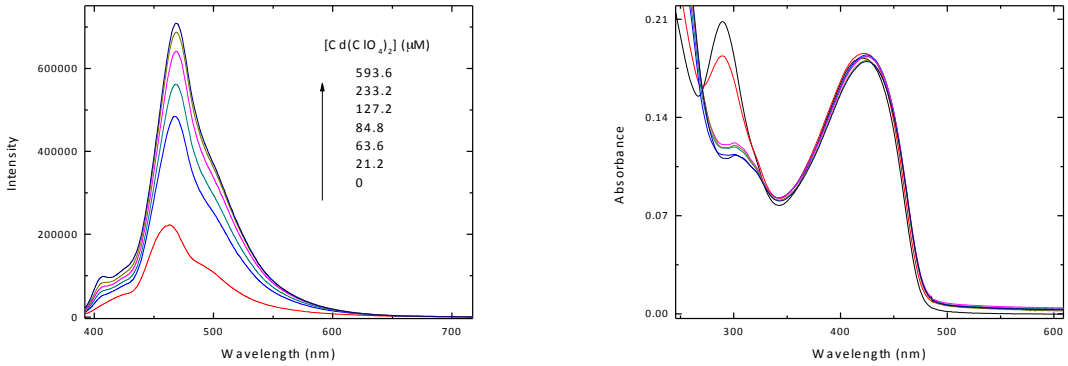

Figure 3-15 Fluorescence spectral (left) and absorption changes (right) of P64 (100 mg mL^{-1}, λ_{ex} = 380 nm) upon titration of $Cd(ClO_4)_2$ in THF.

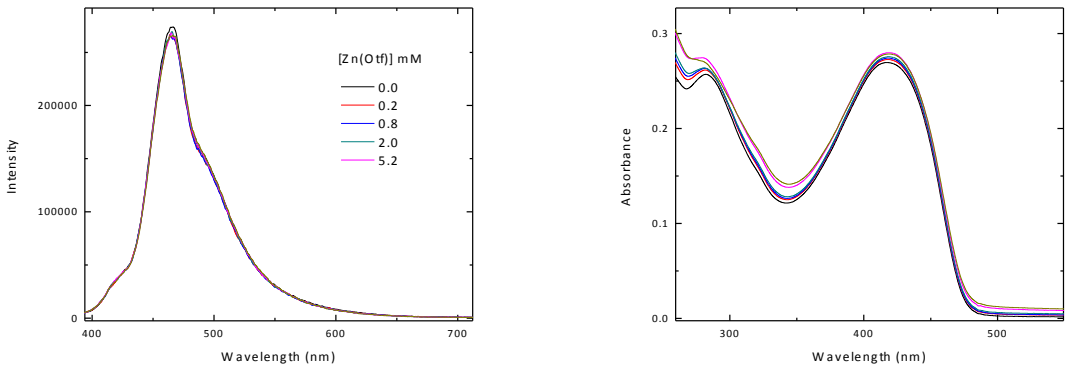

Figure 3-16 Fluorescence spectral (left) and absorption changes (right) of P64 (100 mg mL^{-1}, λ_{ex} = 380 nm) upon titration of $Zn(OTf)_2$ in THF.

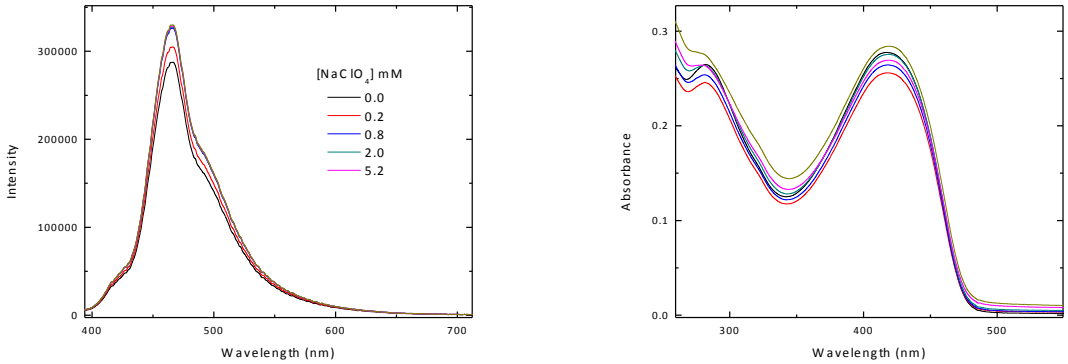

Figure 3-17 Fluorescence spectral (left) and absorption changes (right) of P64 (100 mg mL^{-1}, λ_{ex} = 380 nm) upon titration of $NaClO_4$ in THF.

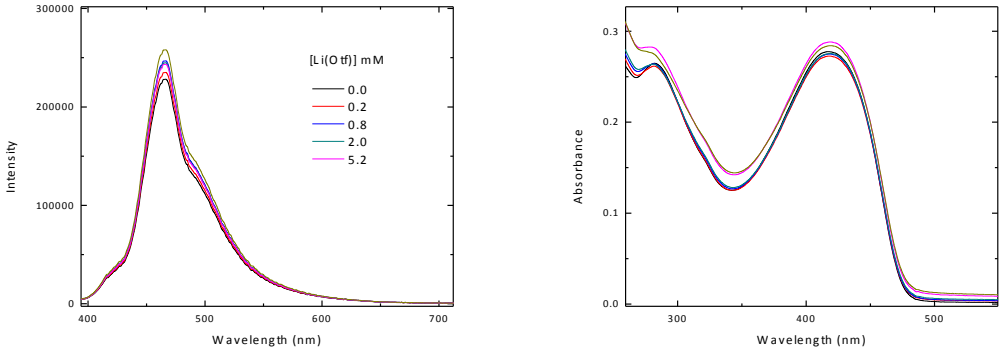

Figure 3-18 Fluorescence spectral (left) and absorption changes (right) of P64 (100 mg mL mL^{-1}, λ_{ex} = 380 nm) upon titration of LiOTf in THF.

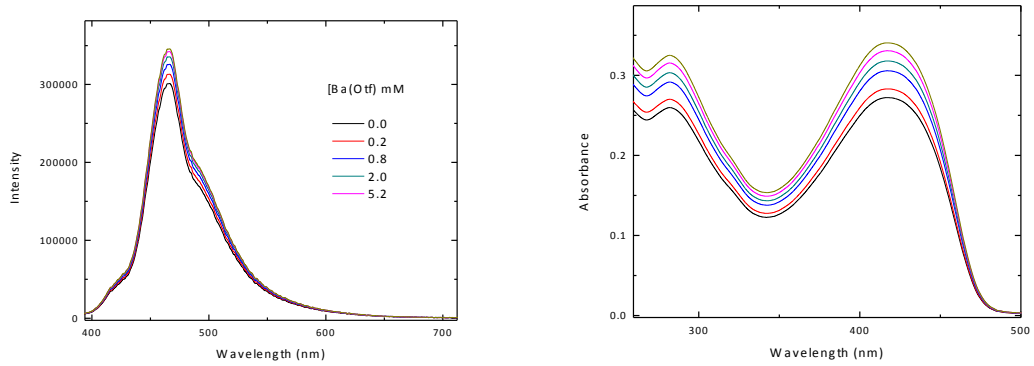

Figure 3-19 Fluorescence spectral (left) and absorption changes (right) of P64 (100 mg mL^{-1}, λ_{ex} = 380 nm) upon titration of Ba(OTf)$_2$ in THF.

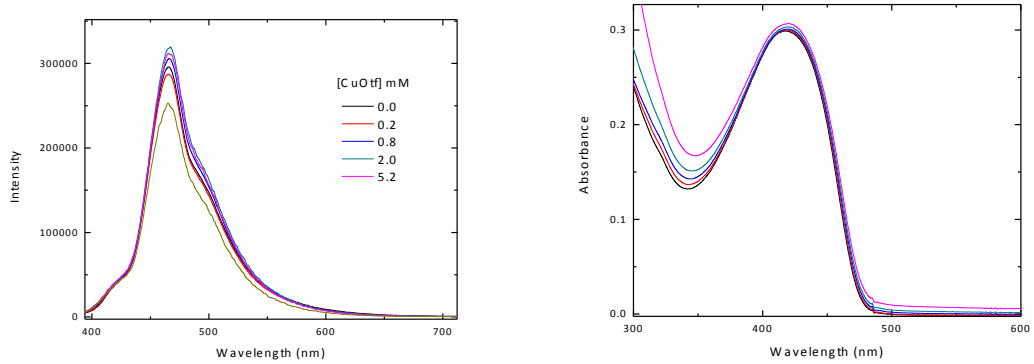

Figure 3-20 Fluorescence spectral (left) and absorption changes (right) of P64 (100 mg mL mL^{-1}, λ_{ex} = 380 nm) upon titration of Cu(OTf)$_2$in THF.

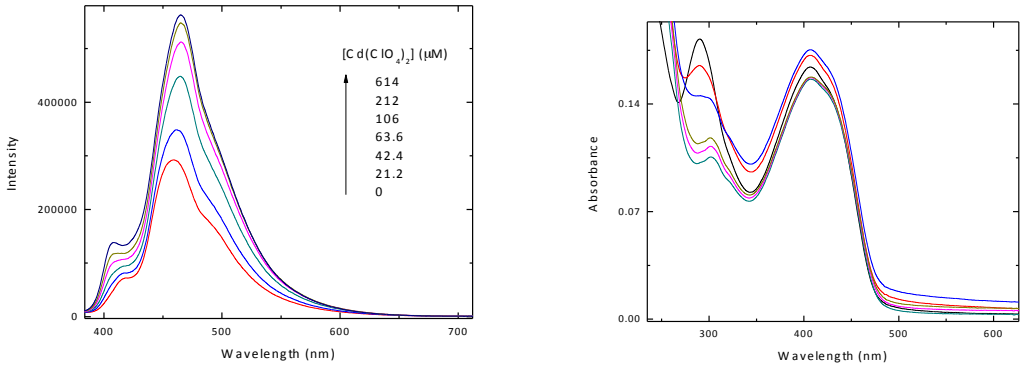

Figure 3-21 Fluorescence spectral (left) and absorption changes (right) of P73 (100 mg mL^{-1}, λ_{ex} = 380 nm) upon titration of $Cd(ClO_4)_2$ in THF.

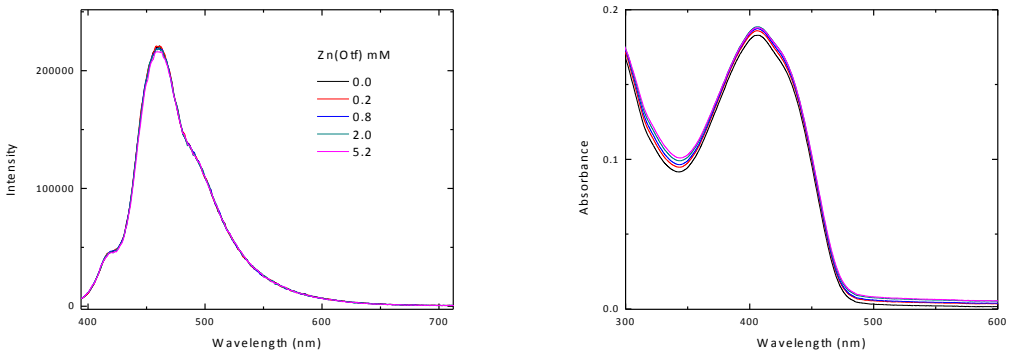

Figure 3-22 Fluorescence spectral (left) and absorption changes (right) of P73 (100 mg mL^{-1}, λ_{ex} = 380 nm) upon titration of $Zn(OTf)_2$ in THF.

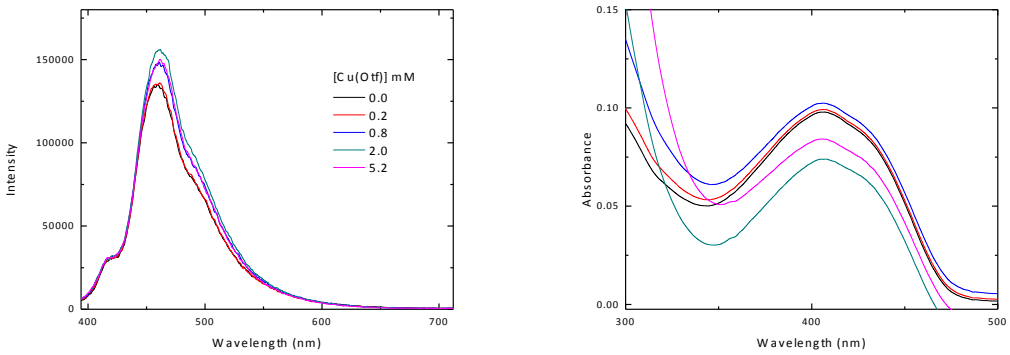

Figure 3-23 Fluorescence spectral (left) and absorption changes (right) of P73 (100 mg mL^{-1}, λ_{ex} = 380 nm) upon titration of $Cu(OTf)_2$ in THF.

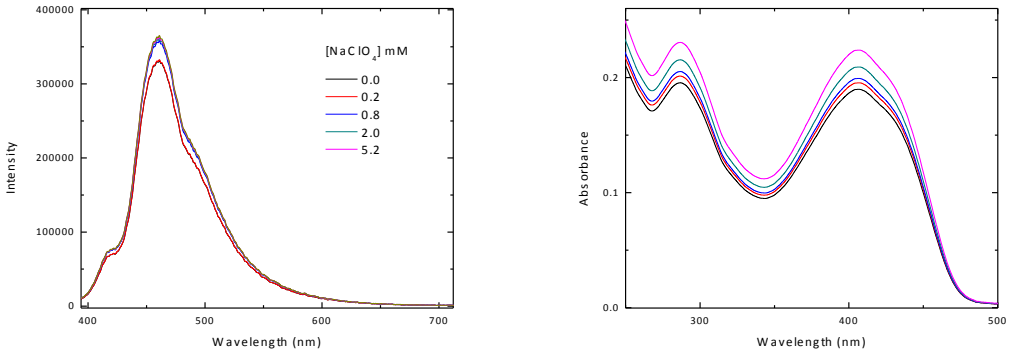

Figure 3-24 Fluorescence spectral (left) and absorption changes (right) of P73 (100 mg mL^{-1}, λ_{ex} = 380 nm) upon titration of $NaClO_4$ in THF.

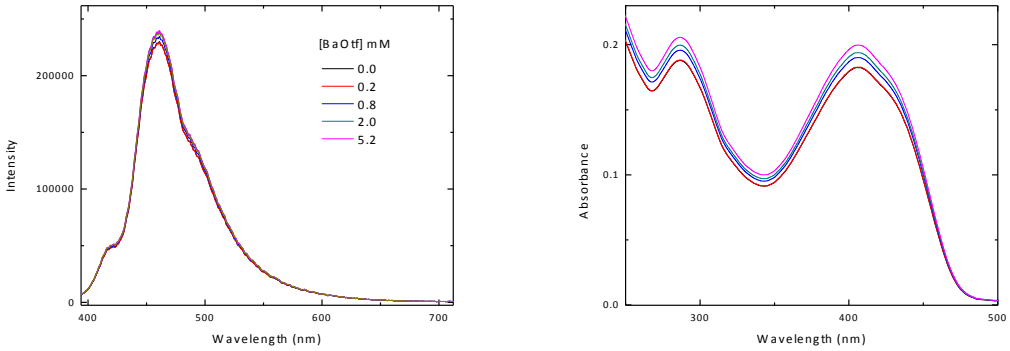

Figure 3-25 Fluorescence spectral (left) and absorption changes (right) of P73 (100 mg mL^{-1}, λ_{ex} = 380 nm) upon titration of Ba(OTf)$_2$ in THF.

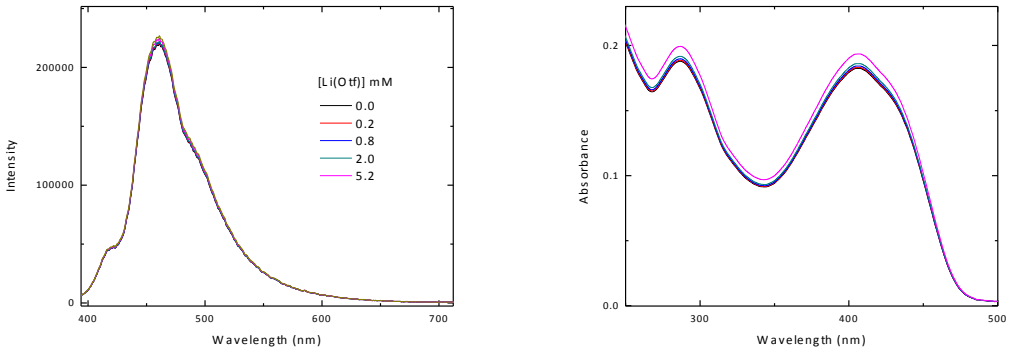

Figure 3-26 Fluorescence spectral (left) and absorption changes (right) of P73 (100 mg mL^{-1}, λ_{ex} = 380 nm) upon titration of LiOTf in THF.

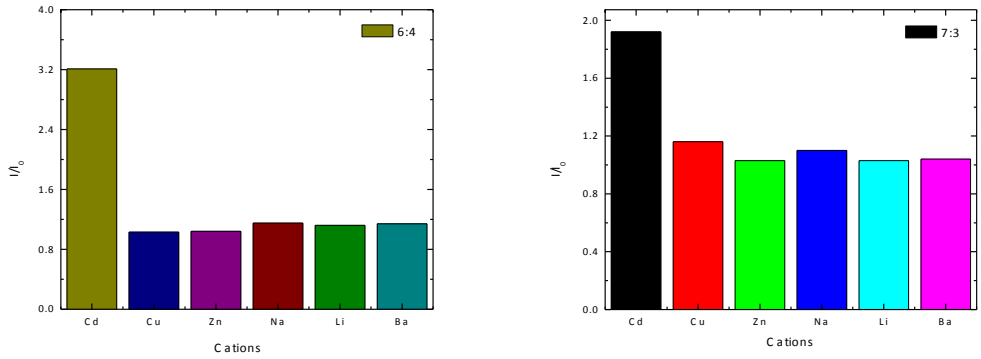

Figure 3-27 Trend of P64 (left) and P73 (right) fluorescence enhancement (I/I_0) for different cations at maximum emission wavelength (I: fluorescence intensity at the saturation point of titration; I_0: initial fluorescence intensity).

3.4 Conclusion and future work

Different lengths of spacing between amino receptors have been successfully introduced into the PPE backbone. As expected, the resulting new polymers exhibited different emission and absorption properties. In particular, **P55** exhibited very dark fluorescence background, and proced to be highly sensitive and selective for only Cd^{2+}. Although the fluorescence enhancement upon interaction with metal ions is decreased, the selectivity has been significantly improved compared with the unmodified polymer. Due to the limited time spent on this side project, two more polymers, **P37** (30% molar equivalent of monomer **3-9** and 70% molar equivalent of **3-14**) and **P46** (40% molar equivalent of monomer **3-9** and 60% molar equivalent of **3-14**), are not yet synthesized, but they should be acquired in the future work to systemically study this polymer system.

3.5 Experimental

Chemicals were purchased from commercial suppliers and used directly without purification. THF was distilled from sodium/benzophenone before use. Et_3N and toluene were distilled from CaH_2 before use. Palladium catalysts, $Pd(PPh_3)_2Cl_2$ and $Pd(PPh_3)_4$, were prepared from $PdCl_2$ according to literature procedures. All reactions were conducted in standard, dry glassware and under an insert atmosphere of nitrogen unless otherwise noted. Evaporation and concentration were carried out with a water-aspirator. Flash column chromatography was performed using 240-400 mesh silica gel purchased from VWR International. Thin-layer chromatography (TLC) was carried out with silica gel 60 F254 covered on plastic sheets and visualized by UV light. 1H and 13C NMR spectra were measured on a Bruker Avance 500 MHz or a 300 MHz spectrometer. Chemical shifts (δ) are reported in parts per million (ppm) downfield from the signal of internal reference $SiMe_4$. Coupling constants (J) are given in Hertz.

4-Iodo-N,N'-dimethylaniline (3-1)

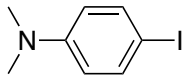

3-1

In a round bottom flask equipped with a stirrer, *N,N'*-dimethylaniline (2 g, 0.0165mol) and pyridine/dioxane (60 mL, 1:1) were mixed and cooled at 0 °C with an ice-water bath. Iodine chips (12.56 g, 0.0495mol) were added and the resulting mixture was stirred for 1 h. Then the ice bath was removed and the reaction mixture was stirred

for another 1 hat room temperature. The resulting mixture was washed with $Na_2S_2O_3$ (aq. 10%) to remove the excess I_2 and brine, followed by drying with $MgSO_4$. After filtration and concentration under vacuum, the mixture (residure) was subjected to column chromatography (CH_2Cl_2/hexanes, 1:4) to afford the desired product **3-1** as a white powder (2.46 g, 0.01mol, 60%). ^{1}H NMR (500 MHz, $CDCl_3$): δ = 7.47 (d, *J* = 9.05 Hz, 2 H), 6.50 (d, *J* = 9.01 Hz, 2H), 2.91 (s, 6H).

***N,N'*-dimethyl-4-((trimethylsily)ethynyl)benzenamine (3-2)**

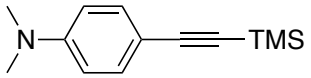

3-2

In a round bottom flask equipped with a stirrer, compound **3-1** (0.3 g, 1.21 mmol), TMSA (0.53 mL, 3.63 mmol), $Pd(PPh_3)_2Cl_2$ (80 mg, 0.121 mmol) and CuI (67 mg, 0.363 mmol) were mixed and dissolved in piperidine (8mL) under N_2. The mixture was stirred at 70 °C for 24 h. After removal of solvent invacuum, the residue was dissolved in diethylether. The solution was then washed with brine and saturated $NaHCO_3$. After concentration under the vacuum, the residue was subjected to column chromatography (CH_2Cl_2/hexanes, 1:4) to afford the desired product **3-2** as pale yellow solid (230 mg, 1.21 mmol, 88%). ^{1}H NMR (500 MHz, $CDCl_3$): δ = 7.35 (d, *J* = 8.99 Hz, 2 H), 6.60 (d, *J* = 8.96 Hz, 2H), 2.96 (s, 6H), 0.23 (s, 9H).

4-Ethynyl-*N*,*N*-dimethylbenzamine (3-3)

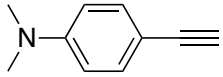

3-3

In a round bottom flask equipped with a stirrer, compound **3-2** (850 mg, 3.91 mmole) and K_2CO_3 (1.62g, 11.72 mmol) were dissolved in MeOH (25 mL). Then the mixture was stirred for 1 hour. After removal of solvent in vacuum, the residue was dissolved in diethylether. The solution was then washed with brine, dried with $MgSO_4$, and then concentrated under vacuum to afford compound **3-3** as a pale yellow solid (518 mg, 3.90 mmol, 91.5%). ^{1}H NMR (500 MHz, $CDCl_3$): δ = 7.38 (d, J = 8.96 Hz, 2H), 6.63 (d, J = 8.94 Hz, 2H), 2.97 (s, 7H).

1,4-Bis(2-bromoethoxy)benzene (3-4)

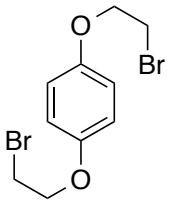

3-4

In a round bottom flask equipped with a stirrer, carbon tetrabromide (33.46 g, 100.9 mmol) was slowly added to a solution of 1,4-bis(2-bromoethoxy)benzene (5 g, 25.22 mmol) and triphenylphosphine (26.1 g, 100.9mmol) in 450 ml of dry acetonitrile with stirring under ice bath. Then the ice bath was removed and the mixture was

allowed to warm to room temperature. The resulting clear solution was then stirred for another 4 h. Upon the addition of 70 mL of cold water, the precipitation formed. Then the product was collect by filtration and washed by with water/methanol (40:60 v/v), followed by recrystalliztion from methanol. The obtained colorless flake-like crystals were dried under vacuum to afford product **3-4** (6.0406 g, 18.63 mmol, 74%). ^{1}H NMR (500 MHz, $CDCl_3$): δ = 6.86 (s, 2 H), 4.25 (t, *J* = 6.30 Hz, 4H), 3.61 (t, *J* = 6.30 Hz, 4H);

2,5-Diiodo-1,4-Bis(2-bromoethoxy)benzene (3-5)

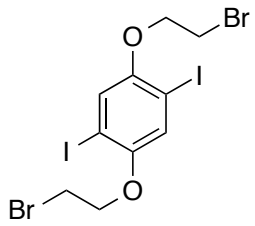

3-5

In a round bottom flask equipped with a stirrer, compound **3-4** (6.0 g, 18.51 mmol), I_2 (14.081 g, 55.52 mmol) and $Hg(OAc)_2$ (17.7 g, 55.52 mmol) were dissolved in CH_2Cl_2 (170 ml) . The mixture was stirred for overnight. Then resulting mixture was subjected to filtration. The filtrate was washed with $Na_2S_2O_3$ and H_2O, dried over $MgSO_4$, and evaporated in vacuum. The residue was recrystallized from EtOH (500 mL) to afford product **3-5** a colorless solid (7.918 g, 13.746 mmol, 79%). ^{1}H NMR (500 MHz, $CDCl_3$): δ = 7.22 (s, 2 H), 4.27 (t, *J* = 6.33 Hz, 4H), 3.66 (t, *J* = 6.29 Hz, 4H).

(2,5-Bis(3-bromopropyl)-1,4-phenylene)bis(ethyne-2,1 diyl)bis(trimethylsilane) (3-6)

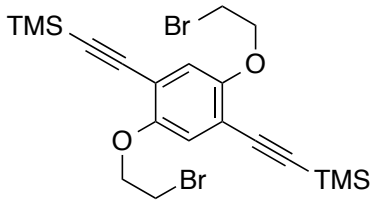

3-6

In a round bottom flask equipped with a stirrer, compound **3-5** (15.1548 g, 0.02631 mol), $Pd(PPh_3)_2Cl_2$ (0.3 g, 0.002631 mol), and CuI (0.3g, 0.007893 mol) were dissolved in 500 ml of dry THF/Et_3N (1:1). Then a solution of TMSA (11.6 ml, 0.07893 mol) in THF (8 ml) was added dropwise. The resulting mixture was stirred at room temperature for 24 hours and then the solvent was removed. The resulting residue was dissolved in CH_2Cl_2 and washed with H_2O. The organic layer was then dried over $MgSO_4$, filtered and finally subjected to column chromatography (hexanes/ethyl acetate 6:1) to afford the compound **3-6** as an off-white solid (10.1564 g, 0.0197 mol, 75%).^{1}H NMR (300 MHz, $CDCl_3$): δ = 6.93 (s, 2 H), 4.28 (t, J = 6.46 Hz, 4H), 3.63 (t, J = 6.49 Hz, 4H), 0.26 (s, 18H).

2,5-Bis(2-azidoethoxy)-1,4-phenylene)bis(ethyne-2,1-diyl)bis(trimethylsilane) (3-7)

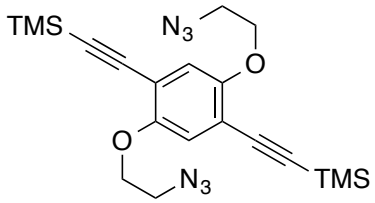

3-7

In a round bottom flask equipped with a stirrer, compound **3-6** (0.6 g, 1.16 mmol) was dissolved in DMF (10 mL), and NaN_3 (0.453 g, 6.97 mmol) was added into the solution. The resulting mixture was stirred at 40 °C for overnight. Cold water (5 mL) and dichloromethane (15 mL) were then added to the reaction mixture. The organic layer was washed with brine and water, and dried over $MgSO_4$. It was then concentrated in vacuum to afford compound **3-7** as colorless needle-like crystals (0.5 mg, 0.963 mmol, 83%). ^{1}H NMR (300 MHz, $CDCl_3$): δ = 6.94 (s, 2 H), 4.14 (t, J = 4.88 Hz, 4H), 3.60 (t, J = 4.88 Hz, 4H), 0.25 (s, 18H).

Compound 3-8

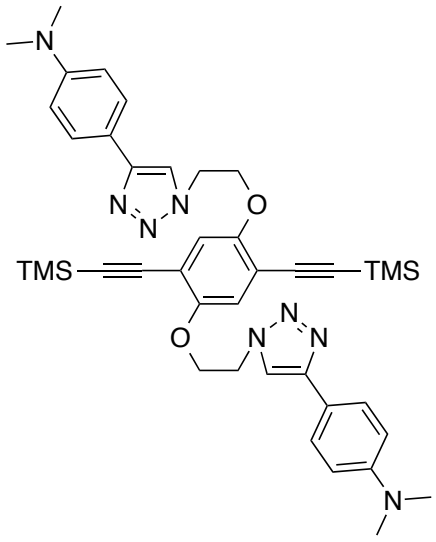

3-8

In a round bottom flask equipped with a stirrer, compound **3-3** (411 mg, 2.84 mmol) and compound **3-7** (500 mg, 1.13 mmol) were dissolved in dry DMF (10 mL). CuI (21.5 mg, 0.113 mmol) and DIPEA (16 mg, 0.113 mmol) were added to the mixture and the resulting mixture was allowed to stir at room temperature for 24 h. The resulting yellow-brown slurry was filtered and the residue was washed with CH_2Cl_2. The filtrate was washed with saturated NH_4Cl, brine, and H_2O. After removal of solvent under the vacuum, the residue was subjected to column chromatography with ethylacetate/hexanes (2:1) gave **3-8** as a pale-yellow solid (243 mg, 0.33 mmol, 30%). ^{1}H NMR 500 MHz, $CDCl_3$): δ = 8.06 (s, 2 H), 7.70 (d, J = 8.89 Hz, 4H), 6.88, (s, 2H), 6.76 (t, J = 8.89 Hz, 4H), 4.81 (t, J = 4.78 Hz, 4H), 4.35 (t, J = 4.88 Hz, 4H), 2.98 (s, 12H), 0.25 (s, 18H).

Compound 3-9

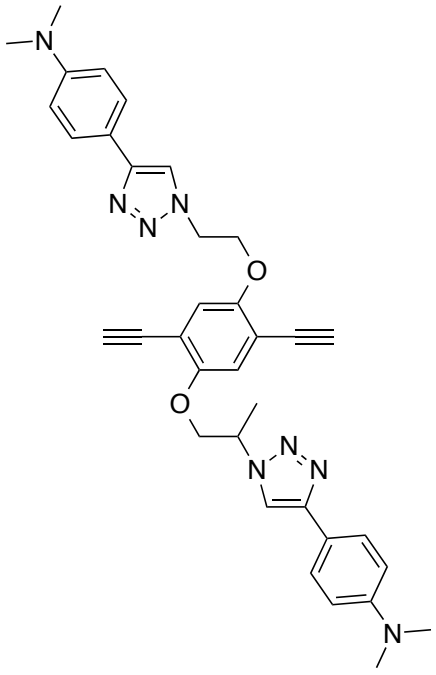

3-9

In a round bottom flask equipped with a stirrer, compound **3-8** (664 mg, 0.908 mmol) and K_2CO_3 (750 mg, 5.45 mmol) were dissolved in 20 mL of THF/MeOH (2:1) in a round-bottom flask and stirred at room temperature for 1 h. After removal of solvent under vacuum, the residue was dissolved in CH_2Cl_2 and washed with water. The organic layer was dried over $MgSO_4$ and the solvent was removed under vacuum to afford compound **3-9** as a pale-yellow solid (375 mg, 0.64 mmol, 77%). ^{1}H NMR (500 MHz, DMSO-d_6): δ = 8.33 (s, 2 H), 7.63 (d, J = 8.72 Hz, 4H), 7.12, (s, 2H), 6.78 (t, J = 8.75 Hz, 4H), 4.75 (t, J = 4.71 Hz, 4H), 4.48 (s, 2H), 4.41 (t, J = 4.73 Hz, 4H), 2.92 (s, 12H).

1,4-Bis(decyloxy)benzene (3-10)

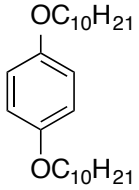

3-10

In a round bottom flask equipped with a stirrer, hydroquinone (6.51 g, 59.2 mmol), KOH (8.27 g, 147.68 mmol) and $C_{10}H_{21}Br$ (32.53 g, 147.68 mmol) were dissolved in EtOH (120 mL). The resulting grey mixture washeated to 90 °C and refluxed for 60 h. The resulting mixture was diluted with CH_2Cl_2, washed with NH_4Cl (aq), H_2O, and dried over $MgSO_4$. It was filtered through a short silica plug and washed with hexane. After removal of solvent under vacuum, the crude product was subjected to recrystallization from MeOH (300 mL). The resulting colorless flakes were washed with MeOH to afford compound **3-10** as colorless flakes (13.61 g, 33.8 mmol, 55%). ^{1}H NMR (500 MHz, $CDCl_3$): δ = 6.80 (s, 4 H), 3.88 (t, *J* = 6.59 Hz, 4H), 1.78-1.68 (m, 4H), 1.44-1.37 (m, 28H), 0.86 (t, *J* = 6.45 Hz, 6H).

1,4-Bis(decyloxy)-2,5diiodobenzene (3-11)

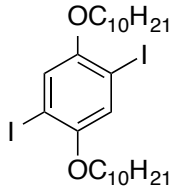

3-11

In a round bottom flask equipped with a stirrer, compound**3-10** (12.57 g, 22.6 mmol), I_2 (24.51 g, 96.6 mmol) and $Hg(OAc)_2$ (30.78 g, 96.6 mmol) were dissolved in CH_2Cl_2 (200 mL). The mixture was stirred at room temperature for 24 h. The resulting mixture was filtered and the filtrate was washed with $Na_2S_2O_3$ (aq), H_2O, brine, and dried over $MgSO_4$. After removal of the solvent under vacuum, and the crude product was recrystallized from EtOH (300mL) to give the colorless flakes compound **3-11**(10.34 g, 11.3 mmol, 50%). ^{1}H NMR (500 MHz, $CDCl_3$): δ 7.17 (s, 2H), 3.92 (t, *J* = 6.44 Hz, 4H), 1.82-1.77 (m, 4H), 1.52-1.46 (m, 4H), 1.36-1.32 (m, 24H), 0.88 (t, *J* = 6.79 Hz, 6H).

1,4-Bis(decyloxy)-2- indo- 5- (trimethylsilylethynyl) benzene (3-12)

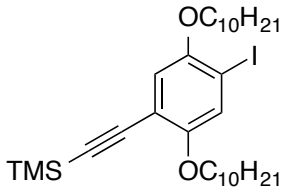

3-12

In a round bottom flask equipped with a stirrer, compound **3-11** (6.35 g, 9.89 mmol), CuI (0.187 g, 0.99 mmol) and $Pd(PPh_3)_2Cl_2$ (0.284 g, 0.41 mmol) were dissolved in Et_3N (60 mL) under N_2. TMSA (1.01mL, 6.9 mmol) was dropwise added and the reaction mixture was stirred at 60 °C for 24 hours. The resulting mixture was filtered and the filtrate was washed with NH_4Cl (aq), H_2O and brine and then dried over $MgSO_4$. After concentration under vacuum, the residue was subjected to column chromatography Hexanes/CH_2Cl_2 (9:1) to give compound **3-12** (2.63 g, 4.2 mmol, 63%)

as colorless liquid. ^{1}H NMR (500 MHz, $CDCl_3$): δ = 7.25 (s, 1 H), 6.83 (s, 1H), 3.95-3.92 (m, 4H), 1.82-1.75 (m, 4H), 1.52-1.46 (m, 4H), 1.34-1.27 (m, 24H), 0.88 (t, J = 6.57, 6H), 0.25 (s, 9H).

(2,5-Bis(decyloxy)-1,4-phenylenebis(ethyne-2,1-diyl)bis(trimethylsilane) (3-13)

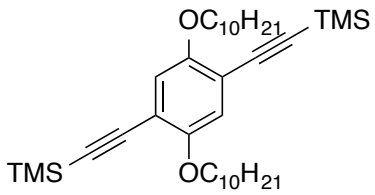

3-13

In a round bottom flask equipped with a stirrer, compound **3-11** (10 g, 15.6 mmol), CuI (0.2 g, 4.68 mmol) and $Pd(PPh_3)_2Cl_2$ (0.25 g, 1.56 mmol) were dissolved in Et_3N/THF(400 mL, 1:1) under N_2. TMSA (6.86mL, 46.7 mmol) was addeddropwiseand the reaction mixture was stirred at room temperature for overnight. After concentration under the vacuum, the residue was subjected to column chromatography ethylacetate/hexanes (1:3) to afford compound **3-13** as a pale-pink solid (5.913 g, 10.1 mmol, 65%). ^{1}H NMR (500 MHz, $CDCl_3$): δ 6.91 (s, 2H), 3.96 (t, *J* = 6.36 Hz, 4H), 1.83-1.78 (m, 4H), 1.55-1.49 (m, 4H), 1.34-1.29 (m, 24H), 0.91 (t, *J* = 6.80, 6H), 0.28 (s, 18H).

1,4-Bis(decyloxy)-2,5-diethylbenzene (3-14)

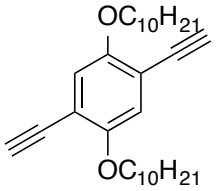

3-14

In a round bottom flask equipped with a stirrer, compound **3-1** (3.8 g, 6.52 mmol) and K_2CO_3 (5 g, 39.15 mmol) were dissolved in 80 mL of THF/MeOH (2:1) in a round-bottom flask and stirred at room temperature for 1 h. After concentration under the vacuum, the residue was dissolved in CH_2Cl_2 and washed with water. The organic layer dried over $MgSO_4$ and the solvent was removed under vacuum to give compound **3-14** as a pale-yellow solid (2.66 g, 6.06 mmol, 93%). ^{1}H NMR (500 MHz, $CDCl_3$): δ 6.95 (s, 2H), 3.97 (t, J = 6.63 Hz, 4H), 3.32 (s, 2H), 1.82-1.77 (m, 4H), 1.52-1.46 (m , 4H), 1.39-1.34 (m, 24H), 0.90-0.87 (t, J = 6.76 Hz , 6H).

Polymer 55 (P55)

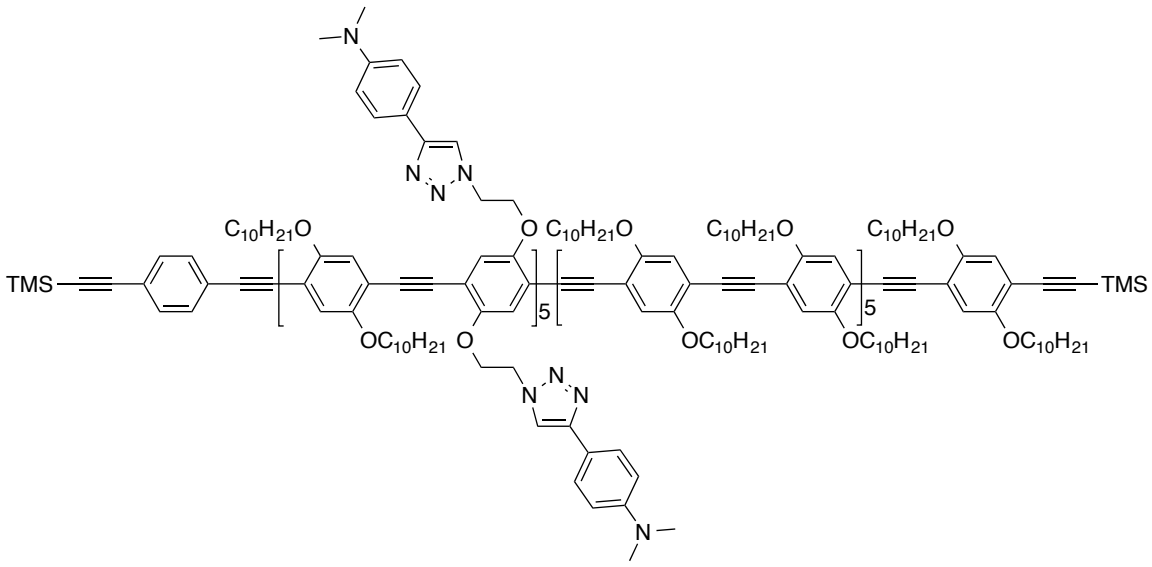

Polymer 5:5

In a round bottom flask equipped with a stir, compound **3-9** (79.4 mg, 0.135 mmol), compound **3-14** (59 mg, 0.135 mmol), compound **3-11** (173.8 mg, 0.36 mmol), compound **3-12** (16.5 mg, 0.036 mmol) as an end-capping reagent, $Pd(PPh_3)_2Cl_2$ (18.9 mg, 0.036 mmol) and CuI (15.4 mg, 0.108 mmol) were dissolved in dry THF/piperidine (50 mL, 5:3).The resulting mixture was degased by freeze-pump-thaw method for three cycles. Then the mixture was heated up to 60 °C stirred for 24 h at this temperature under N_2. After the resulting mixture was cooled to room temperature, the solvent was evaporated off under vacuum and the residue was dissolved in CH_2Cl_2 and washed with NH_4Cl (aq) and H_2O to give a orange-brown organic layer, which was concentrated and dissolved again in CH_2Cl_2. Upon addition of MeOH, a precipitate formed and was collected to give **P55** (164.35 mg, 50%) as a yellow-orange solid.

Polymer 64 (P64)

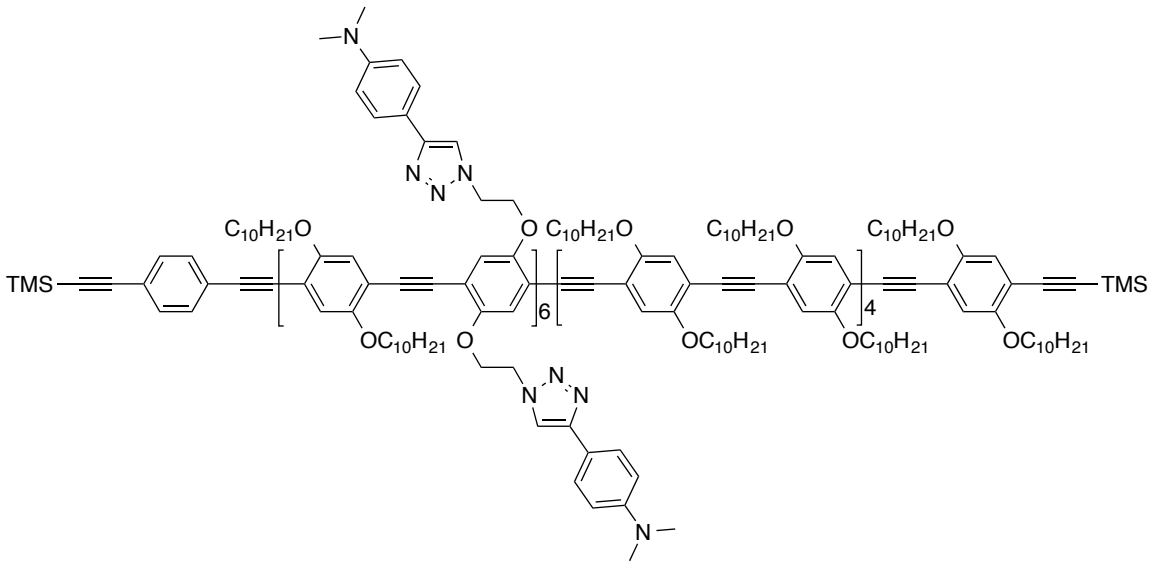

Polymer 6:4

In a round bottom flask equipped with a stirrer, compound **3-9** (80 mg, 0.136 mmol), compound **3-14** (39 mg, 0.09 mmol), compound **3-11** (145 mg, 0.23 mmol), compound **3-12** (13 mg, 0.023 mmol), $Pd(PPh_3)_2Cl_2$ (15 mg, 0.023 mmol) and CuI (13 mg, 0.068 mmol) were dissolved in dry THF/piperidine (50 mL, 5:3). The resulting mixture was degassed by freeze-pump-thaw method for three cycles. Then the mixture was heated to 60 °C and stirred for 24 h at this temperature under N_2. After the resulting mixture was cooled to room temperature, the solvent was evaporated off under vacuum and the residue was dissolved in CH_2Cl_2 and washed with NH_4Cl (aq) and H_2O to afford a orange-brown organic layer, which was concentrated and dissolved again in CH_2Cl_2. Upon the addition of MeOH, a precipitate formed and was collected to give **P64** (140.3 mg, 46%) as a yellow-orange solid.

Polymer 73 (P73)

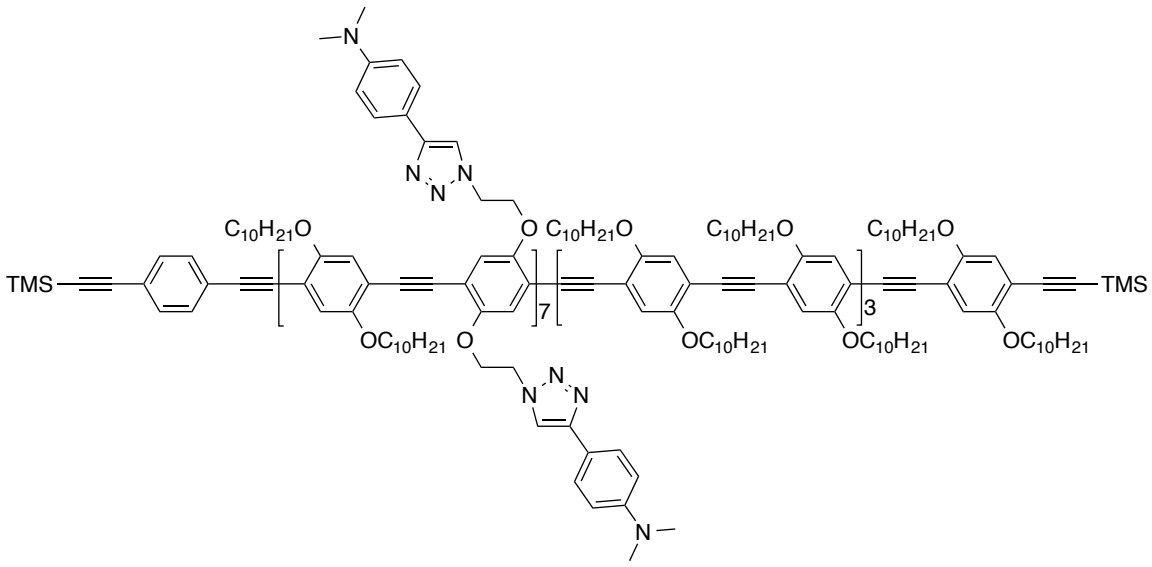

In a round bottom flask equipped with a stirrer, compound **3-9** (80 mg, 0.136 mmol), compound **3-14** (25.6 mg, 0.058 mmol), compound **3-11** (125 mg, 0.194 mmol), compound **3-12** (11.9 mg, 0.019 mmol), $Pd(PPh_3)_2Cl_2$ (13.7 mg, 0.019 mmol) and CuI (11.1 mg, 0.058 mmol) were dissolved in dry THF/piperidine (50 mL, 5:3). The resulting mixture was degassed by freeze-pump-thaw method for three cycles. Then the mixture was heated to 60 °C and stirred under $N_2$for 24 h at this temperature. After the resulting mixture was cooled to room temperature, the solvent was evaporated off under vacuum and the residue was dissolved in CH_2Cl_2 and washed with NH_4Cl (aq) and H_2O. The organic layer was concentrated under vacuum and redissolved in CH_2Cl_2. Upon the addition of MeOH, a precipitate formed and was collected by vacuum filtration to produce **P73** (106.92 mg, 40%) as a yellow-orange solid.

Chapter 4 Numerical Simulation of the Cathodic Protection System with the New Coatings

4.1 Introduction

Corrosion presents a long-lasting and very challenging issue to modern industrial and civilian activities. However, finding efficient ways to prevent it from causing significant damage to infrastructure and even disastrous loss of human life is vitally important, and indeed the costs related to corrosion and corrosion prevention constitute a significant part of the gross national product in the developed world. Over the past few decades, marine and offshore industries have undergone a considerable expansion, driven by the increasing demand for marine transportation and oil and gas exploration. This means increasing human activities will be undertaken in coastal and marine areas that were previously unexplored. How to tackle the emerging technological difficulties encountered within these areas is certainly an important research area requiring cooperative efforts from both academia and industry.

A cathodic protection (CP) system is an effective technique for the preservation of metals against corrosion in an aqueous environment and widely applied to marine and offshore structures(Bortels et al., 2007). Corrosion in marine and offshore structures will occur due to galvanic processes resulting from differences in the electrochemical properties of the materials involved. An electric current is set up and the material which acts as the anode is subject to corrosion. Galvanic protection occurs when different metals are introduced into the structure to setup an electric field which

will reduce and delay the corrosion of the structure. Impressed current protection occurs when an external power supply is introduced so that anodes positioned close to the structure are supplying a known and controllable current into the system. Like the galvanic system this sets up an electrostatic field which prevents the structure from corrosion. Both galvanic and impressed current protection systems involve making the structure behave as a cathode and for this reason the process is known as cathodic protection (Al-Otaibi, 2010) .

The boundary element method is an effective approach to perform optimization. In 2010, Abootalebi and coworkers investigated the application of the boundary elements method to solve cathodic protection problems such as 2D steel storage tanks.(Abootalebi et al., 2010) The basic concept is to set up suitable polarization curves to allow a critical potential to be identified. Optimization of electrode locations is performed by numerical methods to ensure the potential in the corresponding structure is lower than this critical potential. Their studies have proven that the boundary elements method is a powerful approach for analyzing and optimizing the sacrificial anode positions in the CP system.

This chapter mainly focuses on the numerical simulation of the cathodic protection system with the newly developed coatings. A 3D software package (BEASY) was used for design and optimization to evaluate the performance of the new polysiloxane-epoxy coatings. The boundary element method was employed in the simulation.

4.2 Corrosion fundamentals

Corrosion refers to a process that involves deterioration or degradation of metal. The most common example of corrosion is the formation of rust on the steel. Most corrosion phenomena are electrochemical in nature and consist of two complementary processes. One is the oxidation (e.g., dissolution of iron), and is also referred to as the anodic half reaction. The other one is reduction reaction (e.g., reduction of oxygen), and is referred as the cathodic half reaction. The products of the electrochemical reactions can react with each other non-electrochemically to form the rust. For example, the corrosion of iron to form rust proceeds according to the overall reaction:

$$2Fe + 2H_2O + O_2 \rightarrow 2Fe(OH)_2 \quad (14)$$

During the electrochemical corrosion process, several anodic (oxidation) andcathodic (reduction) reactions occur. For example, in an offshore structure, the principle anodic reaction in the corrosion process is:

$$Fe \rightarrow Fe^{2+} + 2e^- \ (anodic) \quad (15)$$

$$2H_2O + O_2 + 4\,e^- \rightarrow 4OH^- \ (cathodic) \quad (16)$$

4.3 Cathodic protection

A cathodic protection (CP) system consists of three parts: the structure to be protected (cathode), the anode which provides the protection, and the electrolyte (e.g. sea water). Generally, there are two types of cathodic protection currently used by

corrosion engineers. The first type is known as the sacrificial anode system, and the second type is the impressed current system. (Zamani, 1988)

4.3.1 Sacrificial Anode System

Cathodic protection can prevent corrosion taking place on the surface of a metal by making it cathodic and sacrificial anodes must be incorporated. Generally, sacrificial anodes are electrically connected to the metals which are to be protected, and the materials of the sacrificial anodes must be active metals compare to those to be protected in the galvanic series. Active metals are easily oxidized. The potential difference between sacrificial anodes and protected metals makes the protected metals cathodicduring corrosion and thus remain inert while sacrificial anodes are corroded and consumed. The position and current of sacrificial anodes are of great importance to the performance of the CP system.

Zinc is the most commonly used sacrificial anode material in the marine environment, while aluminum and magnesium are also options. Zinc can also be directly coated on the surface of metals. For example, in zinc-coated steel, so-called galvanized steel, the zinc surface is oxidized into zinc oxide to form a corrosion barrier. Such a barrier protects zinc as well as steel beneath from further corrosion. Zinc corrodes 10 to 100 times slower than steel in most natural environments.(Hermelin et al., 2008) In the environment, if the chloride concentration is high, the zinc oxide film can be destroyed at an accelerated rate.(“Quantification of the oxidizing capacity of

nanoparticulate zero-valent iron.," 2005) If this happens, the adjacent sites become active and act as anodes to protect steel from corrosion. (Figure 4-1)

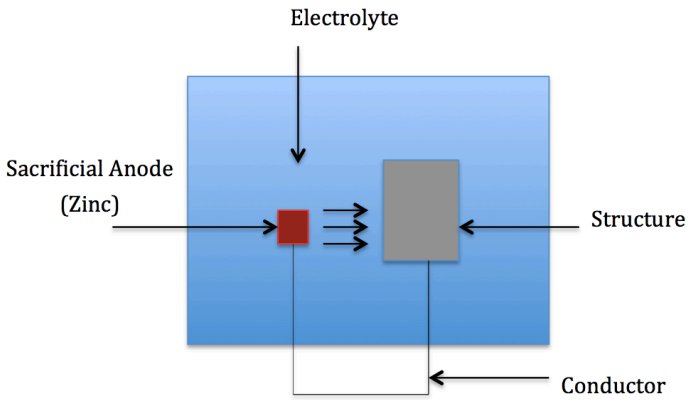

Figure 4-1 A sacrificial anode system

4.3.2 Impressed current system

In addition to the above methods, impressed current cathodic protection (ICCP) is also widely used. The ICCP method is achieved by applying an additional electric current into a metal cathode using an external source of DC power. As the current is applied, the potential of the metal is negatively shifted, which makes the metal cathodic and thus protected. (Figure 4-2)

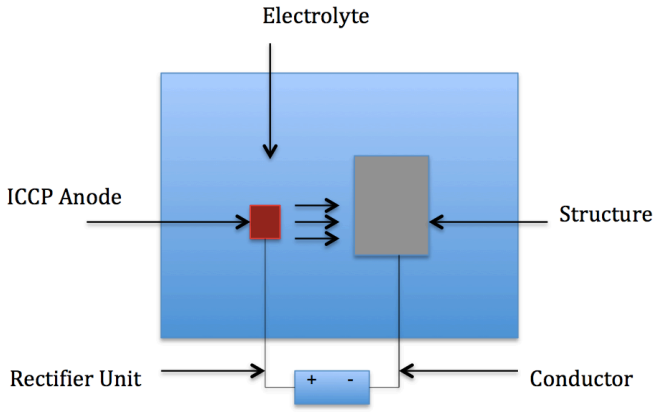

Figure 4-2 An impressed current system

4.4 Mathematical background

In order to predict the potential and current density distribution, a mathematical model has to be set up. The distribution of potential and current is governed by four factors(Chuang, 1986):

1. The electro-neutrality condition (or conservation of charge).
2. The iron conduction characteristics of electrolyte.
3. The polarization characteristics at the metal/electrolyte interface.
4. The geometrical configuration of the domain.

For a uniform, isotropic medium, the flow of current satisfies the Laplace equation, which imposes electro-neutrality in the bulk of the electrolyte:

$$\nabla^2 u = 0 \qquad \text{in a 3-D domain } W \tag{17}$$

Where u is the electrical potential. The current density vector $\vec{j}$ is proportional to the gradient of potential and can be expressed as:

$$\vec{j} = -k\nabla u \tag{18}$$

Where k is the electrolyte conductivity. This boundary-value problem can be solved by using the boundary element method.

In this corrosion study of a sacrificial anode system, the computational domain W is surrounded by outer boundary S_I far from the hull (cathode) and small zinc block (anode). The inner boundaries are denoted by S_C for the hull and S_A for the zinc block. The normal vector $\vec{n}$ on boundaries is assumed to be inward (Figure 4-3).

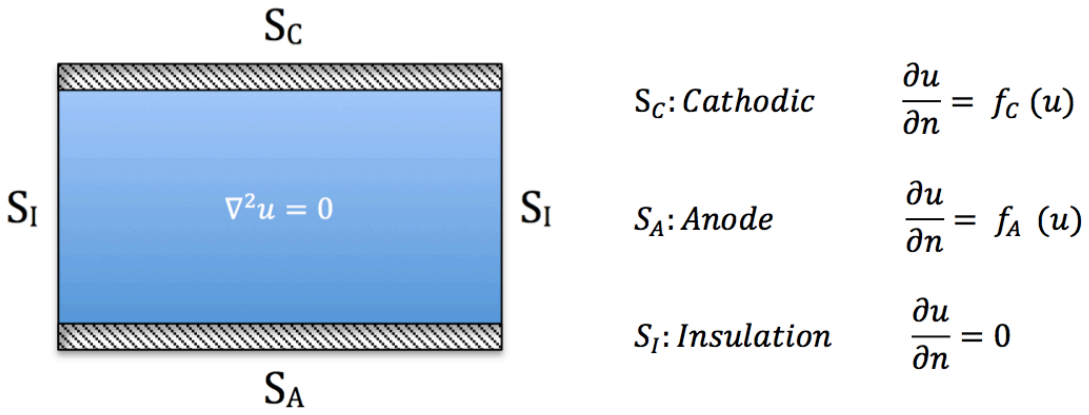

Figure 4-3 Boundary conditions for corrosion problem

The outer boundary S_I is an insulation surface, which is subject to the condition of no current passing through.

$$\frac{\partial u}{\partial n} = 0 \tag{19}$$

For the boundary condition of inner surfaces, polarization functions should be employed. The relationship between potential and current density represents the polarization behavior of the material in the medium. For example, the simplest relationship is a linear relationship and can be written as follows:

$$\frac{\partial u}{\partial n} = c(u - u_0) \tag{20}$$

Where c is the transfer coefficient and u_0 is the potential on the metal (see Figure 3.5). However, the above relationship is still complex because polarization functions depend not only on the material but also on coating, medium, scale, age and temperature. Normally, the polarization functions on these inner surfaces are defined as $f_A(u)$ and $f_C(u)$ which can be obtained from experiments or a polarization database. Then the boundary condition on the anode surface S_A can be expressed as:

$$\frac{\partial u}{\partial n} = f_A(u) \tag{21}$$

The boundary condition on the cathode surface S_C can be expressed as:

$$\frac{\partial u}{\partial n} = f_C(u) \tag{22}$$

The boundary value problem defined above is solved by using Green's theorem to derive integral equations for the electrical potential *u*. The body surface boundaries can be discretized as n_{total} flat panels for numerical calculations. It is assumed that $n_{total} = n_I + n_A + n_C$, where n_I is the panel number on the surface S_I, n_A are the panels on surface S_A and n_C are the panels on surface S_C. The subscript symbol *i* is denoted as the *i*-th field point and *j* is denoted as the *j*-th integrated point. Based on this discretization, the continuous equations can be reduced to a set of linear simultaneous equations for the values of the electrical potential over the panels.

$$4\pi u_i = \sum_j^{n_I} [u_j \frac{\partial}{\partial n_j}(\frac{1}{r_{ij}})]\Delta S_j + \sum_j^{n_A} [u_j \frac{\partial}{\partial n_j}(\frac{1}{r_{ij}}) - f_A(u_j)\frac{1}{r_{ij}}]\Delta S_j + \sum_j^{n_C} [u_j \frac{\partial}{\partial n_j}(\frac{1}{r_{ij}}) - f_C(u_j)\frac{1}{r_{ij}}]\Delta S_j \quad (23)$$

When *i= j* (r_{ij} *= 0)*, the singularity problem should be considered and the equation can be represented:

$$\int \frac{\partial}{\partial n_j}(\frac{1}{r_{ij}})\, ds \quad (24)$$

$$\frac{\partial u}{\partial n} = \frac{\partial}{\partial n}\int \frac{\partial}{\partial n}\left(\frac{1}{r}\right) ds = 2\pi \frac{\partial}{\partial n_j} \quad (25)$$

Where *i=1,2...* n_{total}; r_{ij} is the distance between the *i*-th field point and the *j*-th integrated point; ΔS_j is the area of the *j*-th panel. The details to remove singularity about r_{ij} =0 case can be seen in equation (25). After u_i (*i*=1, 2, … n_{total}) on the

boundaries have been solved, the potential at any field point can be computed from equation (23) directly. The current density at any field point can be computed as the gradient of the known potential based on equation (18).

Finally, a cathodic protection (CP) system can be modeled which consists solving equations (17) to (25).

4.5 Computer modeling

4.5.1 Computer modeling Procedure

Computer modeling procedure is described in Appendix.

4.5.2 Defining the geometry

The model has been represented by a cylinder (cathodic part) and a small anode putting on the surface of the cylinder immerged in the electrolyte (sea water). The geometry of the model was built in the GID software, which is a drawing tool that works as an interface between the model and the BEASY solver software.

The extent of the electrolyte surrounding the anode and cathode can be then defined. Assuming the anode and cathode are fully immersed in deep seawater, a large "box" can be created which will contain the electrolyte surrounding the anodes and cathode. On the surfaces of the box, it is assumed that the normal current density is zero. This is correct if the dimensions of the box are sufficiently large compared with the typical dimensions of the model (Figure 4-4).

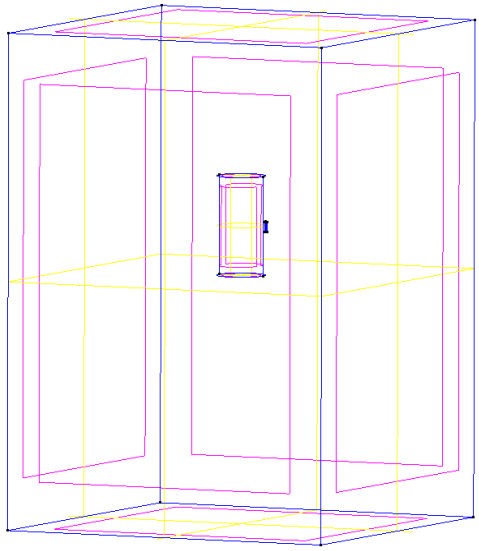

Figure 4-4 Geometry of the cathodic cylinder protected by a small anode

4.5.3 Mesh generation

The mesh generation involves:

- Definition of mesh type for individual geometry.
- Definition of number of elements along the boundary.
- Generation of the mesh.

The generated mesh is shown inFigure 4-5, and the .dat file can be generated.

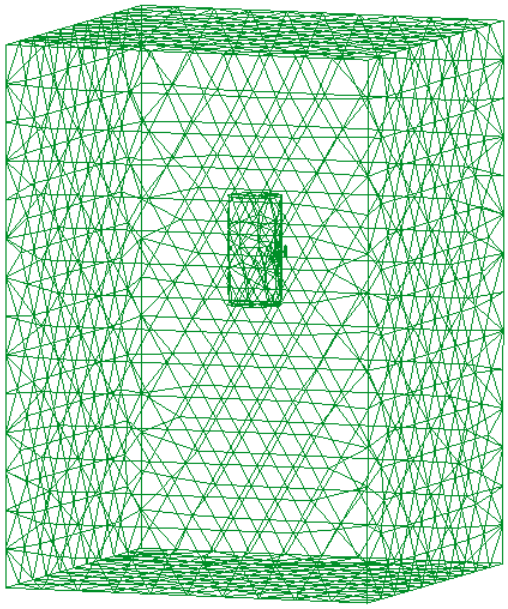

Figure 4-5 Meshof the cathodic cylinder protected by a small anode model

4.6 Polarization curve

The CP system can be simulated by solving the Laplace equation with boundary conditions with a given polarization.

The objectives of this chapter is to compare the performance of the four types of surfaces without coating, with regular epoxy coating (ER), epoxy coating with eugenol-modified polysiloxane (P1) andepoxy coatingwith eugenol-ethoxylvinylsilane-modified polysiloxane (P2). Their material properties can be represented by the polarization curves.

4.6.1 Polarization curve

The polarization behavior of any materials in the medium can be represented by the relationship between current density and potential. The polarization curve can be described by the relationship between the current density (***j***) and the potential ($\Delta\mathbf{V}$). If this relation is linear,***j*** can be expressed as:

$$j = c\,(V - V_0) \tag{26}$$

Where c is the transfer coefficient and V_0 is the potential on the metal.

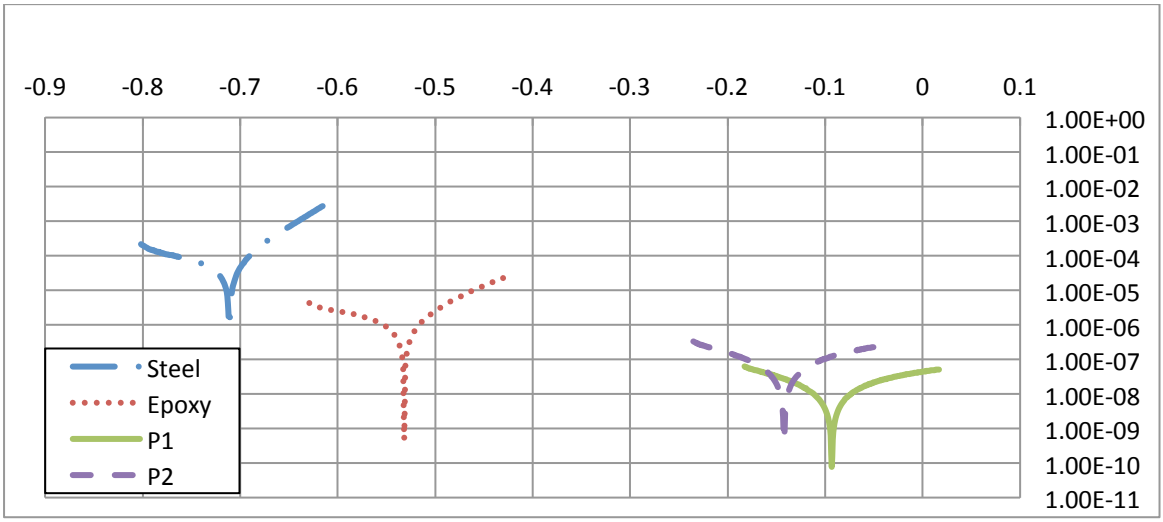

Figure 4-6 Comparison of the polarization curve.

(P1: Epoxy with eugenol-modified polysiloxane coating; P2: Epoxy with eugenol-ethoxylvinylsilane-modified polysiloxane coating. the horizontal axis represents the open-circuit potential value (V) and the vertical axis reprsents the current value (I))

As shown in Figure 4-6, the steel plate coated with modified epoxy coatings P1/P2 shows a large positive shift in the open-circuit potential (OCP), OCP values are as followed: bare steel (-0.71 V), the steel plate coated with epoxy (-0.54 V), the high OCPs of plates coated with P1 (-0.09 V) or P2 (-0.14 V). It indicates that, thermodynamically, they have less tendency to undergo corrosion. Further analysis of the polarization curves provides information about corrosion rate and polarization resistance (Table 4-1). The clear plate coated with P1/P2 corrodes slower than the plate coated with epoxy, and even much slower than bare steel.

4.6.2 Polarization curve data analysis

Table 4-1 Corrosion rate and polarization resistance data.

	Steel	ER	P1	P2
Polarization Resistance (Ω)	308.33Ω	17.77kΩ	1.097MΩ	2.60MΩ
Corrosion Rate (mm/year)	0.7927	0.01854	0.00048	0.00038

(ER: Epoxy coating, P1: Epoxy with eugenol-modified polysiloxane coating, P2: Epoxy with eugenol-ethoxylvinylsilane-modified polysiloxane coating)

4.6.2.1 Corrosion rate

The corrosion rate can be described by thekinetics relationship between the anodic (oxidation) and cathodic (reduction) reactions. Based on Faraday's law, there is

a linear relationship between the metal corrosion rate, R_M, and the corrosion currenti_{corr}:

$$R_M = \frac{M}{nF\rho} i_{corr} \tag{27}$$

Where M is the molar mass of the substance, n is the number of moles of substance, F is Faraday constant, and ρ is the density of the substance.

The determination of corrosion currents is required when one wants to calculate the corrosion rates. The relationship between potential and current density of cathodic and anodic electrode reactions under charge transfer control is given by the Butler-Volmer equation:

$$i = i_{corr}(e^{2.303\frac{\eta}{b_a}} - e^{2.303\frac{\eta}{b_c}}) \tag{28}$$

$$\eta = E - E_{corr} \tag{29}$$

where E is the applied potential and $i$is the measured current density. The over potential, η, is defined as the difference between applied potential and the corrosion potential E_{corr}. The potential, E_{corr}, is the open circuit potential of a metal being corroded. The corrosion current, i_{corr}, and the Tafel constants,b_a, and b_c, can be obtained from the measurement (impedance spectroscopy experiment) in chapter 2.

4.6.2.2 Polarization resistance

The lntercept and the Tafel slopescan be used to estimate the value of the polarization resistance according to:

$$R_p = \frac{1}{2.303(\frac{1}{b_a}+\frac{1}{b_c})} i_{corr} \quad (30)$$

Where R_p is the polarization resistance, i_{corr} is the corrosion current and b_a, and b_c are the Tafel constants.

4.6.2.3 Open circuit potential (OCP)

Table 4-2OCP data

	Steel	ER	P1	P2
Open circuit potential (OCP) (V)	-0.71	-0.54	-0.09	-0.14

(ER: Epoxy coating, P1: Epoxy with eugenol-modified polysiloxane coating, P2: Epoxy with eugenol-ethoxylvinylsilane-modified polysiloxane coating)

The OCP is the potential of the working electrode relative to the reference electrode when no potential or current is being applied to the cell.

The OCP value can evaluate the corrosion condition of the metal. According to the data comparison table (Table 4-2), the OCP value of the epoxy with polymers

coatings shifted towards positive direction, which means the Epoxy with polymers coatings (OCP around -0.1) has better anti-corrosion effect than the Epoxy coating.

4.7 Results and conclusion

The basic idea to deal with coatings is that paint in some thickness can be simulated by scaling the current values in the polarization curves for a particular material.(DeGiorgi, 1998) The coating breakdown factor (*bf*) describes the anticipated reduction in cathodic current density due to the application of an electrically insulating coating. When $bf = 0$, the coating is 100% electrically insulating, therefore decreasing the cathodic current density to zero. A coating with $bf = 1$ has no current-reducing properties.

In Figure 4-7 The distribution of the average protection potential shows the distribution of the average protection potential of four different types of material properties, set up so that the average protection potential is based on the same scale (-610.31mV to -1162.4mV). Based on the above data, one can confidently conclude that the polymer P1/P2 significantly enhances the anti-corrosion performance of epoxy coatings.

Which comparing the uncoated structure (a) to the coated structures (b) (c) (d), the uncoated structure shows much lower anti-corrosion proection than the coated structures. Most of uncoated structures cannot be protected by the sacrificial metal, the average protected potential is around -600mV (Figure 4-7(a)). Most of the coated structures (Figure 4-7(b), (c) and (d)) can be protected and the average protected

potential being around -1000mV. Most notably, structures (c) and (d) shows perfect anti-corrosion phenomena from the plots. Comparing the coated structure (b) with the other two coated structures (c) and (d), structure (b) has higher potential than structure (c) and structure (d). Higher potential means lower current flow; structures with lower current flow are more easily to be corroded. On the contrary, the structures (c) and (d) can be well protected by the coating and CP system.

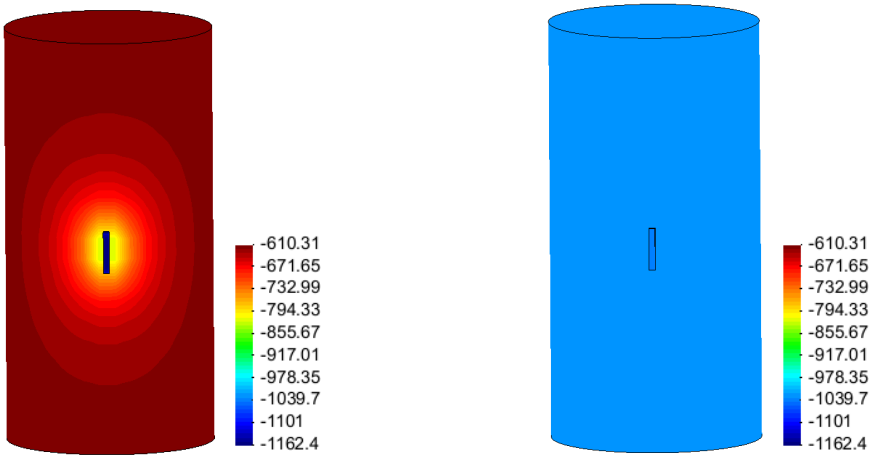

(a) **(b)**

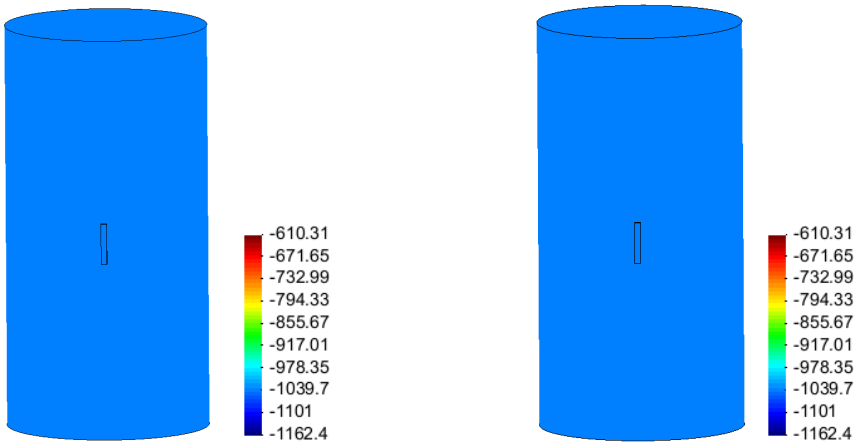

(c) **(d)**

Figure 4-7 The distribution of the average protection potential

(a: steel, b: epoxy coating, c: epoxy with eugenol-modified polysiloxane coating, d: epoxy with eugenol-ethoxylvinylsilane-modified polysiloxane coating)

In conclusion, it can conclude that both numerical simulation and experimental tests show that the polymer P1/P2 can significantly enhance the anti-corrosion performance of epoxy coatings.

Chapter 5 Conclusions and future work

5.1 Conclusion

In this thesis work, the first part focuses on the development of effective anticorrosion coating systems using polysiloxane based polymers as additives for epoxy polyamide coatings. The second part, a 3D software package (BEASY),was used to evaluate the performance of the newly designed polysiloxane-epoxy coatings in cathodic protection systems. The boundary element method is employed to solve the governing mathematical equations.

The cured epoxy coatings doped with the modified polysiloxanes have many great enhancements. The first is a noticeable increase in thermal stability. In addition, the surface of modified epoxy coatings shows interesting spherical dimple-like microscopic patterns. Moreover, the hydrophobicity of the coatings was increased significantly, as evidenced by the increased water contact angles. The performances of commercial epoxy resin coatings in terms of corrosion protection were greatly enhanced after blending with a low percentage of modified polysiloxane additives. The detailed correction mechanisms have been studied by EIS analysis. Based on the experimental results, it is believed that the modified polysiloxane will be of great value for anticossorion applications. Based on the above data, one can confidently conclude that the polymer P1/P2 can significantly enhance the anti-corrosion performance of epoxy coatings.

The numerical simulations are implemented by the BEASY softwareto evaluate the performance of the newly developed polysiloxane-epoxy coatings in cathodic protection systems.The potential theory is used to solve the Laplace equation with boundary conditions specified as polarization functions. The steel plate coated with modified epoxy coatings P1/P2 shows a large positive shift in the open-circuit potential (OCP), which indicates they have lower tendencies to undergo corrosion. Further analyses of the polarization curves provide information about corrosion rate and polarization resistance. It is clear that plate coated with P1/P2 corrodes slower than the plate coated with epoxy, and even much slower than bare steel. Moreover, the distribution of the average protection potential clearly shows the great anti-corrosion performance of the epoxy with P1/P2 coatings.

5.2 Future work

Since the eugenol-functionalized polysiloxanes are very cheap (P1: $55/Kg, P2: $42/Kg.) and easy to produce in large quantity (added P1/P2 (1.0-2.5wt%) into the commercial epoxy coating formulas). It is envisioned that further investigations of this type of polysiloxane materials should lead to useful technology for corrosion control and optimization. Furthermore, another great enhancement of eugenol-functionalized polysiloxanes is the increased hydrophobicity, which can apply to industry using anti-icing and anti-fouling applications. Moreover, the most important enhancement of eugenol-functionalized polysiloxanes is the improvement of corrosion protection effect which can apply to the marine and offshore structures.

For the future work, thenewly developed coating will be applied to other geometries like a ship hull for practical applications. The time-varying boundary conditions may be considered in numerical simulations for the corrosion protections since real polarization functions are time-varying. In addition, the UV resistance of the two polymers will be investigated.

Reference

Abootalebi, O., Kermanpur, A., Shishesaz, M.R., Golozar, M.A., 2010. Optimizing the electrode position in sacrificial anode cathodic protection systems using boundary element method. Corrosion Science 52, 678–687.

Ahmad, S., Gupta, A.P., Sharmin, E., Alam, M., 2005. Synthesis, characterization and development of high performance siloxane-modified epoxy paints.Progress in Organic Coatings 54, 248–255.

Al-Otaibi, M., 2010. The Application of Beasy Software to Simulate Cathodic Protection of Pipelines and Storage Tanks.Master's thesis, Univerisity of British Columbia, Vancouver, Canada.

Almeida, E., Santos, D., Fragata, F., La Fuente, De, D., Morcillo, M., 2006. Anticorrosive painting for a wide spectrum of marine atmospheres: Environmental-friendly versus traditional paint systems. Progress in Organic Coatings 57, 11–22.

Armelin, E., Martí, M., Liesa, F., Iribarren, J.I., Alemán, C., 2010. Partial replacement of metallic zinc dust in heavy duty protective coatings by conducting polymer. Progress in Organic Coatings 69, 26–30.

Armelin, E., Ocampo, C., Liesa, F., Iribarren, J.I., 2007a. Study of epoxy and alkyd coatings modified with emeraldine base form of polyaniline.Progress in Organic Coatings 58, 316–322.

Armelin, E., Oliver, R., Liesa, F., Iribarren, J.I., 2007b. Marine paint fomulations: Conducting polymers as anticorrosive additives.Progress in Organic Coatings 59, 46–52.

Banerjee, I., Pangule, R.C., Kane, R.S., 2010. Antifouling Coatings: Recent Developments in the Design of Surfaces That Prevent Fouling by Proteins, Bacteria, and Marine Organisms. Advanced Materials 23, 690–718.

Barsoukov, E., Macdonald, J.R. (Eds.), 2005. Impedance Spectroscopy. John Wiley & Sons, Inc., Hoboken, NJ, USA.

Bortels, L., Van den Bossche, B., Purcar, M., Dorochenko, A., Deconinck, J., 2007. 3D cathodic protection design of ship hulls. Simulation of Electrochemical Processes II 1, 103–112.

Cabanelas, J., 2003. Water absorption in polyaminosiloxane-epoxy thermosetting polymers. Journal of Materials Processing Technology 143-144, 311–315.

Cabanelas, J.C., Serrano, B., González-Benito, J., Bravo, J., Baselga, J., 2001. Morphology of Epoxy/Polyorganosiloxane Reactive Blends. Macromolecular Rapid Communications 22, 694–699.

Chen, J.-T., Hsu, C.-S., 2011. Conjugated polymer nanostructures for organic solar cell applications. Polymer Chemistry 2, 2707–2722.

Chuang, J.M., 1986. Numerical Solution of Nonlinear Boundary-Value Problems Arising in Corrosion and Electroplating Modeling With Application to 3-D Ships andMarine Structures. PhD's thesis, Technical University of Nova Scotia. Halifax, Canada.

de Silva, A.P., Gunaratne, H.Q.N., Gunnlaugsson, T., Huxley, A.J.M., McCoy, C.P., Rademacher, J.T., Rice, T.E., 1997. Signaling Recognition Events with Fluorescent Sensors and Switches. Chemical Reviews 97, 1515–1566.

DeGiorgi, V.G., 1998. Finite resistivity and shipboard corrosion prevention system performance. Boundary elements XX.20, 555-563

Emge, A., Bäuerle, P., 1999. Molecular recognition properties of nucleobase-functionalized polythiophenes.Synthetic metals 102, 1370–1373.

Fan, L.-J., Zhang, Y., Jones, W.E., 2005. Design and Synthesis of Fluorescence "Turn-on" Chemosensors Based on Photoinduced Electron Transfer in Conjugated Polymers. Macromolecules 38, 2844–2849.

Fan, L.-J., Zhang, Y., Murphy, C.B., Angell, S.E., Parker, M.F.L., Flynn, B.R., Jones, W.E., Jr., 2009. Fluorescent conjugated polymer molecular wire chemosensors for transition metal ion recognition and signaling. Coordination Chemistry Reviews 253, 410–422.

Hermelin, E., Petitjean, J., Lacroix, J.-C., Chane-Ching, K.I., Tanguy, J., Lacaze, P.-C., 2008. Ultrafast Electrosynthesis of High Hydrophobic Polypyrrole Coatings on a Zinc Electrode: Applications to the Protection against Corrosion. Chemistry of Materials 20, 4447–4456.

Hinderliter, B.R., Croll, S.G., Tallman, D.E., Su, Q., Bierwagen, G.P., 2006. Interpretation of EIS data from accelerated exposure of coated metals based on modeling of coating physical properties. Electrochimica Acta 51, 4505–4515.

Ji, W.G., Hu, J.M., Zhang, J.Q., Cao, C.N., 2006. Reducing the water absorption in epoxy coatings by silane monomer incorporation. Corrosion Science 48, 3731–3739.

Kasemura, T., Takahashi, S., Nishihara, K., Komatu, C., 1993. Surface modification of epoxy resin with telechelic silicone. Polymer 34, 3416–3420.

Kendig, M., Scully, J., 1990. Basic aspects of electrochemical impedance application for the life prediction of organic coatings on metals. Corrosion Science 46, 22–29.

Levita, G., De Petris, S., Marchetti, A., Lazzeri, A., 1991. Crosslink density and fracture toughness of epoxy resins. Journal of Materials Science 26, 2348–2352.

Li, J., Kendig, C.E., Nesterov, E.E., 2007. Chemosensory Performance of Molecularly Imprinted Fluorescent Conjugated Polymer Materials. Journal of the American Chemical Society 129, 15911–15918.

Liang, S., Chen, G., Zhao, Y., 2013. Conformationally switchable TTFV–phenylacetylene polymers: synthesis, properties, and supramolecular interactions with single-walled carbon nanotubes. Journal of Materials Chemistry C 1, 5477–5490.

Majumdar, P., Crowley, E., Htet, M., Stafslien, S.J., Daniels, J., VanderWal, L., Chisholm, B.J., 2011. Combinatorial Materials Research Applied to the Development of New Surface Coatings XV: An Investigation of Polysiloxane Anti-Fouling/Fouling-Release Coatings Containing Tethered Quaternary Ammonium Salt Groups.ACS Combinatorial Science 13, 298–309.

Melchers, R.E., 2003. Modelling of marine immersion corrosion for copper-bearing steels. Corrosion Science 45, 2307–2323.

Melchers, R.E., Jeffrey, R., 2008. Modeling of Long-Term Corrosion Loss and Pitting for Chromium-Bearing and Stainless Steels in Seawater. Corrosion Science 45, 2307–2323.

Mikhailov, A.A., Strekalov, P.V., Panchenko, Y.M., 2008. Atmospheric corrosion of metals in regions of cold and extremely cold climate (a review). Protection of Metals 44, 644–659.

Nakazawa, M., Somorjai, G.A., 1995. Coadsorption of water and selected aromatic molecules to model the adhesion of epoxy resins on hydrated surfaces of zinc oxide and iron oxide.Applied surface science 84, 309–323.

Paik, J.K., Thayamballi, A.K., Park, Y.I., Hwang, J.S., 2004. A time-dependent corrosion wastage model for seawater ballast tank structures of ships. Corrosion Science 46, 471–486.

Pourghaz, Y., Dongare, P., Thompson, D.W., Zhao, Y., 2011. Click functionalized poly(p-phenylene ethynylene)s as highly selective and sensitive fluorescence turn-on chemosensors for Zn2+ and Cd2+ ions. Chemical Communications 47, 11014.

Qin, S., Cui, W., 2003. Effect of corrosion models on the time-dependent reliability of steel plated elements. Marine Structures 16, 15–34.

Quantification of the oxidizing capacity of nanoparticulate zero-valent iron, 2005. Quantification of the oxidizing capacity of nanoparticulate zero-valent iron. Environmental science & technology 39, 1263–1268.

Rouw, A.C., 1997. Model epoxy powder coatings and their adhesion to steel.Progress in Organic Coatings 34, 181–192.

Sangaj, N.S., Malshe, V.C., 2004. Permeability of polymers in protective organic coatings.Progress in Organic Coatings 50, 28–39.

Sathyanarayana, M.N., Yaseen, M., 1995. Role of promoters in improving adhesions of organic coatings to a substrate. Progress in Organic Coatings 26, 275–313.

Selvaraj, M., Maruthan, K., Venkatachari, G., 2006. Studies on enhancement of surface durability for steel surface by camphor oil modified epoxy polyamide coating. Corrosion Science 48, 4365–4377.

Shifler, D.A., 2005. Understanding material interactions in marine environments to promote extended structural life. Corrosion Science 47, 2335–2352.

Skale, S., Doleček, V., Slemnik, M., 2008. Electrochemical impedance studies of corrosion protected surfaces covered by epoxy polyamide coating systems. Progress in Organic Coatings 62, 387–392.

Soares, C.G., Garbatov, Y., 1999. Reliability of maintained, corrosion protected plates subjected to non-linear corrosion and compressive loads. Marine Structures 12, 425–445.

Suay, J.J., Rodríguez, M.T., Razzaq, K.A., Carpio, J.J., 2003. The evaluation of anticorrosive automotive epoxy coatings by means of electrochemical impedance spectroscopy. Progress in Organic Coatings 46, 121–129.

Sørensen, P.A., Kiil, S., Dam-Johansen, K., Weinell, C.E., 2009. Anticorrosive coatings: a review. Journal of Coatings Technology and Research 6, 135–176.

Thomas, S.W., Joly, G.D., Swager, T.M., 2007. Chemical Sensors Based on Amplifying Fluorescent Conjugated Polymers. Chemical Reviews 107, 1339–1386.

Torresi, R.M., Souza, S., Silva, J.E., Torresi, S.I., 2005. Galvanic coupling between metal substrate and polyaniline acrylic blends: corrosion protection mechanism. Electrochimica Acta 50, 2213–2218.

Yadav, A.P., Nishikata, A., Tsuru, T., 2004. Degradation mechanism of galvanized steel in wet–dry cyclic environment containing chloride ions. Corrosion Science 46, 361–376.

Yebra, D.M., Kiil, S., Dam-Johansen, K., 2004. Antifouling technology—past, present and future steps towards efficient and environmentally friendly antifouling coatings.

Zamani, N.G., 1988. Boundary element simulation of the cathodic protection system in a prototype ship. Applied Mathematics and Computation 26, 119–134.

Zhang, J.T., Hu, J.M., Zhang, J.Q., Cao, C.N., 2004. Studies of water transport behavior and impedance models of epoxy-coated metals in NaCl solution by EIS. Progress in Organic Coatings 51, 145–151.

Zhang, X.G., 1996. Galvanic Corrosion of Zinc and Its Alloys. Journal of The Electrochemical Society 143, 1472–1484.

Appendix

Computer modeling procedure

The computer modeling has been carried out by using the BEASY simulation software to evaluate the performance of the newly designed polysiloxane-epoxy coatings. There are three major stages in BEASY software.

1. Pre-processing (Model preparation)

The geometry and environmental conditions can be defined in this stage. The geometry is described by subdividing the boundary of the problems (the surface of the structure and anodes in the case of CP) into a number of elements inter-connected at nodes. Then the zone properties are defined and which groups consolidate the different zones in the model is specified. Finally, the discretized mesh is generated for the model and a BEASY data file can be exported. In this 3D model, all the normal directions of the surfaces point outwards from the point of view of the electrolyte. The geometry model can be set up using the GID drawing program.

2. Numerical simulation

The computational scheme is based on the boundary element equations and their coupling them with the equations derived from the polarization data. By using the four

types of material properties, (Zinc-Steel, epoxy coating (ER), eugenol-modified polysiloxane (P1) and eugenol-ethoxylvinylsilane-modified polysiloxane (P2)), and specifying groups of surfaces with anodic and cathodic behavior, the set of equations were then solved iteratively and the values of potential and current density were computed at the boundary nodes.

3. Post-processing

In this stage, the numerical results can be viewed graphically by use of the post-processors at the 3D user interface of the BEASY software.

NMR Spectra

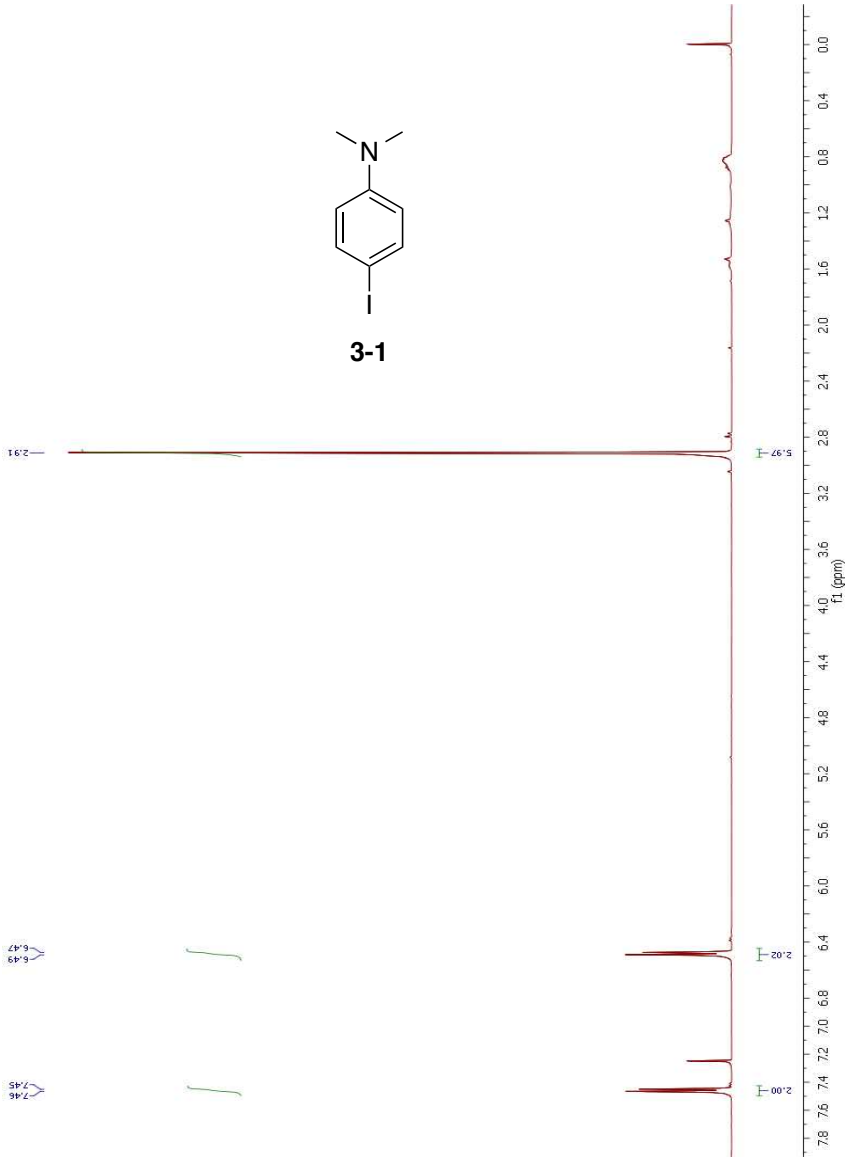

Figure A- 1: ^{1}H NMR (500 MHz, CDCl3) spectrum of compound 3-1.

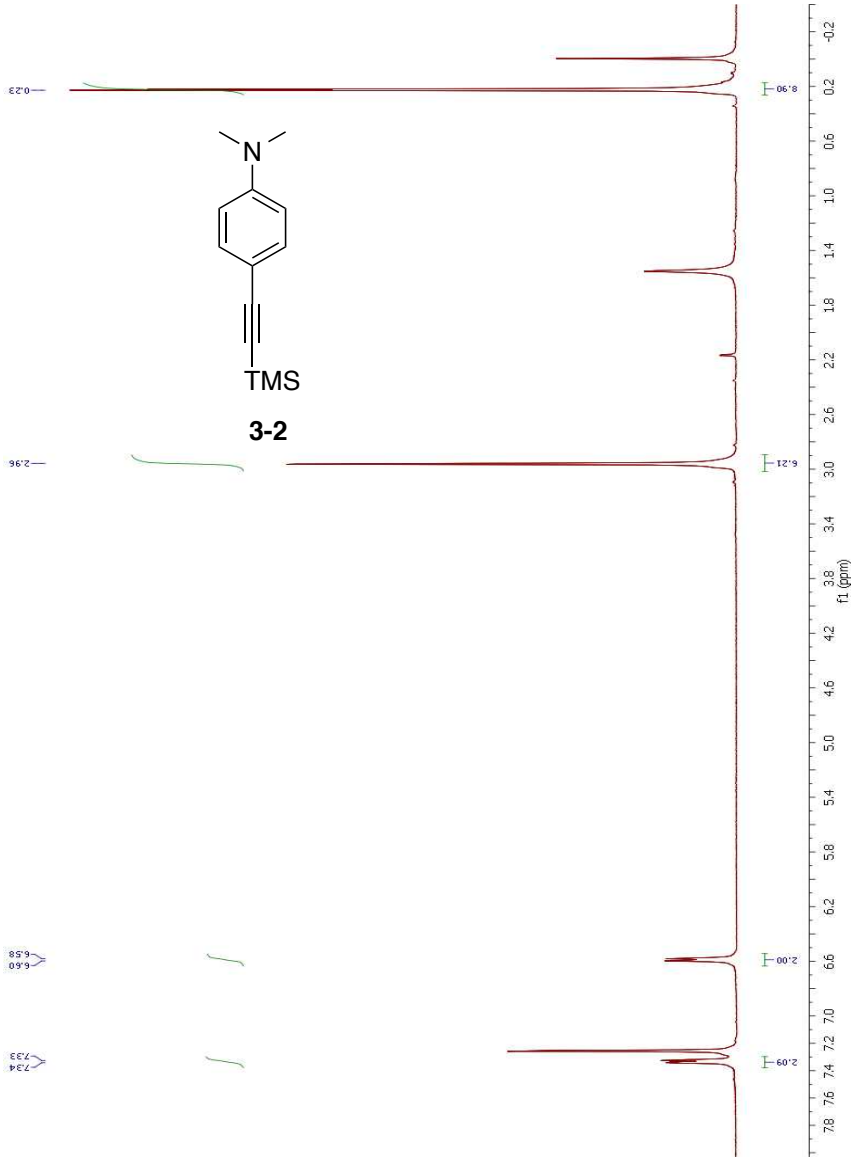

Figure A- 2: ^{1}H NMR (500 MHz, CDCl3) spectrum of compound 3-2.

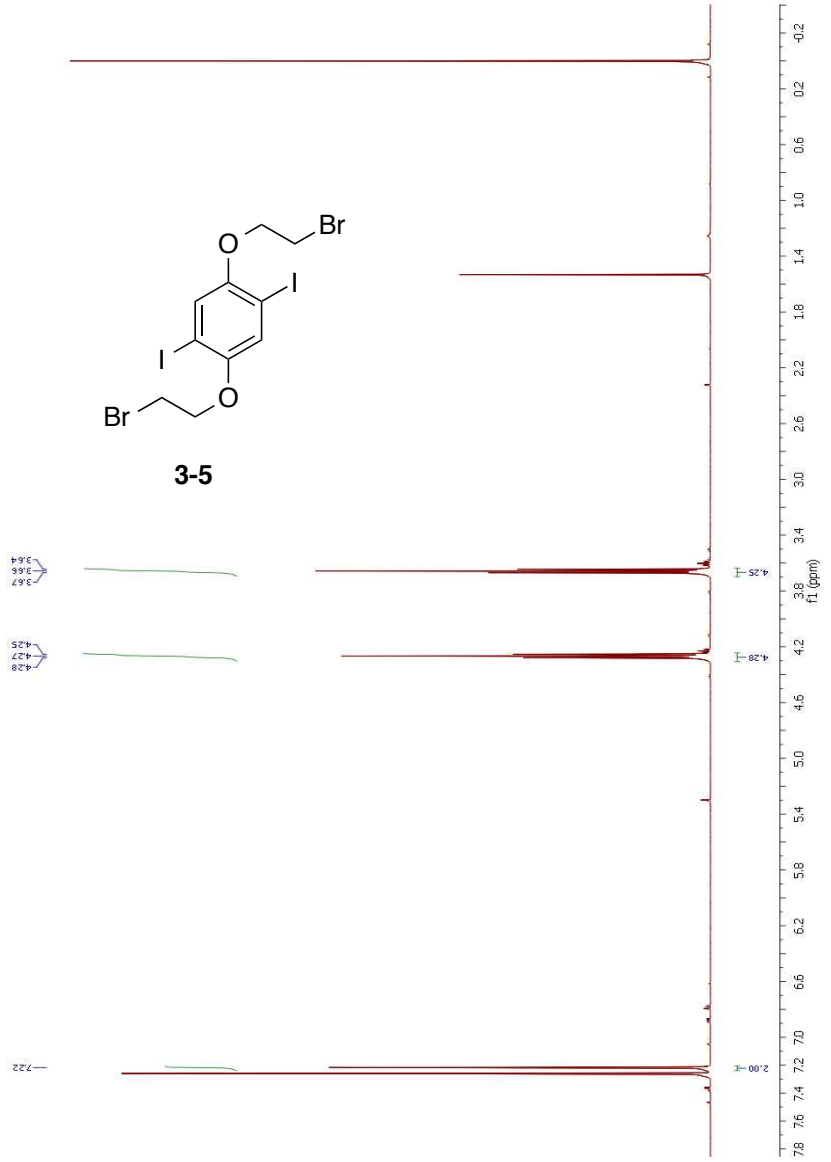

Figure A- 3: ^{1}H NMR (500 MHz, CDCl3) spectrum of compound 3-5.

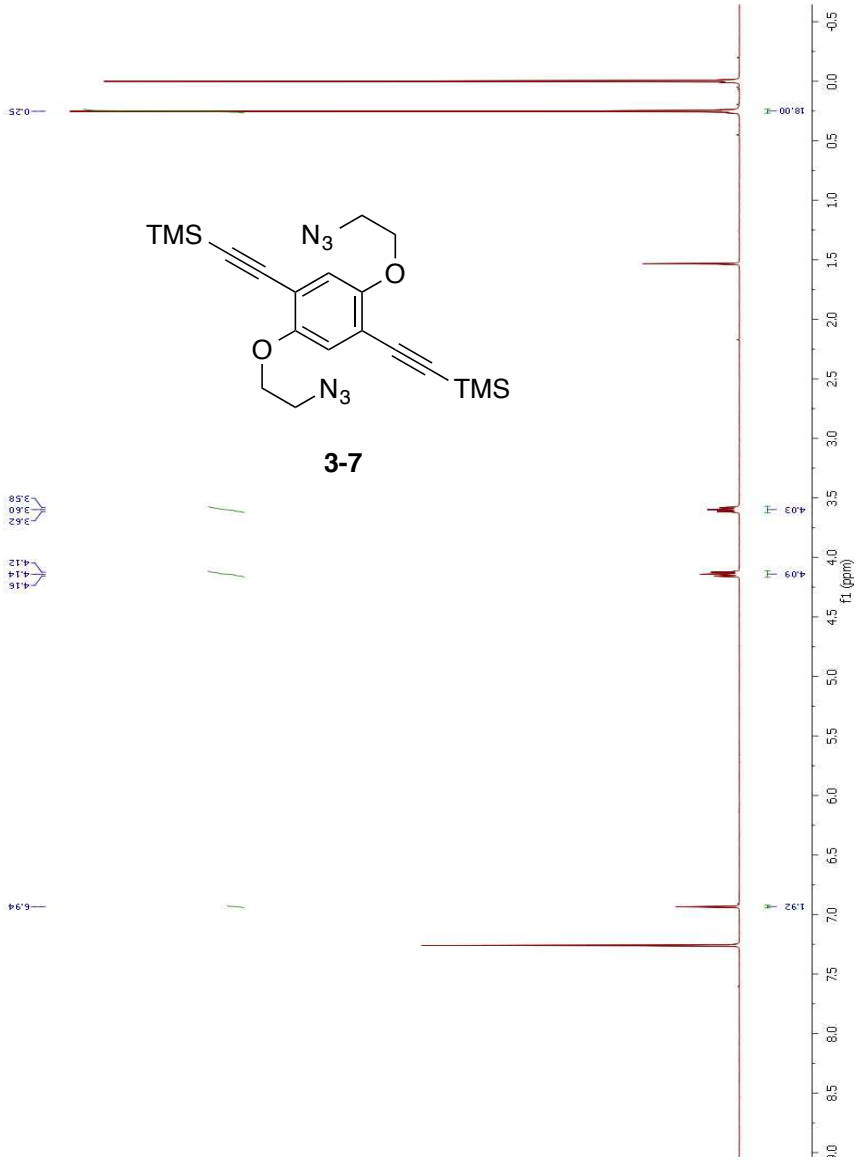

Figure A- 4: ^{1}H NMR (500 MHz, CDCl3) spectrum of compound 3-7.

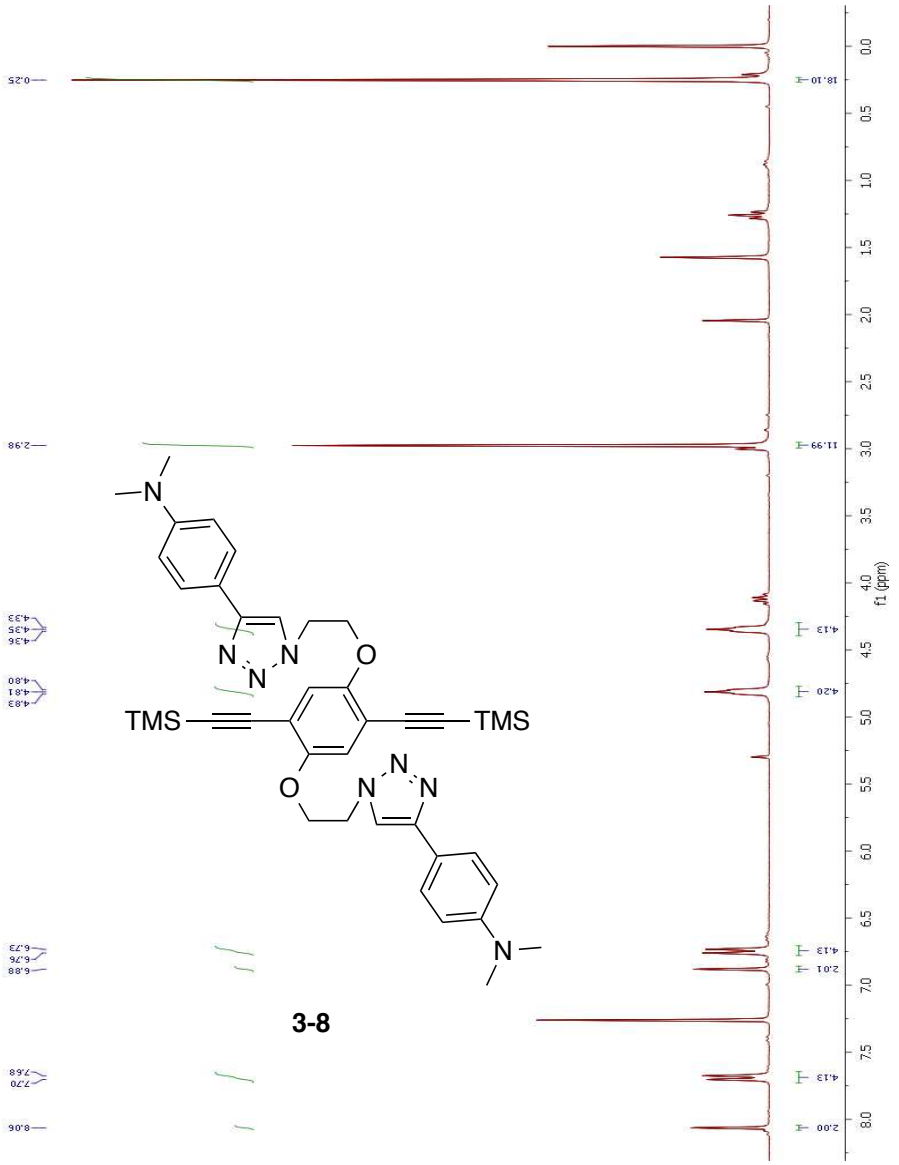

Figure A- 5: ^{1}H NMR (500 MHz, CDCl3) spectrum of compound 3-8.

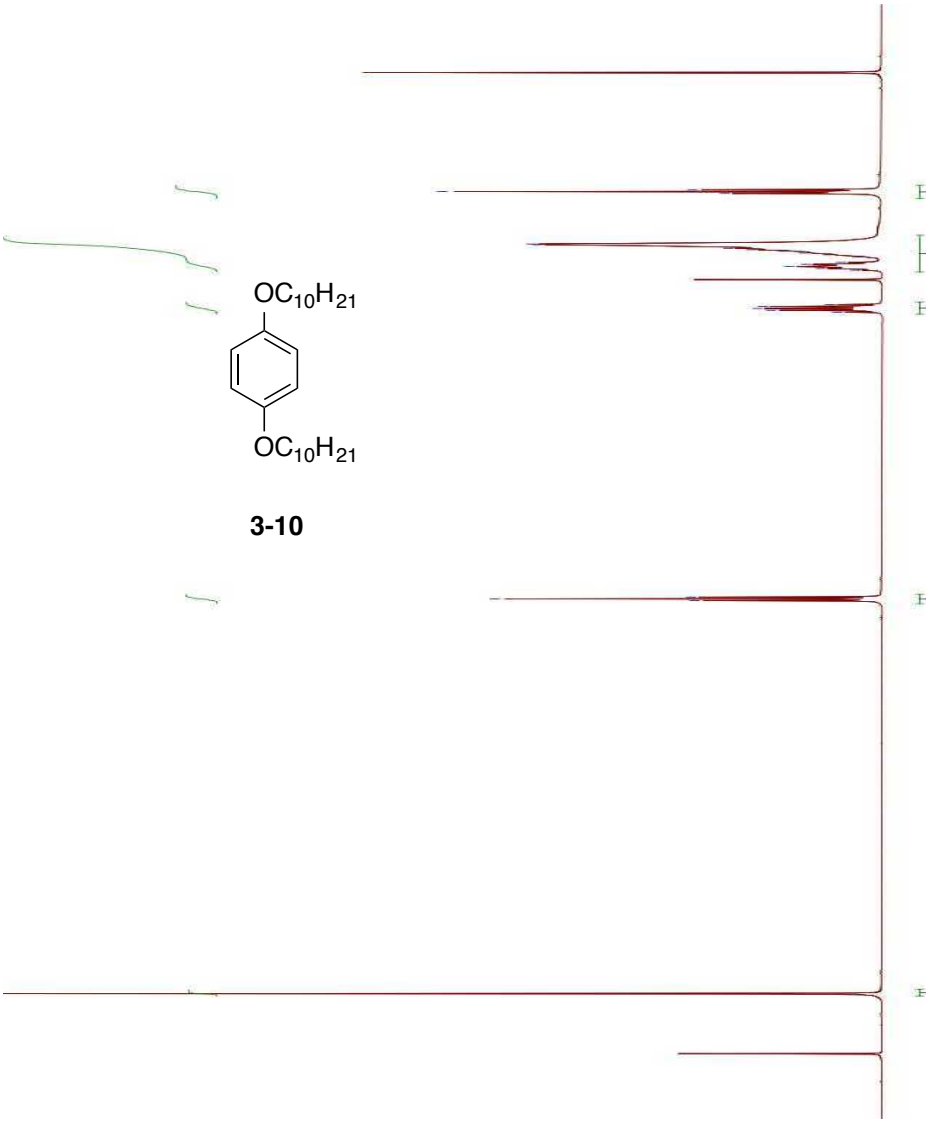

Figure A- 6: ^{1}H NMR (500 MHz, CDCl3) spectrum of compound 3-10.

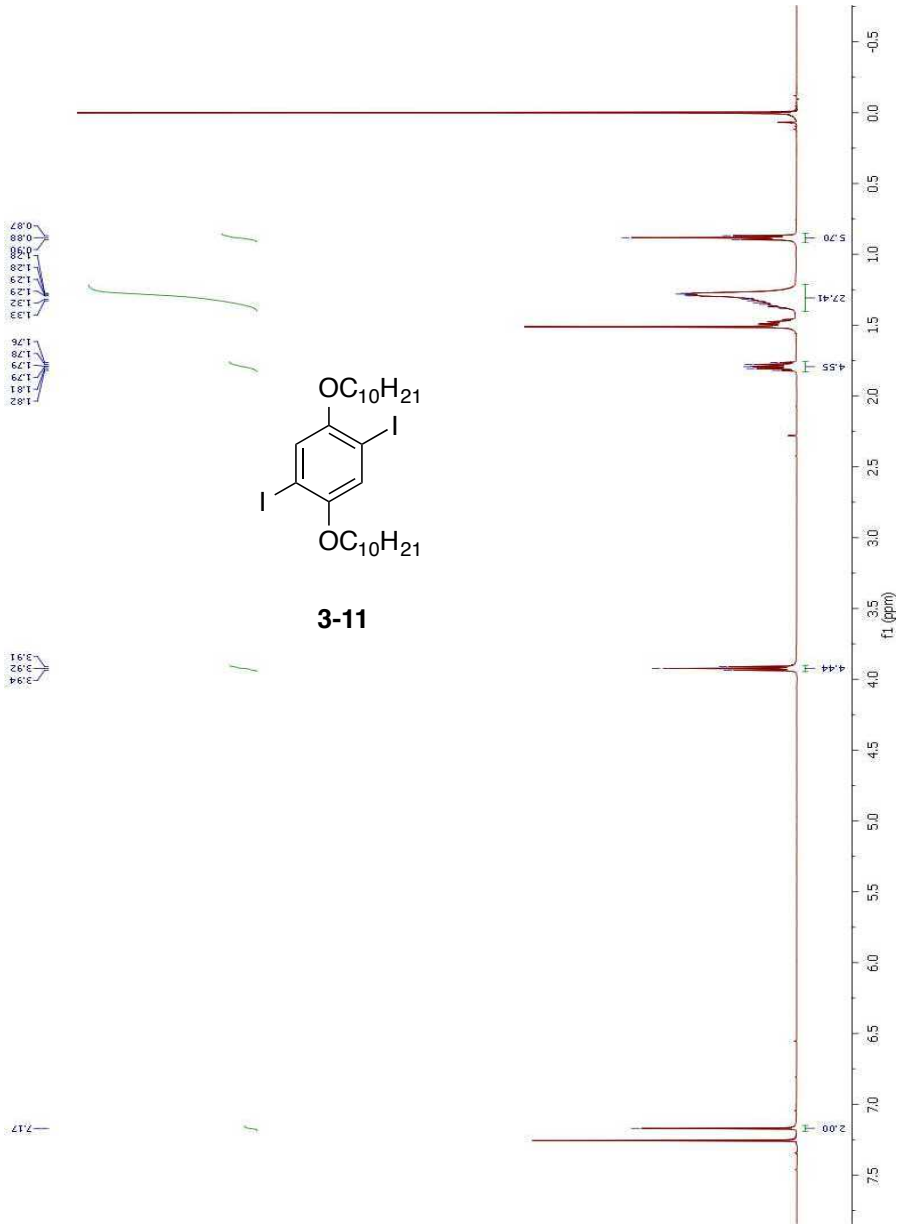

Figure A- 7: ^{1}H NMR (500 MHz, CDCl3) spectrum of compound 3-11.

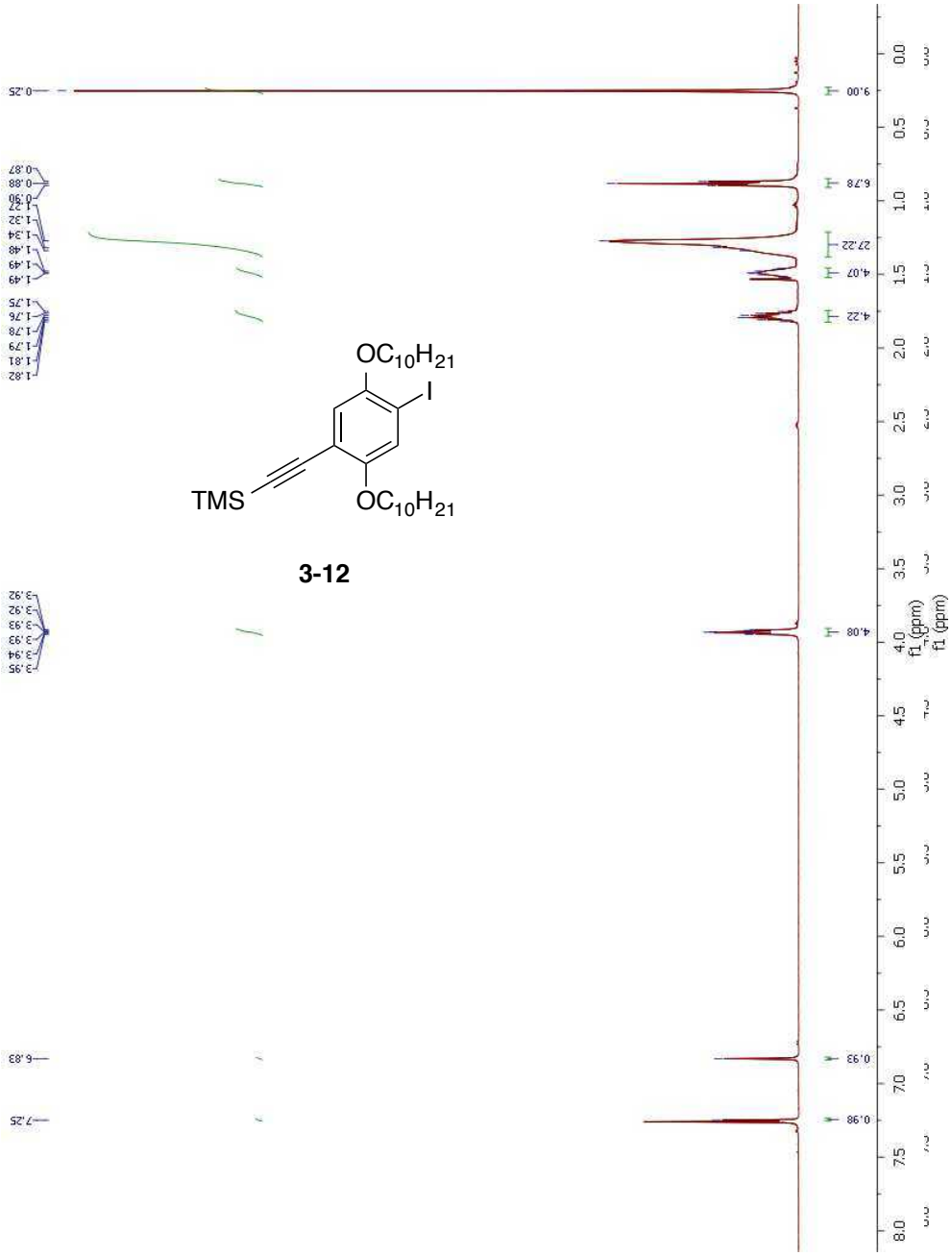

Figure A- 8: ^{1}H NMR (500 MHz, CDCl3) spectrum of compound 3-12.

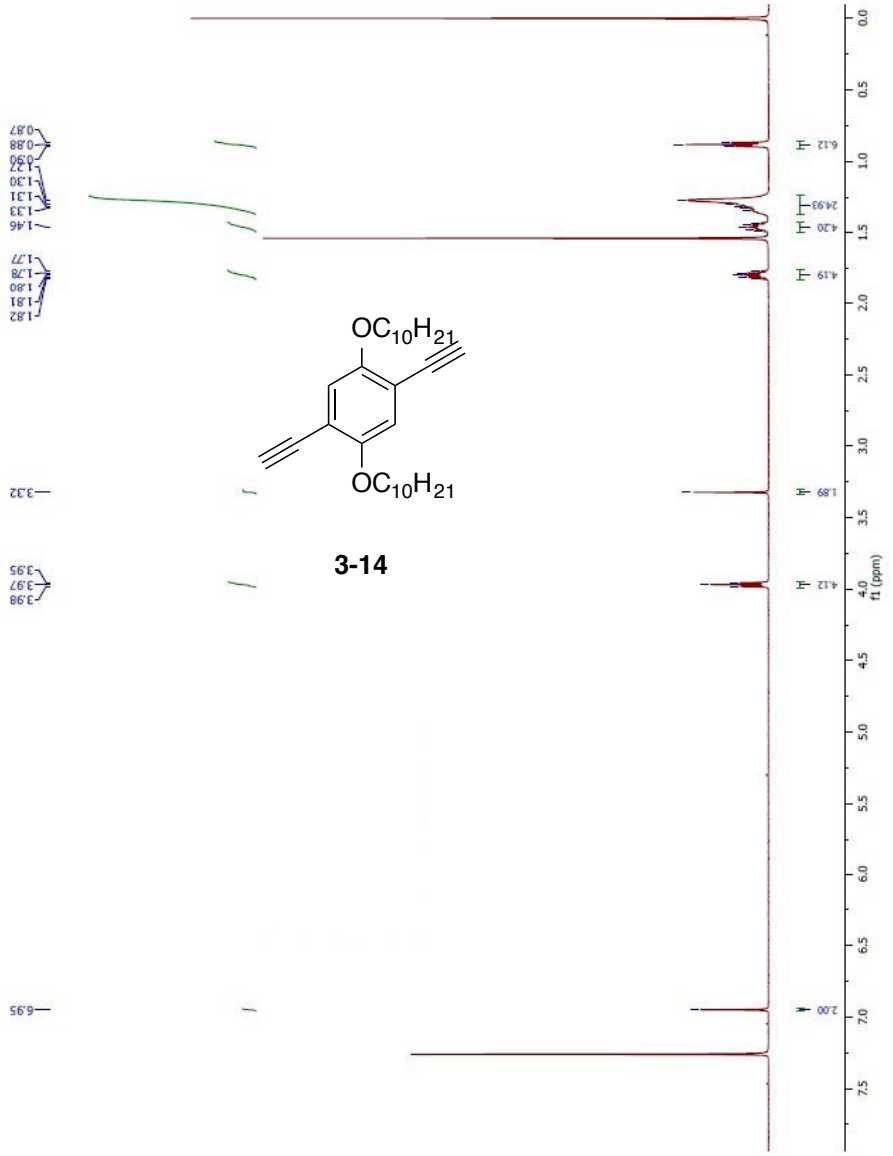

Figure A- 9: ^{1}H NMR (500 MHz, CDCl3) spectrum of compound 3-14.

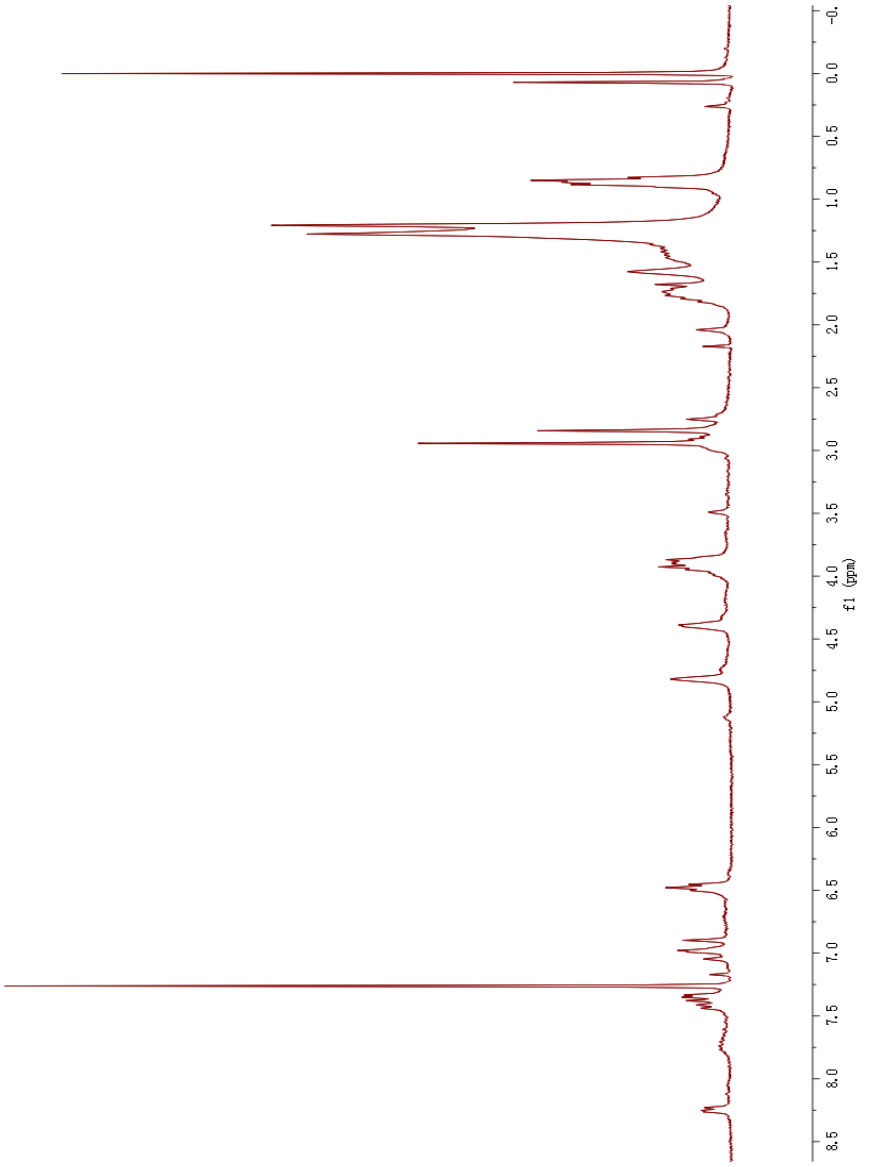

Figure A- 10: ^{1}H NMR (500 MHz, $CDCl_3$) spectrum of polymer P55.

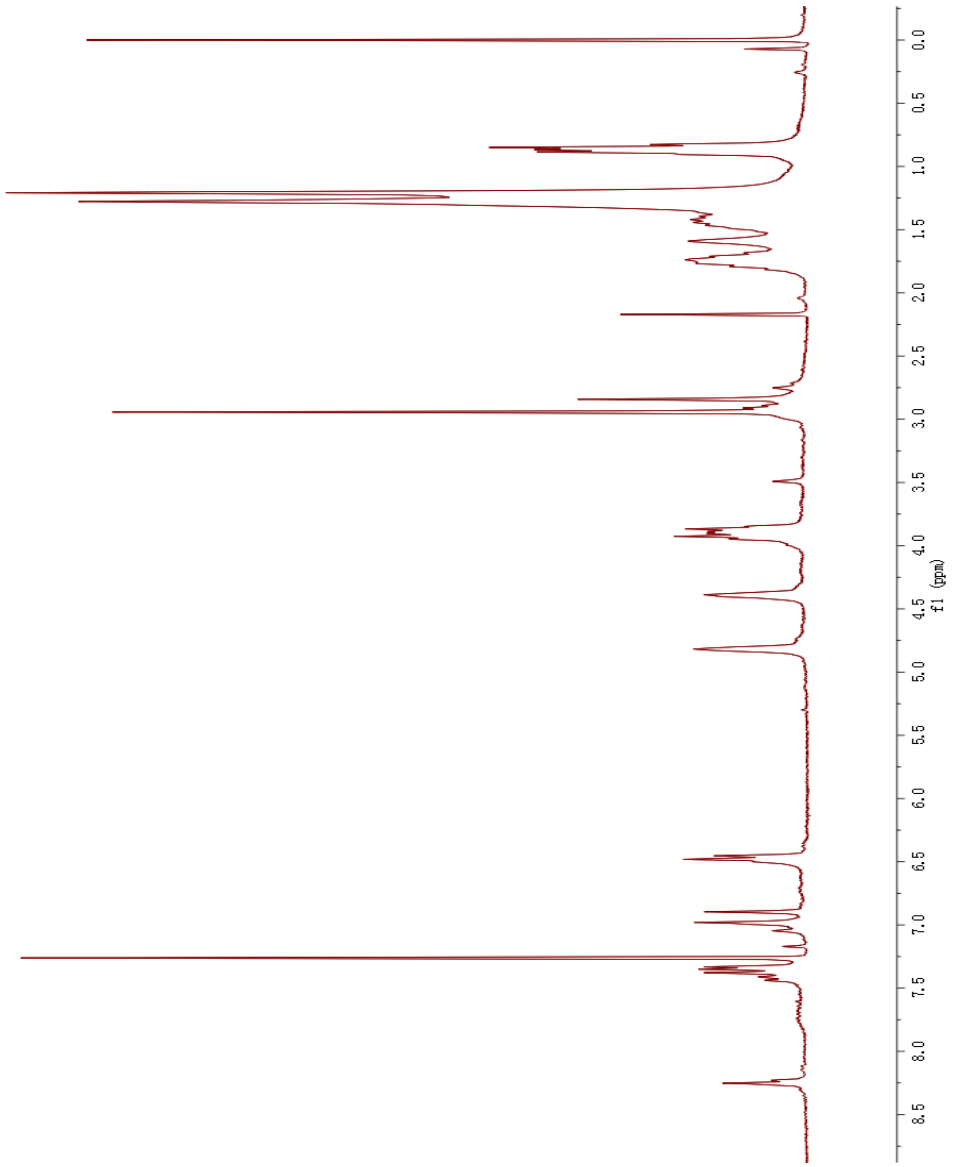

Figure A- 11: ^{1}H NMR (500 MHz, $CDCl_3$) spectrum of polymer P64.

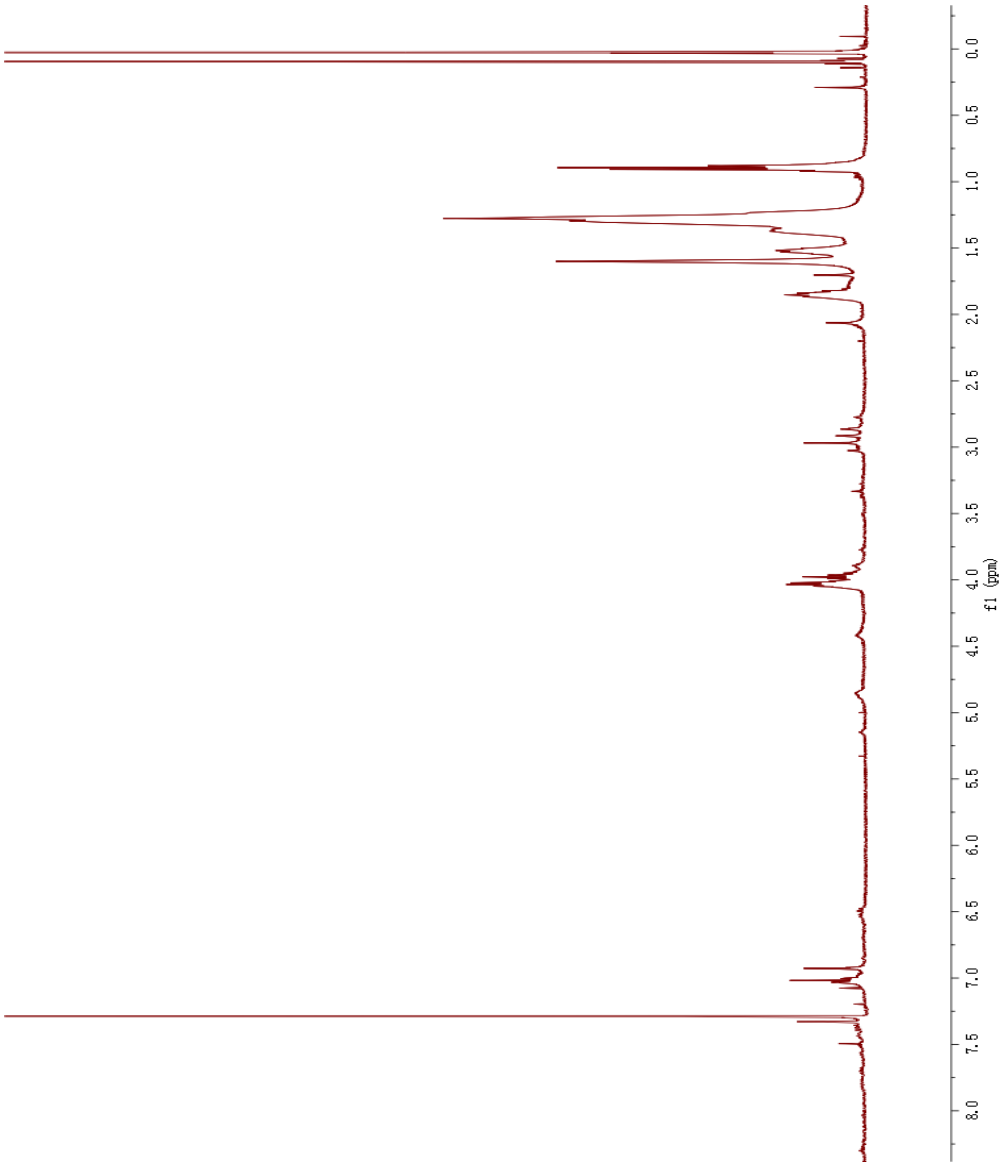

Figure A- 12: ^{1}H NMR (500 MHz, $CDCl_3$) spectrum of polymer P73.